DOT/FAA/TC-13/36,V1

Federal Aviation Administration
William J. Hughes Technical Center
Aviation Research Division
Atlantic City International Airport
New Jersey 08405

Analytical Tools for Residual Stress Enhancement of Rotorcraft Damage Tolerance

Volume 1: Stress and Crack Growth Analyses

August 2014

Final Report

This document is available to the U.S. public through the National Technical Information Services (NTIS), Springfield, Virginia 22161.

This document is also available from the Federal Aviation Administration William J. Hughes Technical Center at actlibrary.tc.faa.gov.

U.S. Department of Transportation
Federal Aviation Administration

NOTICE

This document is disseminated under the sponsorship of the U.S. Department of Transportation in the interest of information exchange. The U.S. Government assumes no liability for the contents or use thereof. The U.S. Government does not endorse products or manufacturers. Trade or manufacturers' names appear herein solely because they are considered essential to the objective of this report. The findings and conclusions in this report are those of the author(s) and do not necessarily represent the views of the funding agency. This document does not constitute FAA policy. Consult the FAA sponsoring organization listed on the Technical Documentation page as to its use.

This report is available at the Federal Aviation Administration William J. Hughes Technical Center's Full-Text Technical Reports page: actlibrary.tc.faa.gov in Adobe Acrobat portable document format (PDF).

Technical Report Documentation Page

1. Report No.	2. Government Accession No.	3. Recipient's Catalog No.
DOT/FAA/TC-13/36,V1		

4. Title And Subtitle	5. Report Date
ANALYTICAL TOOLS FOR RESIDUAL STRESS ENHANCEMENT OF ROTORCRAFT DAMAGE TOLERANCE, VOLUME 1: STRESS AND CRACK GROWTH ANALYSES	August 2014
	6. Performing Organization Code
7. Author(s)	8. Performing Organization Report No.
James C. Newman, Jr., Steve R. Daniewicz, and Shakhrukh Ismonov	
9. Performing Organization Name and Address	10. Work Unit No. (TRAIS)
Department of Aerospace Engineering 501 Hardy Road Mississippi State University Mississippi, MS 39762	11. Contract or Grant No. DTFACT-06-C-00025
12. Sponsoring Agency Name and Address	13. Type of Report and Period Covered
U.S. Department of Transportation Federal Aviation Administration Software and Systems Branch FAA William J. Hughes Technical Center Atlantic City International Airport Atlantic City, NJ 08405	Final Report
	14. Sponsoring Agency Code ANG-E27

15. Supplementary Notes

The Federal Aviation Administration William J. Hughes Technical Center Aviation Research Division Technical Monitors were Traci Stadtmueller and Dr. John G. Bakuckas, Jr.

16. Abstract

Finite element and numerical studies were performed to develop the stress distributions on tests conducted to study crack growth in residual stress-bearing structural details and materials typical of rotorcraft structures. Companion analyses were also developed to assess the accuracy of typical fatigue crack growth models using either linear superposition or a nonlinear method. In another part of the Federal Aviation Administration-sponsored project, fatigue crack growth tests were carried out on a range of specimens that progressed from very simple to fairly complex. These tests involved laser shock-peened, compact (C(T)) specimens; cold-worked open hole specimens; pin-loaded cold-worked hole specimens, and a typical rotorcraft component with cold-worked fastener loaded holes.

Crack growth analyses were performed on the laser peened C(T) specimens and the cold-worked open hole specimens using linear superposition, whereas a nonlinear method was also applied to the cold-worked hole specimens. Using the measured residual stresses, the linear superposition method greatly overestimated crack growth lives in the C(T) specimens, whereas using the residual stress intensity factors computed from either a weight function or Green's function method fell short of the test data. Three-dimensional elastic-plastic finite element analyses (FEAs) were performed on the cold-worked hole process to generate the residual stress distributions used in the linear superposition method. Crack growth lives predicted using the nonlinear method agreed well with the test data. In addition, a two-dimensional elastic-plastic FEA was performed on the pin-loaded and cold-worked hole configuration. Lastly, FEA were also conducted on the nested angle components under typical cold-worked hole conditions.

17. Key Words	18. Distribution Statement
Damage tolerance, Fatigue, Crack growth, Stress analysis, Residual stress, Stress intensity factor, Finite element method	This document is available to the U.S. public through the National Technical Information Service (NTIS), Springfield, Virginia 22161. This document is also available from the Federal Aviation Administration William J. Hughes Technical Center at actlibrary.tc.faa.gov.

19. Security Classif. (of this report)	20. Security Classif. (of this page)	21. No. of Pages	22. Price
Unclassified	Unclassified	135	

Form DOT F 1700.7(8-72) Reproduction of completed page authorized

TABLE OF CONTENTS

			Page
EXECUTIVE SUMMARY			xiii
1.	INTRODUCTION		1
	1.1	Purpose	1
	1.2	Background	2
	1.3	Research Objectives	3
2.	LITERATURE SURVEY ON RESIDUAL STRESS ENHANCEMENTS		3
	2.1	Shot Peening	4
	2.2	The LSP	6
	2.3	Cold Working of Holes	9
	2.4	Cold-Expanded Bushing	14
	2.5	Summary	17
3.	MATERIALS		17
	3.1	Tensile Properties	17
	3.2	Fatigue Crack Growth Properties	18
4.	CRACK GROWTH ANALYSIS METHODS WITH RESIDUAL STRESSES		20
	4.1	Linear Superposition	21
		4.1.1 As-Machined Compact Specimens	22
		4.1.2 Laser Shock-Peened C(T) Specimens	23
		4.1.3 Cold-Worked Open Hole Specimens	27
	4.2	Nonlinear Method	31
		4.2.1 The MSU Tests	36
		4.2.2 The HE Tests	40
5.	THE 3D ANALYSES OF THE COLD WORKING PROCESS		45
	5.1	Introduction	45
	5.2	The FEA of the Cold Working Process	46
		5.2.1 Configuration	46
		5.2.2 Material Models	48
		5.2.3 The FE Model	49
		5.2.4 Boundary Conditions and Cold Working Simulation	51
		5.2.5 Validation	53

5.3 Results 53

5.3.1 Thin Specimen 53
5.3.2 Thick Specimen 59

5.4 Conclusions 63

6. STRESS AND CRACK ANALYSES FOR PIN-LOADED HOLES 64

6.1 Elastic-Plastic Stress Analysis of Cold-Worked Pin-Loaded Holes 64

6.1.1 Introduction 64
6.1.2 Configuraton and Material Models 66
6.1.3 The FE Model and BCs 67
6.1.4 Model Validaton 69
6.1.5 Results 73

6.2 The SIFs for a Single Crack at Pin-Loaded Hole 77

6.2.1 The FE Model and BCs 77
6.2.2 Methodology 78
6.2.3 Results 81

7. STRESS AND CRACK ANALYSES ON COLD-WORKED ROTORCRAFT COMPONENT 83

7.1 Configuration 83
7.2 Material Model 85
7.3 The FE Model and BCs 86
7.4 Results 89

8. CONCLUSION 93

9. REFERENCES 93

APPENDICES

A—Green's Function for Compact Specimen
B—Linear Superposition Life Prediction Code

LIST OF FIGURES

Figure		Page
1	Shot Peening Process	4
2	Influence of Shot Peening Parameters on Distribution of Residual Stresses	4
3	The FE Models for the Target Work Piece and the Shot: 3D and 2D Axisymmetric Mesh	5
4	The LSP Process	6
5	One-Sided LSP Model	8
6	Single LSP Impact: The 3D FE Model and Residual Stress Distributions With Respect to Different Impact Pressures	9
7	Fatigue Technology, Inc. Split Sleeve Cold Expansion Process and Residual Stress Distribution	10
8	Dependence of Radial and Tangential Stress in a Wide Aluminum Plate on the Level of Interference With a Steel Pin	11
9	Details of the 3D FE Model Used for the Cold Working Process Simulation Model Assembly; Plate and Sleeve Assembly; Plate and Sleeve Mesh, Detail; Hole Mesh, Detail; Detail Near the Mandrel; Sleeve and Plate Near the Hole	12
10	von Mises Residual Stress Field After the Hole Deformation Process: Uniform Hole Expansion and Cold Working Process Using a Rigid Mandrel	13
11	The FEA Results With Two Adjacent Holes	13
12	Cold-Expanded Bushing Process	14
13	The 3D FE Model Mesh: BCs and Cold-Expanded Bushing	15
14	Experimental and FEM Residual Strain Results After Bushing Installation	16
15	Residual Stresses With Bushing Installed, After Bushing Was Removed and Caused by Shrink-Fit Bushing	16
16	Effective SIF Range Against-Rate for 7075-T6 Aluminum Alloy Sheet for Various Stress Ratios on Small-Width M(T) Specimens	19

17	Effective SIF Range Against-Rate for 7075-T6 Aluminum Alloy Sheet for Various Stress Ratios on Large-Width M(T) Specimens	19
18	Measured and Calculated Crack Length-Against-Cycles for As-Machined C(T) Specimen Using Linear Superposition Code	23
19	Measured Residual Stresses in Laser Shock-Peened C(T)Specimens	24
20	Measured and Calculated Residual SIFs for Laser Shock-Peened C(T)Specimens	25
21	Measured Residual SIFs for Laser Shock-Peened C(T)Specimens and Calculated Maximum and Minimum SIFs	26
22	Measured and Calculated Crack Length-Against-Cycles for Laser Shock-Peened C(T)Specimen Using Linear Superposition Code	27
23	Single Crack Emanating From an Open Hole Subjected to Remote Uniform Stress	28
24	Normalized Residual Stresses After Reaming and Notching Cold-Worked Hole From Two Different FEAs	29
25	Various SIFs for Notched Cold-Worked Hole as a Function of Crack Length-to-Hole Radius Ratio	30
26	Measured and Predicted Crack Length-Against-Cycles for Cold-Worked, Reamed, and Slotted Open Hole Specimen Using Linear Superposition Code	31
27	Cold-Worked Hole and Simulated Behavior in FASTRAN	33
28	Normalized Residual Stresses for Cold-Worked Hole From FEA and Simulated Behavior in FASTRAN	34
29	Normalized Residual Stresses After Reaming and Notching Cold-Worked Hole From FEA and Simulated Behavior in FASTRAN	35
30	Residual Plastic Deformations in FASTRAN During Simulated Cold Working and After Reaming	35
31	Measured and Predicted Crack Length-Against-Cycles Under Constant-Amplitude Loading for Several Single Crack-at-an-Open Hole Specimens Made of 7075-T6 Aluminum Alloy	37
32	Measured and Predicted Crack Length-Against-Cycles Under Constant-Amplitude Loading After Cold Working, Reaming, and Notching	38

33 Calculated Crack Opening Stress Levels as a Function of Crack Length During Constant-Amplitude Loading for a Residual Stress-Free Hole and a Simulated Cold-Worked Hole 39

34 Calculated Crack-Opening Stress Levels as a Function of Cycles During Constant-Amplitude Loading for a Residual Stress-Free Hole and a Simulated Cold-Worked Hole 39

35 Measured and Predicted Crack Length-Against-Cycles Under Constant-Amplitude Loading for Single Crack-at-an-Open Hole Specimens Made of 7075-T6 Aluminum Alloy at $R = 0.5$ 41

36 Measured and Predicted Crack Length-Against-Cycles Under Constant-Amplitude Loading for Single Crack-at-an-Open Hole Specimens Made of 7075-T6 Alluminum Alloy at $R = 0.1$ 42

37 Measured and Predicted Crack Growth Rates for the 7075-T6 Aluminum Alloy at $R = 0.1$, and for the 7075-T6 Aluminum Alloy at $R = 0.5$ 43

38 Measured and Calculated Crack Length-Against-Cycles Under Constant-Amplitude Loading After Cold Working, Reaming, and Notching for $R = 0.1$ 44

39 Measured and Calculated Crack Length-Against-Cycles Under Constant-Amplitude Loading After Cold Working, Reaming, and Notching for $R = 0.5$ 44

40 Split Sleeve CX Process Description 45

41 Geometries of the Specimen, Split Sleeve, and Mandrel 47

42 Elastic-Plastic Stress-Strain Curve of the 7075-T6 Aluminum Alloy Sheet 49

43 The FE Mesh of the CX Model 50

44 Configuration of the Smoothed Split Sleeve Edge 51

45 Prescribed BCs Used in the FE Model 52

46 Normalized Circumferential Residual Stress Results From Isotropic and Kinematic Hardening Material Models Compared With Experimental Measurements for Thin Specimen Entrance Face, $z/t_p = 0.25$, Mid-Thickness, $z/t_p = 0.75$, Exit Face, and Through-Thickness Direction at $x/r = 1$ and $y = 0$ 54

47 Normalized Circumferential Residual Stress Results for Different Friction Coefficients for Thin Specimen Entrance Face, Mid-Thickness, Exit Face, and Through-Thickness Direction at $x/r = 1$ and $y = 0$ 55

48 Circumferential Residual Stress Curves From Split Sleeve and Non-Split Sleeve Models for Thin Specimen on the Plane $y = 0$, at the Hole Surface; with $\mu = 0.2$, and Case (a) BC 57

49 Circumferential Residual Stress Contours Around the Hole Edge of the Sheet for the Split Sleeve and Non-Split Sleeve Models of the Thin Specimen, $\mu = 0.2$, Case (a) BC 58

50 Normalized Circumferential Residual Stress Results for Cases (a) and (b) BCs With $\mu = 0.2$ for Thin Specimen Entrance Face, Mid-Thickness, Exit Face, and Through-Thickness Direction at $x/r = 1$ and $y = 0$ 59

51 Normalized Circumferential Residual Stress Results From Isotropic and Kinematic Hardening Material Models Compared With Experimental Measurements for Thick Specimen Entrance Face, $z/t_p = 0.25$, Mid-Thickness, $z/t_p = 0.75$, Exit Face, and Through-Thickness Direction at $x/r = 1$ and $y = 0$ 60

52 Normalized Circumferential Residual Stress Results for Different Friction Coefficients for Thick Specimen, Entrance Face, Mid-Thickness, Exit Face, Through-Thickness Direction at $x/r = 1$ and $y = 0$ 61

53 Circumferential Residual Stress Curves From Split Sleeve and Non-Split Sleeve Models for Thick Specimen on the Plane $y = 0$ and at the Hole Surface, with $\mu = 0.2$ and Case (a) BC 62

54 Normalized Circumferential Residual Stress Results for Cases (a) and (b) BCs With $\mu = 0.2$ for Thick Specimen Entrance Face, Mid-Thickness, Exit Face, and Through-Thickness Direction at $x/r = 1$ and $y = 0$ 63

55 An Infinite Sheet Loaded by a Resultant Pin Load P 65

56 Pin-Loaded Hole Model Configuration 67

57 Prescribed BCs of the FE Model 67

58 The FE Mesh for the Pin-Loaded Hole Model 68

59 Convergence Studies for Radial and Hoop Stress Distributions at $r = r_o$, L is Element Size at the Hole Edge 70

60 Comparison of Normal, Shear, and Tangential Stress Distributions Along the Hole Circumference With Results 72

61 Comparison of the Normal and Tangential Stress Distributions Along The Hole Circumference With Results 73

62 Hoop Stress Distributions Along the Hole Circumference From Elastic and Elastic-Plastic Models 74

63 Radial Stress Distributions Along the Circumference of Cold-Expanded and Pin-Loaded Hole 75

64 Hoop Stress Distributions Along the Circumference of the Cold-Expanded and Pin-Loaded Holes 76

65 Hoop Stress Distributions Along the Line $y = 0$ Around the Cold-Expanded and Pin-Loaded Holes 76

66 Sheet Configuration: $h = 65.0$ mm, $2w = 44.45$ mm, $2r = 7.07$ mm, and $d = 22.23$ mm 77

67 Case (b) Loading for Cracked Pin-Loaded Hole 77

68 Sample FE Mesh for Cracked Pin-Loaded Hole With $(a+r)/w = 0.25$ 78

69 A Single Crack From a Hole in an Infinite Plate 79

70 Nodal Contact Stresses 80

71 Boundary Correction Factors for a Single Crack From an Open Hole in a Finite Sheet Loaded in Tension 82

72 Boundary Correction Factors for a Single Crack From a Pin-Loaded Hole in a Finite Sheet 83

73 Nested Angle Joint Loaded in Tension 84

74 Drawings and Dimensions of Small and Large Angles 85

75 Stress-Strain Curve for 7075-T6511 Aluminum Alloy 86

76 The 3D Model of Pin-Joint Component 87

77 The FE Mesh of the Nested Angle Model 88

78 Orientation of the Crack Around Critical Hole d1 89

79 Hoop Stress Distributions Around Holes 90

80 Circumferential Stress Distributions Around Hole d1 in Angle 2 at Front Face, Mid-Thickness, and Back Face 91

81 Load Distributions to Each Hole: No Crack, $(a+r)/r = 1.4$, $(a+r)/r = 1.8$ 92

LIST OF TABLES

Table		Page
1	Mechanical Properties for 7075-T6 and 7075-T6511 Aluminum Alloys	18
2	Effective SIF-Against-Rate Relationship for 7075-T6 Aluminum Alloy	20
3	Cold Working Model Dimensions in Millimeters	48

LIST OF SYMBOLS, ABBREVIATIONS, AND ACRONYMS

α	Constraint factor
Δa	Crack growth increment, mm
ΔK	Stress intensity factor range, MPa√m
ΔK_o	Effective stress intensity factor range threshold, MPa√m
ΔK_{th}	Stress intensity factor range threshold, MPa√m
ΔK_{eff}	Effective stress intensity factor range, MPa√m
$(\Delta K_{eff})_T$	Effective stress intensity factor range at flat-to-slant crack growth, MPa√m
σ_{ij}	Normal stresses, MPa
σ_o	Flow stress (average of σ_{ys} and σ_u), MPa
σ_{ys}	Yield stress (0.2 % offset), MPa
σ_u	Ultimate tensile strength, MPa
ν	Poisson's ratio
μ	Friction coefficient
θ	Angle measured around a hole
θ_{max}	Angle corresponding to the peak hoop stress
B	Specimen thickness, mm
C_i	Crack growth equation coefficients (i = 1 to 5)
a	Crack length, mm
a_i	Initial crack length, mm
a_n	Notch length, mm
a/W	Crack-length-to-width ratio
da/dN	Fatigue crack growth rate in a-direction, m/cycle
d_{max}	Distance from center of hole to end of maximum plastic-zone size, mm
F	Boundary correction on stress intensity factor
E	Modulus of elasticity, MPa
J	Contour integral, MPa-m
K_I	Mode I stress intensity factor, MPa√m
K_{Ie}	Elastic stress intensity factor at failure, MPa√m
K_{max}	Maximum applied stress intensity factor, MPa√m
K'_{max}	Total maximum stress intensity factor ($K_{max} + K_{rs}$), MPa√m
K_{min}	Minimum applied stress intensity factor, MPa√m
K'_{min}	Total minimum stress intensity factor ($K_{min} + K_{rs}$), MPa√m
K_{op}	Crack opening stress intensity factor, MPa√m
K_{rs}	Residual stress intensity factor, MPa√m
N	Number of cycles
P	Applied load, kN
P_{max}	Maximum applied load, kN
P_{min}	Minimum applied load, kN
P_o	Crack opening load, kN
r	Hole radius, mm
R	Stress ratio (K_{min}/K_{max} or P_{min}/P_{max})
S_o	Crack opening stress, MPa
W	Total width ($2w$) of M(T) specimen, mm

w	Width of C(T) specimen and one half width of M(T) specimen, mm
x	Distance from center of hole along crack path, mm
1D	One-dimensional
2D	Two-dimensional
3D	Three-dimensional
ASTM	American Society for Testing and Materials
BC	Boundary condition
C(T)	Compact specimen
CX	Cold expansion
EDM	Electrical discharge machining
FAA	Federal Aviation Administration
FE	Finite element
FEA	Finite element analysis
FEM	Finite element method
GF	The Green's Function
HE	Hill Engineering, LLC
LSP	Laser shock peening
MSU	Mississippi State University
M(T)	Middle-crack-tension specimen
SAC	Sikorsky Aircraft Corporation
SIF	Stress intensity factor

EXECUTIVE SUMMARY

Finite element and numerical studies were performed to develop the stress states on tests conducted to study crack growth in residual stress-bearing structural details and materials typical of rotorcraft structures. Companion analyses were also developed to assess the accuracy of typical fatigue crack growth models using either linear superposition or a nonlinear method. In another part of the Federal Aviation Administration-(FAA-) sponsored project, fatigue crack growth tests were carried out on a range of specimens that progressed from very simple to fairly complex. The specimen geometries were one-dimensional (1D) cracks in standard compact (C(T)) specimens, 1D and two-dimensional (2D) cracks in specimens with open holes, 1D cracks in specimens with pin-loaded holes, and 2D cracks at fastener holes in nested angle specimens with a lap shear joint. Most series of tests were performed under constant-amplitude cyclic loading, but additional tests of pin-loaded hole and nested angle specimens were performed under variable-amplitude loading. Each test series employed a number of identical specimens (replicate tests) as well as specimens in at least two material conditions: an as-machined condition (without residual stress) and a residual stress-bearing condition. Tests on the C(T) specimens had residual stress induced by laser shock peening, whereas all other tests had residual stress induced by cold-hole expansion. Replicate tests provided measures of variability in residual stress and fatigue crack growth. Companion linear elastic fracture mechanics analyses were performed to develop Green's function (GF) for the C(T) specimen and to develop a linear superposition life prediction code.

Crack growth analyses were performed on the laser shock-peened C(T) specimens and the cold-worked open hole specimens using linear superposition, while a nonlinear method was also applied to the cold-worked hole specimens. Using the measured residual stresses, the linear superposition method greatly overestimated crack growth lives in the C(T) specimens, whereas using the residual stress intensity factors computed from either a weight function or GF method fell short of the test data. Three-dimensional elastic-plastic finite element analyses (FEA) were performed on the cold-worked hole process to generate the residual stress distributions used in the linear superposition method. Crack growth lives predicted using the nonlinear method agreed fairly well with the test data. In addition, a 2D elastic-plastic FEA was performed on the pin-loaded and cold-worked hole configuration. Finally, FEAs were also conducted on the nested angle components under typical cold-worked hole conditions.

The FAA William J. Hughes Technical Center's Rotorcraft Damage Tolerance Program sponsored this project. This work is part of a larger project described in two additional volumes and was performed at Mississippi State University with subcontracts to Hill Engineering, LLC (Ranch Cordova, CA) and to the Sikorsky Aircraft Company.

1. INTRODUCTION.

Fatigue is the source of at least half of all mechanical failures [1]. The fatigue problem is complex and not fully understood, but it is very important in the design of mechanical systems. Fatigue is of special interest to the rotorcraft industry. Many components used in rotorcraft are fastened together; thus, fastener holes are prevalent. Fastener holes are a source of high stress concentration and, therefore, are potential sites for fatigue cracks.

One technique used to enhance the fatigue strength of a fastener hole is to introduce a compressive residual stress field around the hole. An applied load must overcome this residual stress before the crack can grow, thus leading to a longer fatigue life. Although it is widely recognized that compressive residual stress improves fatigue life, in many applications the benefits of compressive residual stresses are not included in the final predicted fatigue life [2]. In these cases, the residual stress provides added confidence against usage uncertainty, but because it is not quantified, it leads to conservative life predictions. The benefits of residual stress treatments are not adequately included in design analyses, which results in overly conservative designs. This prevents optimal planning of appropriate damage inspection intervals, which is a critical component of the damage tolerance design philosophy. The goal of this research was to support the creation of tools to accurately account for the benefits of residual stresses in design analyses. This allowed residual stress locations and amounts to be optimized, thus increasing component lifetimes, decreasing component weights, and creating more useful intervals for damage inspection.

1.1 PURPOSE.

This project's objective was to advance the previous research to provide practical, reliable, and validated analytical methods for crack growth analyses that account for the effects of various life enhancement processes, such as laser shock peening (LSP) and cold-worked holes. To support this objective, tasks included:

- Development and experimental validation of analysis methods to predict residual stress fields resulting from residual stress treatments.
- Development and experimental validation of analysis methods to predict crack growth in bodies containing residual stresses.
- Demonstration of the design tool capability for rotorcraft components.
- Quantification of the damage tolerance benefits for existing and new life enhancement processes for rotorcraft applications.

The development of a consistent and validated analytical approach for predicting the influence of residual stress treatments will enable wider use in rotorcraft structures.

1.2 BACKGROUND.

Life enhancement processes, such as shot peening, cold work, and cold-expanded bushings are now being used in many rotorcraft components, and LSP is now under consideration for some rotorcraft structures, such as gears. These processes result in improved fatigue life and crack growth times. The improvements in fatigue life are often not accounted for in design analysis, but are reflected for many components in the full-scale certification testing. The improved crack growth times lead to better damage tolerance capability. There has been some research on the effect of life enhancement processes on crack growth for rotorcraft structure, including:

- Development of superposition-based crack growth analysis in previous work at the Sikorsky Aircraft Corporation (SAC).

- Development of superposition and strip yield (crack closure) analyses for cold-worked holes in Federal Aviation Administration-(FAA)-sponsored work at Mississippi State University (MSU).

- Development of residual stress measurement and fatigue design for laser shock-peened components in Department of Energy (DOE), Department of Defense (DoD), and industry-sponsored projects at the University of California, Davis, and Hill Engineering, LLC (HE).

- Development of residual stress and crack growth analysis models in FAA-sponsored work at the University of California, Irvine.

However, additional research and development is needed to provide practical and validated analytical methods that can be used to take advantage of these processes in rotorcraft damage tolerance design and certification. To better implement rotorcraft damage tolerance, past research has indicated that it is important to be able to predict the effect of the life enhancement processes on crack growth in rotorcraft components. However, there are still technical issues that need to be addressed before the technology can be applied with confidence. Also, the analytical methods developed in the past research were approximate, not fully validated, and too complex for use in damage tolerance design applications.

Some of the technical issues that need to be fully understood are related to the difference between superposition and the FASTRAN nonlinear crack growth analysis. In a recent MSU cold-worked hole project, FASTRAN provided better predictions than superposition models for growth of through-thickness cracks at cold-worked holes. However, in these analyses, an approximation of the cold-work residual stresses was used in FASTRAN, and the technical reasons for the differences between FASTRAN and superposition were not investigated. Superposition is known to provide good crack growth predictions for cases involving multiple applied load distributions, such as axial load and bending. It may be that residual stresses do not behave as applied loads and, if this behavior can be characterized, then superposition may be an appropriate analysis method.

Another technical issue that needs to be addressed is that of developing practical analysis methods for the determination of residual stresses and practical means to introduce these stresses into the crack growth analyses codes. In the MSU cold work project, an approximation was used for the cold work residual stresses based on the application of a tensile overload. An improved method of cold-work residual stress analysis and a practical interface with the crack growth analysis needs to be developed. Also, the through-thickness residual stress distributions for cold-worked holes and the effect on through-thickness and corner cracks need to be evaluated.

It is important to develop experimental data on residual stress distributions and crack growth measurements in the residual stress fields to validate the analytical models. Also, it is important that the models be practical for use in a rotorcraft design environment and that their practical application to rotorcraft components be demonstrated.

1.3 RESEARCH OBJECTIVES.

The objectives of this research program were to:

- Develop methods to estimate residual stresses for residual stress treatment processes, such as cold working of holes, considering both finite element (FE) and specialized analytical methods. Three-dimensional (3D) FE simulations were used to reveal through-thickness residual stress variation and to account for reaming and slotting of cold-worked holes.

- Develop crack growth analysis approaches, including a two-dimensional (2D) approach for through cracks and a 3D approach for surface and corner cracks. The analyses included the effects of residual stress on crack growth, where residual stresses are introduced through direct simulation, numerical analyses, or experimental measurements. Analysis methods encompassed both crack closure (strip-yield) and linear-elastic superposition approaches in codes, such as FASTRAN.

- Provide for technical transfer to implement the analytical methods at the SAC.

- Collaborate with SAC to perform detailed analysis of specific rotorcraft components aimed at producing desired life and crack growth improvements in specific rotorcraft components.

2. LITERATURE SURVEY ON RESIDUAL STRESS ENHANCEMENTS.

Rotorcraft components operating under time-dependent loads are susceptible to fatigue failure. One potential method of increasing material resistance to fatigue is introducing compressive residual stress fields in critical zones. The beneficial compressive residual stress fields may be produced using many different life enhancement processes. These include shot peening, LSP, cold expansion (CX) of holes, and the implementation of cold-expanded bushings.

The improvements in fatigue life from the above-mentioned methods are often not included during the design analysis. Understanding the residual stresses created from these processes is

important to account for their benefits. Numerous articles have been published regarding the measurement and prediction of residual stresses.

This report presents a brief description of four life enhancement processes, and then reviews recently published research related to numerical and analytical methods to estimate the residual stress fields.

2.1 SHOT PEENING.

Shot peening is accomplished by bombarding a surface with small spherical particles called shots that are harder than the material being peened [3]. As a result of a shot impact, plastic deformation occurs at the surface layer of the material, which, in turn, creates beneficial compressive residual stresses due to restoring forces (figure 1).

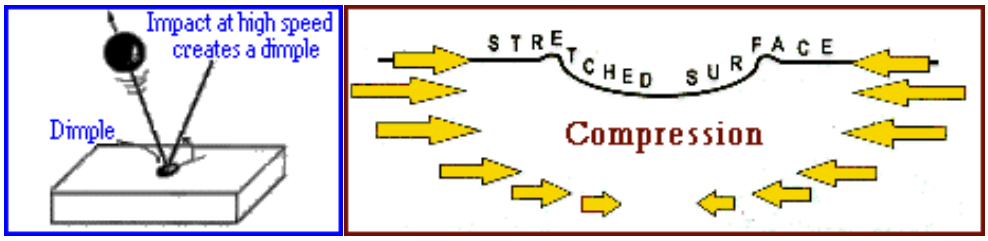

Figure 1. Shot Peening Process [3]

The peening process is controlled by the size, velocity, quality, and coverage area of the shot, as well as the thickness of the work piece. The influence of some parameters on the distribution of the residual stress, determined from experimental data, is shown in figure 2 [4]. The compressive stresses caused by shot peening increase the material resistance to fatigue cracking, stress corrosion cracking, corrosion fatigue, fretting, galling, and erosion [3]. However, if certain parameters of the process are not chosen carefully, shot peening may actually have a negative influence on the part life by inducing superficial defects, such as overlaps, microcracks, and surface imperfections [5].

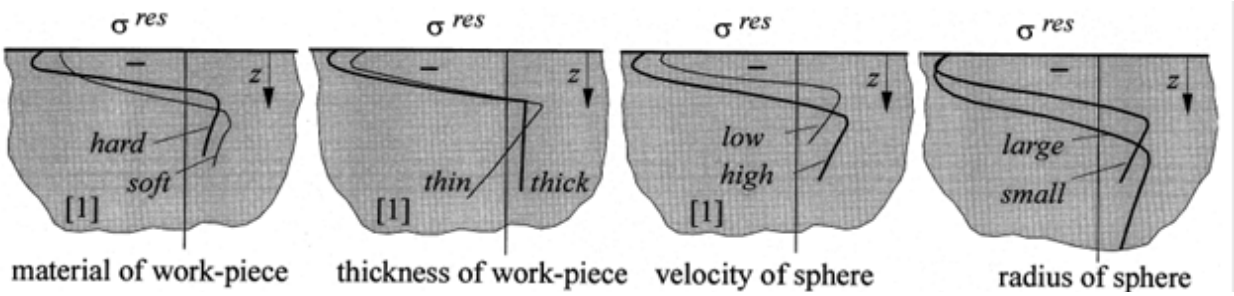

Figure 2. Influence of Shot Peening Parameters on Distribution of Residual Stresses

Numerous studies have been performed on the modeling and simulation of this life enhancement method. Residual stresses caused by shot peening were determined through experimental [6 and 7], analytical [8 and 9], or finite element methods (FEM) [4, 5, and 10-12]. One of the

first closed form solutions, which appeared in 1981 by Al-Hassani [8], used elastic-perfectly plastic material for the target work piece. Based on this model, Shen and Atluri [9] have recently developed a new theoretical model. Shen and Atluri extended Al-Hassani's solution by taking the primary shot peening factors into account, including the diameter and the velocity of the shot. The target material was assumed to be isotropic with multilinear strain hardening behavior. Three other assumptions were small displacement, elastic unloading before reversed yielding starts, and hydrostatic stresses that do not introduce plastic deformation. Results were compared with experimental data and fairly good agreements were observed. More details regarding this method can be found in reference 9.

Many authors have recognized FEM as the most suitable approach to analyzing the shot peening process. The FEM was used to determine the influence of the process parameters on the residual stress distributions [10 and 11]. Some researchers used 2D axisymmetric models [4 and 13], whereas many others worked with 3D models to simulate the process (figure 3) [5, 10, and 11]. Dynamic analyses were also performed [4, 10, and 11], while a static analysis [5] was adopted using an energy equivalence method to simplify the process.

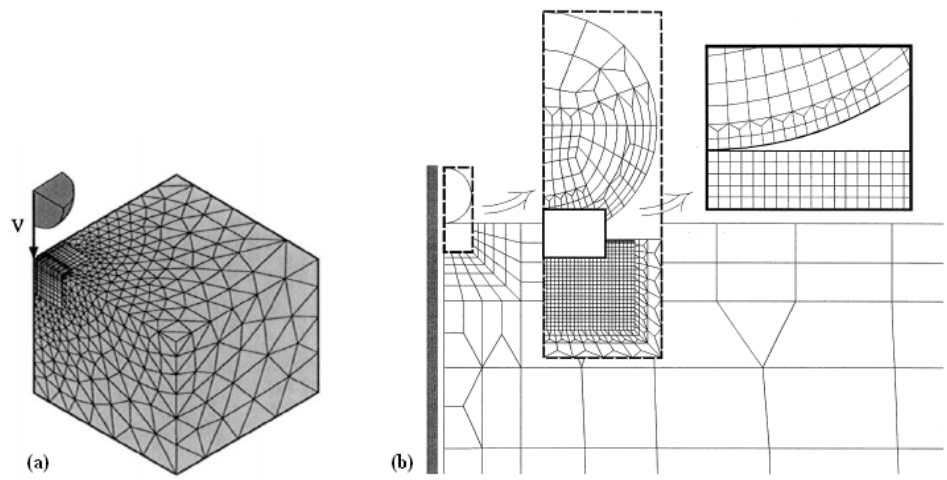

Figure 3. The FE Models for the Target Work Piece and the Shot: (a) 3D [11] and (b) 2D Axisymmetric Mesh [4]

Most FE studies modeled the shot as a rigid particle and the work piece as an elastic-plastic material with strain hardening behavior. However, according to El Tobgy et al. [8], assuming the shot as a rigid body leads to an overestimation of the residual stresses when compared with experimental results. Therefore, to increase accuracy in modeling the process, an elastically deformable shot needs to be used instead of a rigid shot.

El Tobgy et al. also considered a thermal displacement model, where the heat generated during the process could affect the material properties. The slight increase in the temperature caused by the process did not have a significant impact. It was concluded that the effect of the temperature change could be disregarded [8].

A contact model between the shot and the work piece was created using a Coulomb friction relationship [10]:

$$F_f = \mu \cdot F_n \tag{1}$$

where F_f is the friction force, F_n is the normal force, and μ is the coefficient of friction.

According to Meo and Vignevic [13], a significant difference can be found in the residual stress distribution when comparing frictionless contact results with results using a friction coefficient set to 0.1. However, negligible stress variation was experienced in the material for $0.1 < \mu < 0.5$ [10]. This leads to the conclusion that the friction between the shot and the work piece may not always be disregarded in process simulation.

2.2 THE LSP.

In the LSP process, a high-amplitude shock wave is driven into a material surface using a high-energy pulsed laser [14]. The material surface to be processed is coated with an ablative layer (typically black paint or tape) and a transparent overlay, such as flowing water. The laser pulse passing through the transparent layer vaporizes the ablative coating to form plasma. The plasma, produced between the material surface and the transparent overlay, rapidly expands, creating a high pressure shock wave, which propagates into the work piece as shown in figure 4 [14]. The planar shock wave created during the LSP process plastically deforms the material surface, leaving behind a layer of residual stress that is four or more times deeper than that attainable from shot peening [15].

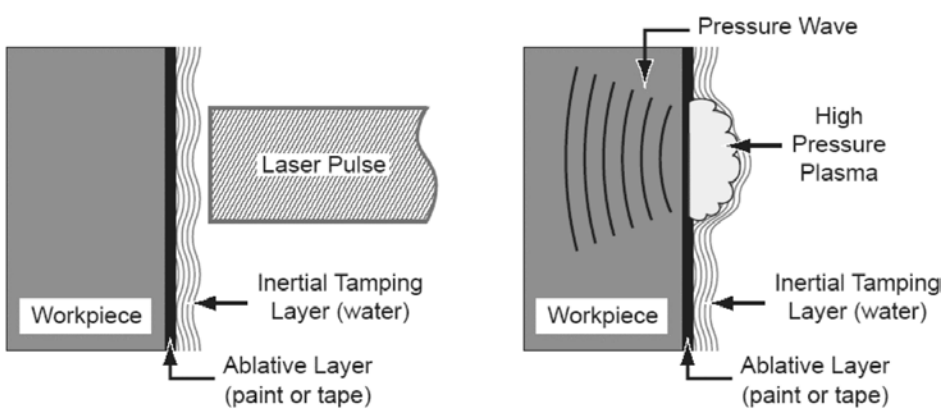

Figure 4. The LSP Process [14]

Even though LSP is known as a more costly and time-consuming process compared to shot peening, it is emerging as a viable surface treatment that could be used for more expensive and critical parts [3 and 16]. This process is particularly beneficial for treating materials in complicated configurations, such as fastener holes in aircraft structures and refurbished fastener holes in old aircraft, in which the possible initiation of cracks may not be noticeable by inspection [17].

There has been much experimental work performed on LSP, but only a relatively small amount of work has been done on the development of analytical methods to predict residual stresses. According to Ding and Ye [17], the first analytical model for predicting the residual stress induced by LSP was developed by Ballard [18]. In this model, the material was assumed to be elastic-perfectly plastic with uniaxial strain conditions.

The surface plastic strain from Hooke's law is expressed as:

$$\varepsilon_p = \frac{-2HEL}{3\lambda + 2\mu}\left(\frac{P}{HEL} - 1\right) \tag{2}$$

where HEL is the Hugoniot elastic limit, P is the pressure, and λ and μ are Lame's constants [18]. For the square laser spot on the target, the surface residual stress can be calculated by:

$$\sigma_x^{surf} = \sigma_y^{surf} = \sigma_o - \left(\mu \cdot \varepsilon_p \frac{1+\nu}{1-\nu} + \sigma_o\right) \times \left[1 - \frac{4\sqrt{2}}{\pi}(1+\nu)\frac{L_p}{a}\right] \tag{3}$$

where a is the edge length of a square laser spot, σ_o is the initial surface residual stress, and L_p is the plastically affected depth, which can be determined from the following equation:

$$L_p = \left(\frac{C_{el}C_{pl} \cdot \tau}{C_{el} - C_{pl}}\right) \times \left(\frac{P - HEL}{2HEL}\right) \tag{4}$$

where τ is the pressure pulse duration, and C_{el} and C_{pl} are the elastic and plastic velocities that are calculated from:

$$C_{el} = \sqrt{\frac{\lambda + 2\mu}{\rho}} \tag{5}$$

$$C_{pl} = \sqrt{\frac{\lambda + 2\mu/3}{\rho}} \tag{6}$$

where ρ is the target material density [18].

Braisted and Brockman [16] pioneered the use of the FEM to predict residual stresses from the LSP treatment of surface with a circular laser spot [19]. They also assumed the work piece material to be elastic-perfectly plastic and employed an axisymmetric model to simulate one-sided peening of a semi-infinite solid. The model was composed of finite and infinite elements (see figure 5). A combination of the ABAQUS/Explicit and ABAQUS/Standard FE codes was used to solve the problem. First, ABAQUS/Explicit analysis was used to simulate plastic deformation due to shock waves. Then, ABAQUS/Standard was used to solve the residual stress

fields in static equilibrium. To simulate multiple peening, an output file from the standard analysis was read into ABAQUS/Explicit and the procedure was repeated [16].

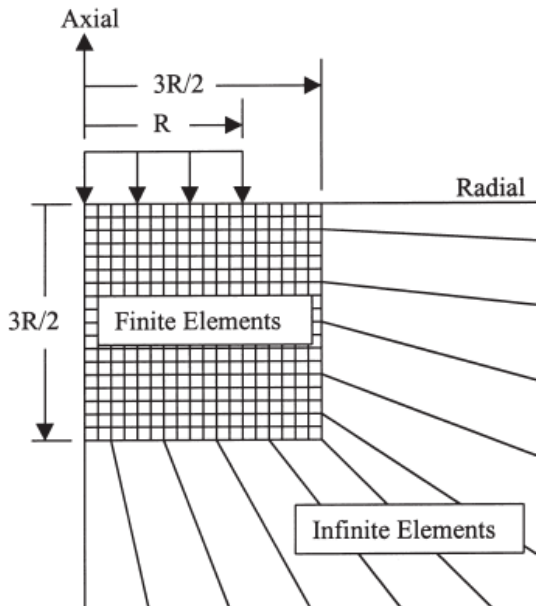

Figure 5. One-Sided LSP Model [16]

Ding and Ye [17] continued exploring the use of the FEM to simulate LSP by developing a 3D FE model. They analyzed the LSP treatment of a material surface with a square, instead of circular, laser spot and found that the former produced better results in terms of residual stress distribution. Ding reported that a circular laser spot led to a lack of compressive residual stresses at the center of the treated zone due to focused stress waves [17]. For single LSP impact, figure 6a shows the 3D FE model and figure 6b shows the residual stress distribution with respect to different impact pressures. The same authors used FEM to simulate two-sided LSP of thin sections [20].

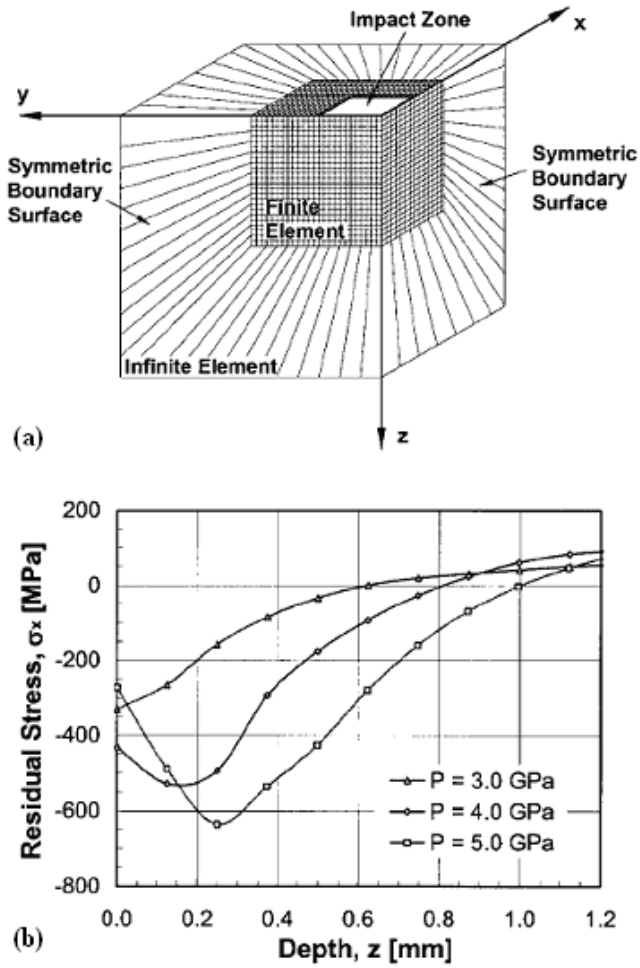

Figure 6. Single LSP Impact: (a) The 3D FE Model and (b) Residual Stress Distributions With Respect to Different Impact Pressures [17]

2.3 COLD WORKING OF HOLES.

In cold-expanded holes, a compressive residual stress region is created by radially expanding the hole using a tapered mandrel and a split sleeve (figure 7(a)). The diameter of the mandrel and the sleeve is greater than that of the hole. When the mandrel, fitted in the lubricated sleeve, is pulled through the hole, it expands the hole and produces yielding. As the mandrel is removed, a beneficial compressive residual stress is produced (figure 7(b)), after which the hole is reamed to the final size [21].

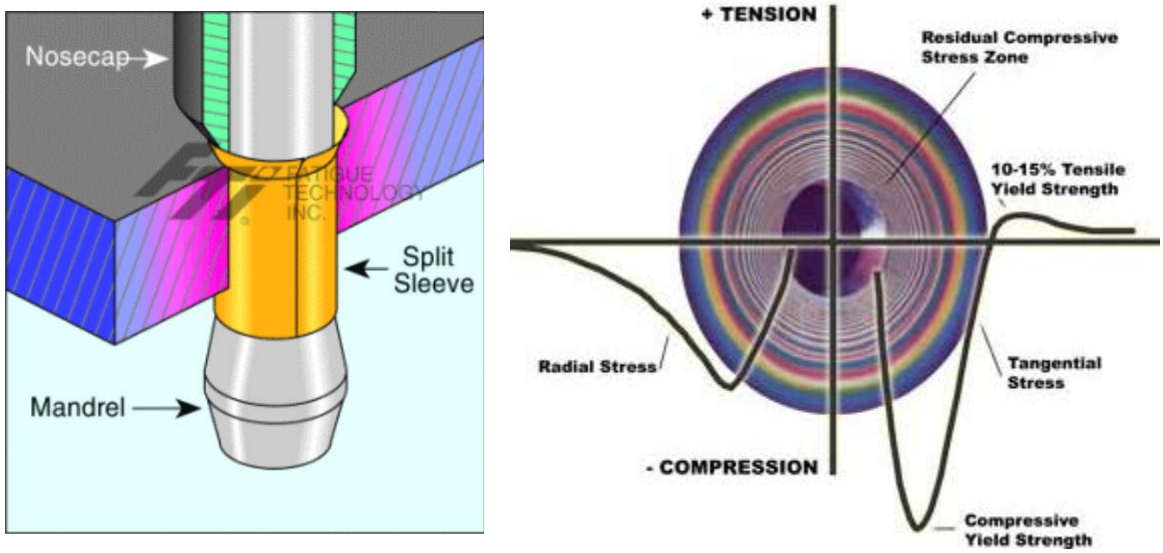

(a) (b)

Figure 7. Fatigue Techonology, Inc. (a) Split Sleeve Cold Expansion Process and (b) Residual Stress Distribution [3 and 21]

Many analytical and numerical studies have been conducted and published regarding the prediction of residual stresses caused by cold expansion. Assuming small strain and plane stress conditions in 2D, Ball [22] obtained a closed-form elastic-plastic solution for the radial expansion of fastener holes. He expressed the uniaxial strain hardening behavior of the material in the form of a power law:

$$\varepsilon = \frac{\sigma}{E}\left|\frac{\sigma}{\sigma_y}\right|^{n-1} \quad \text{for } |\sigma| > \sigma_y \tag{7}$$

where σ, ε, and σ_y are the stress, the strain, and the yield strength, respectively; and E and n are the modulus of elasticity and the strain hardening exponent of the material.

Ball idealized the elastic mandrel insertion by a radial pressure applied on the hole surface. He developed a relationship between the interface pressure and the level of interference. The hole unloading process was modeled using a reverse yielding criterion. A more detailed explanation of this technique can be found in reference 22. Figure 8 shows the closed-form radial and tangential stress solutions for various levels of interference (I_o).

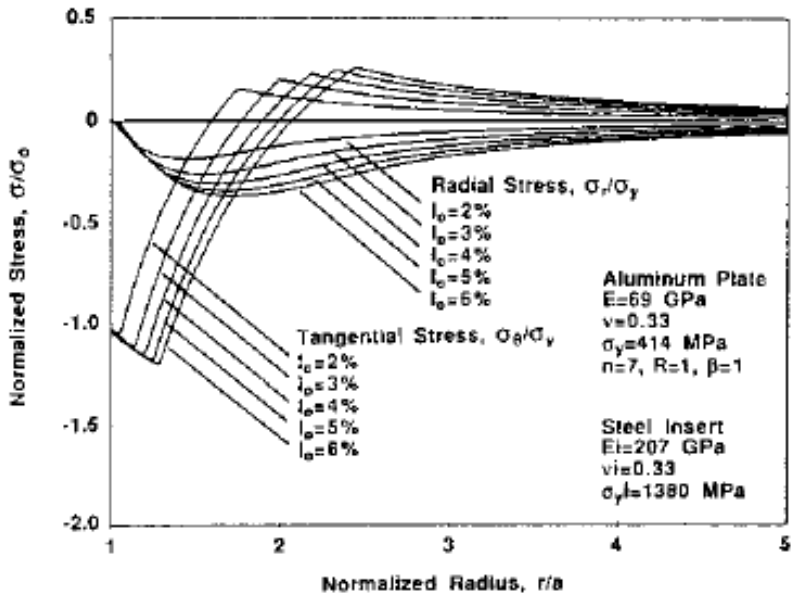

Figure 8. Dependence of Radial and Tangential Stress in a Wide Aluminum Plate on the Level of Interference With a Steel Pin [22]

Recent studies used the FEM, rather than a closed-form solution approach, to simulate the CX process. Authors emphasized the importance of 3D analysis because of the variation of the residual stress contour throughout the thickness [23-25]. Because 2D simulation alone did not manage to estimate the residual stress due to cold work, Priest et al. [23] showed that existing analytical models did not provide accurate predictions.

Even though CX is a dynamic process, according to Kang et al. [25], it could be modeled as a quasi-static test because the stress-strain response of the material should not be significantly different. Studies divided the process into three steps: (1) hole expansion, (2) hole recovery, and (3) finish reaming.

The hole-expansion process was simulated by the addition of uniform displacements on the nodes at the hole edge of the FE model [23-28]. Next, the hole recovery was accomplished by removing the preapplied boundary condition and the reaming was simulated by eliminating a layer of nodes at the hole surface.

Recent studies included the rigid mandrel and the elastic sleeve in finite element analysis (FEA) to attain a more realistic simulation of the process. De Matos et al. [24] compared residual stresses determined from 2D analysis, using rectangular and cylindrical plates, and between 2D axisymmetrical and 3D methods for the same hole dimensions (figure 9). Results from the work of De Matos et al. show that the 2D model overpredicts residual compressive stress. The research of Kang et al. [25] resulted in the same conclusion. The stress state can be most accurately represented by plane-stress assumption at the surface and plane-strain assumptions at the mid-section.

Residual stress fields from 2D axisymmetric and 3D models were in good agreement. However, the 2D axisymmetric model predicted a greater amount of hole enlargement (deformation). De Matos stated that this might be because he used fewer elements through the thickness of the 3D model [24] (see figure 9).

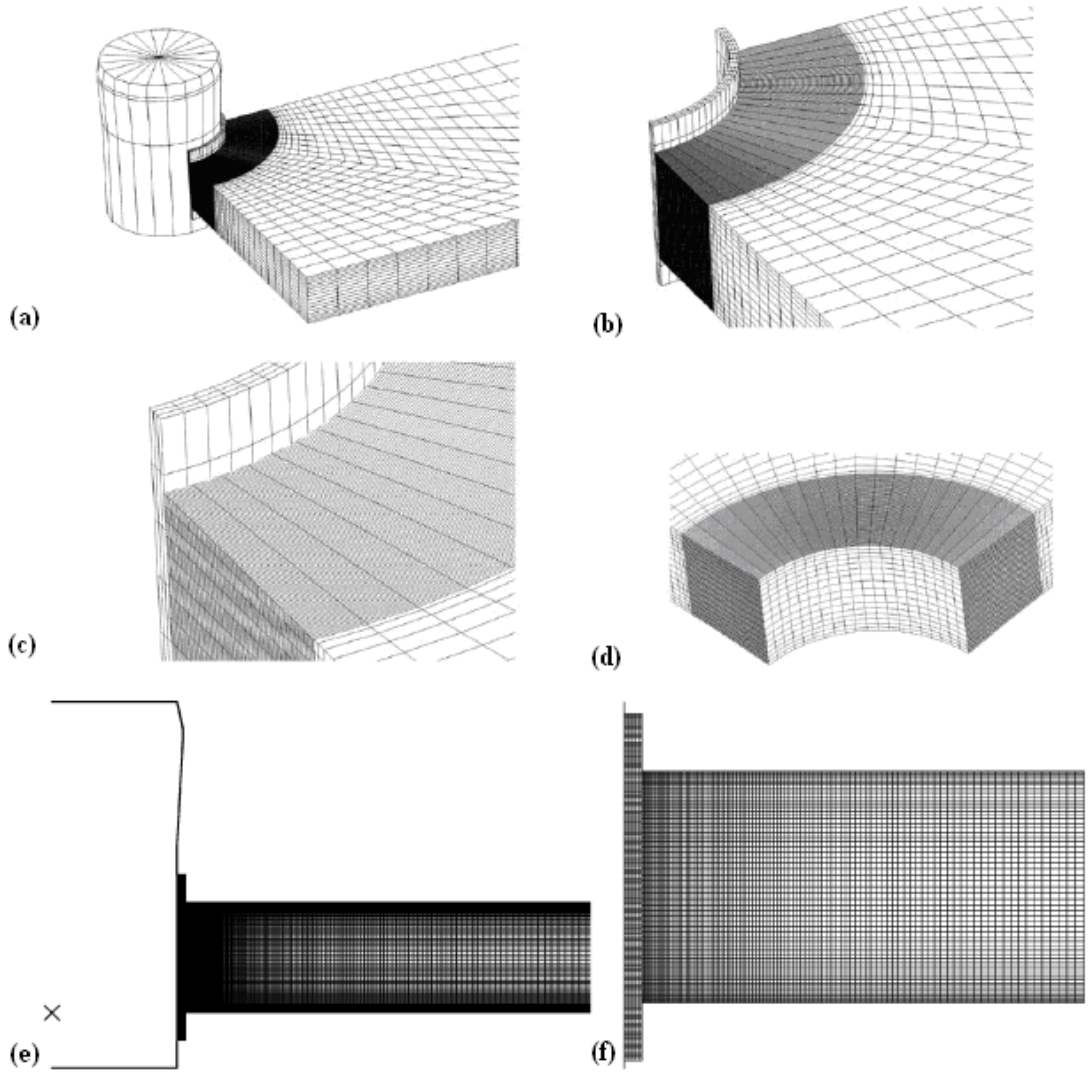

Figure 9. Details of the 3D FE Model Used for the Cold Working Process Simulation: (a) Model Assembly; (b) Plate and Sleeve Assembly; (c) Plate and Sleeve Mesh, Detail; (d) Hole Mesh, Detail; (e) Detail Near the Mandrel; and (f) Sleeve and Plate Near the Hole [24]

De Matos introduced the residual stress fields using two methods: (1) uniform expansion, and (2) actual cold-working process. Frictionless conditions were assumed between the mandrel and the sleeve, and between the sleeve and the plate material in method 2. This assumption was justified by lubricated surfaces. The mandrel was modeled as a rigid body, whereas the sleeve was modeled as a linear elastic material. Results from these two approaches (i.e., uniform expansion and the cold-working process) were significantly different, as shown in figure 10.

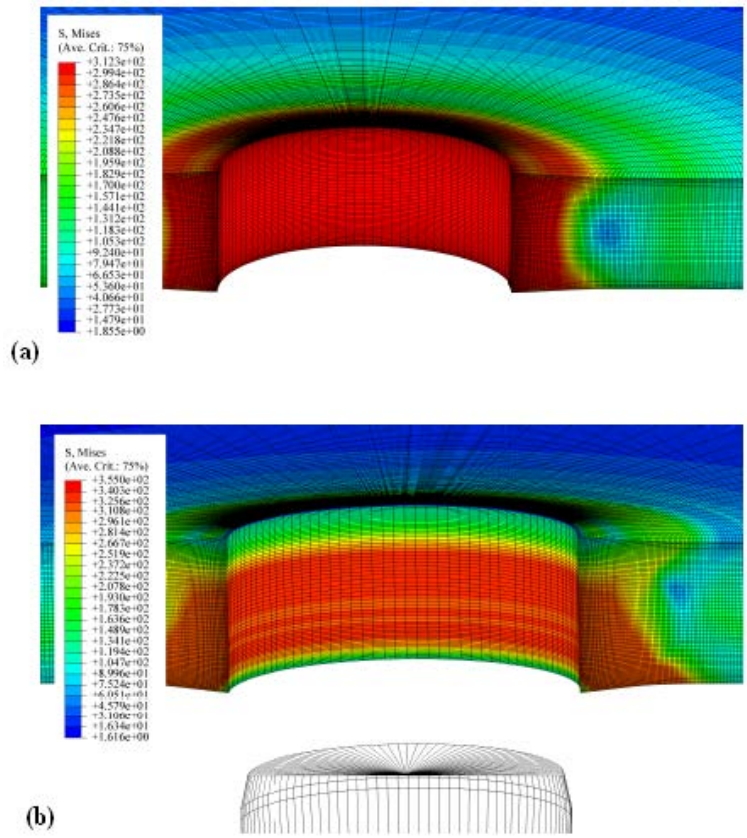

Figure 10. von Mises Residual Stress Field After the Hole Deformation Process: (a) Uniform Hole Expansion and (b) Cold Working Process Using a Rigid Mandrel [26]

Kim et al. [27] studied the influence of adjacent holes when estimating the residual stress fields caused by CX (figure 11). Two cases were considered: (1) simultaneous CX, and (2) sequential CX. The results showed that the simultaneous CX led to much higher compressive residual stress than the sequential CX.

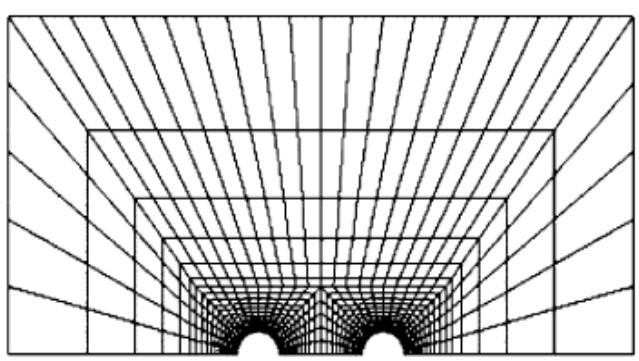

Figure 11. The FEA Results With Two Adjacent Holes [27]

The material hardening behavior in all of the studies discussed was modeled using experimental data points from a tensile test of the material. Data points above the yield stress were needed for

numerical simulations because the plate material experienced yielding when cold-worked. Both kinematic and isotropic plastic hardening of the material was considered. Kang et al. [25] discovered no differences in residual stress solutions at the hole surface using both kinematic and isotropic hardening. However, Priest's work [23] predicted higher compressive tangential residual stresses with isotropic hardening when compared with kinematic hardening, suggesting that the Bauschinger effect can influence the results. According to Priest, to have more accurate predictions, further information is needed about the compressive behavior of the material [23].

To verify the calculated FEA results, different experimental techniques have been used to measure the residual stresses in cold-expanded holes. For example, x-ray diffraction is a nondestructive method, which involves the measurements of stresses in the surface layers of the material [23]. There are other experimental residual stress measurement techniques, such as neutron diffraction, Sachs' cutting method, and photoelastic and optical strain measurements [28]. Experimental measurements and FEA predictions of residual stresses were not in good agreement [23 and 29]. Some justified this as a result of experimental measurements that were averaged over an irradiated volume, while others said it was due to the presence of preexisting residual stresses induced through specimen preparation. Good agreement was observed by Kang et al. and Kim et al. [25 and 27].

2.4 COLD-EXPANDED BUSHING.

The use of cold-expanded bushings is a similar process (see figure 12) to CX of holes, except that the disposable split sleeve is replaced by a bushing [3]. The lubricated bushing is initially placed in the hole with a clearance fit. Then, with the help of an oversized tapered mandrel, the bushing is cold-expanded into the hole. As a result, beneficial compressive stresses are created around the hole and the bushing is installed with a high interference fit. The fatigue life improvement because of this life enhancement method is typically 3:1 [30].

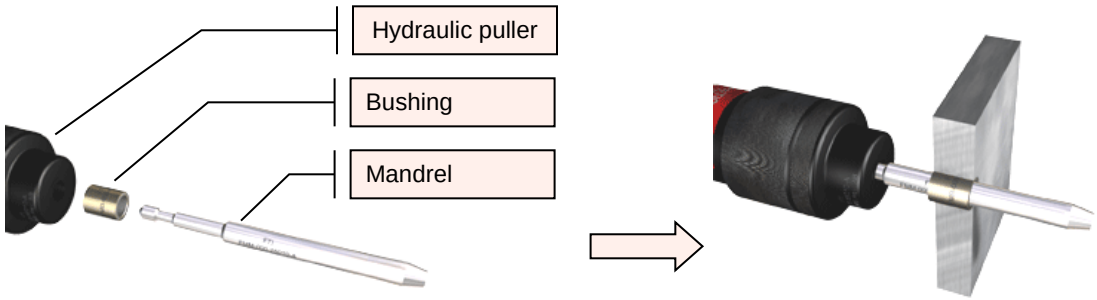

Figure 12. Cold-Expanded Bushing Process [30]

Only a few articles have been published by the scientific community regarding the analysis of cold-expanded bushings, perhaps because of the similarity between this process and the CX of holes. Pipkins [31] performed a numerical study to understand the effectiveness of this process in fastener holes near the edge of aluminum panels. He developed a 3D FE model (figure 13) and assumed both the panel and the bushing to be elastic-perfectly plastic with isotropic hardening. The cold-expanded bushing was simulated by applying uniform radial displacements to the interior surface of the bushing. The residual stress fields were determined by removing the

preapplied displacement boundary condition and allowing the bushing and the work piece material to experience a spring back.

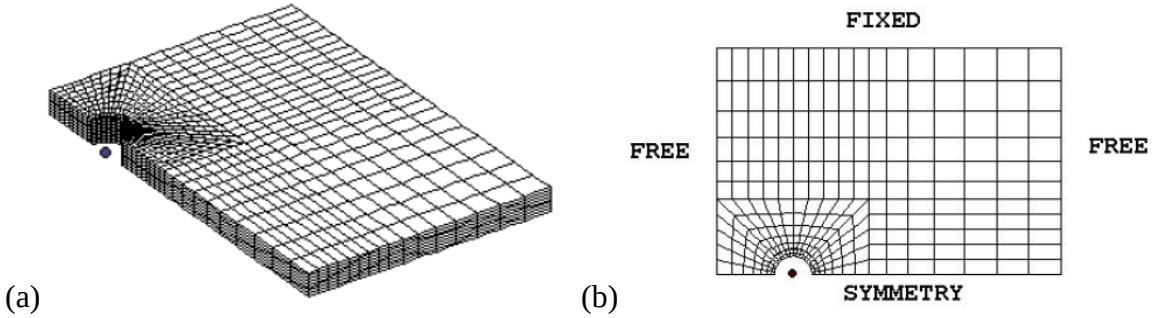

Figure 13. The 3D FE Model Mesh: (a) BCs and (b) Cold-Expanded Bushing [29]

After the residual stress fields were determined, cracks with various sizes and shapes were introduced at the hole, and linear elastic fracture mechanics analyses were carried out to estimate the increase in fatigue life due to the cold-expanded bushing. It was concluded that this process could be an effective method of repairing cracking at fastener holes, thereby increasing fatigue life. However, if the hole is located close to the edge of the panel, the size of the compressive residual stress field becomes small and significant tensile residual stresses may develop at the free edge of the panel. This may result in a range of effects from minor to detrimental on the fatigue life [31].

Lanciotti [32] performed a more realistic simulation of a cold-expanded bushing, and included the mandrel and the bushing in his analysis. Stress-strain curves of 7050-T7451 aluminum alloy for the specimen and steel 17-4 PH for the bushing were considered. The steel mandrel was modeled to be elastic and the cold-expanded bushing process was simulated by pulling the mandrel through the hole of the specimen. The experimental and numerical results were in good agreement, as shown in figure 14.

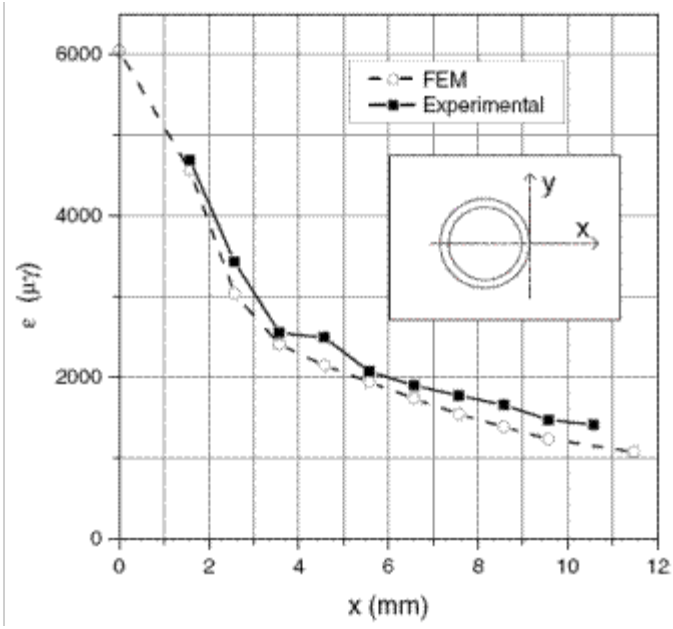

Figure 14. Experimental and FEM Residual Strain Results After Bushing Installation [32]

Lanciotti [32] used FEM to estimate residual stress fields that were caused by the installation of a shrink-fit bushing with a 0.04 interference. The stress field for this case was completely different, where bushings produced tensile elastic stresses in the lug, as shown in figure 15.

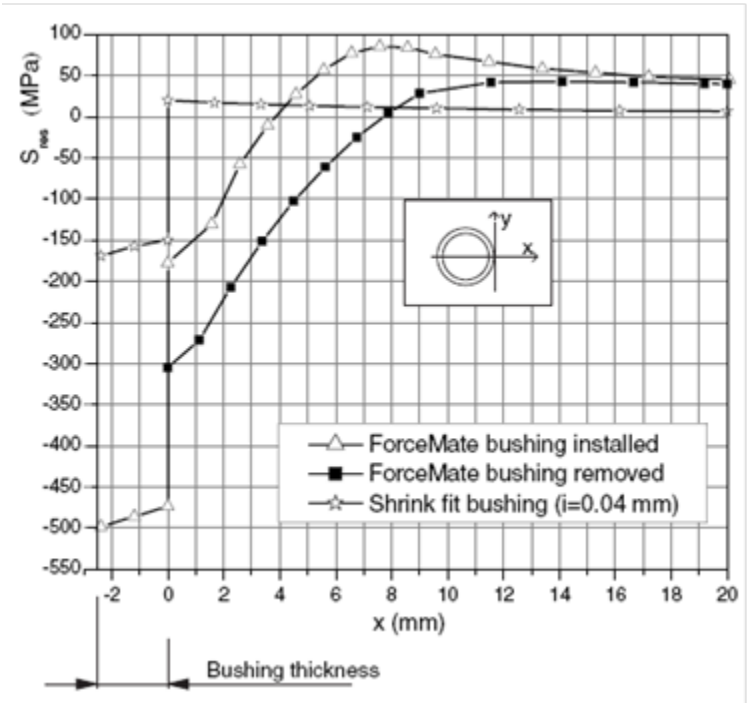

Figure 15. Residual Stresses With Bushing Installed, After Bushing Was Removed and Caused by Shrink-Fit Bushing [32]

2.5 SUMMARY.

A literature review was done regarding four life enhancement processes. Numerous publications were found concerning the estimation and modeling of residual stresses due to shot peening, LSP, and the CX of holes. Only a few articles were found regarding the analysis of cold-expanded bushings, perhaps because of the similarity between this process and the CX of holes.

Studies indicate that the FEM is emerging as a primary tool to model and analyze these types of problems. Advances in computer hardware and software are leading to more realistic process simulations. Among all existing FEA tools, ABAQUS was preferred in most of the studies that are mentioned in this report.

In general, the analysis of the cold expansion of holes and cold-expanded bushings has assumed frictionless conditions between the mandrel and the sleeve, and between the sleeve and the plate material. This assumption was justified by lubricated contact surfaces.

3. MATERIALS.

Two high-strength aluminum alloy sheet materials commonly used for rotorcraft structures were selected for the test and analysis program. One material was 7075-T6 aluminum alloy (bare and clad) sheet and the other was the 7075-T6511 aluminum alloy extrusion. For the 7075-T6 aluminum alloy, there were two sheet thicknesses considered (2- and 4.8-mm thick). The 7075-T6 aluminum alloy was chosen for the open and loaded hole test specimens because of its extensive application in rotorcraft and the large existing NASGRO® material database [33]. The fastened joint test article was constructed of 7075-T6511 extruded aluminum alloy. The T6511 heat treatment is a common standard for aerospace 7075 extrusions. This alloy was chosen for the nested angle component tests, because of: (1) its extensive use in rotorcraft structural configurations, (2) experience with this alloy on several nested angle tests on other programs, and (3) its extensive application in rotorcraft and large existing NASGRO material database.

3.1 TENSILE PROPERTIES.

Mechanical properties for the 7075-T6 and 7075-T6511 aluminum alloy sheet material are listed in table 1, as found in MIL-HDBK-5H [34]. The results for the T6511 aluminum alloy were determined by private communication with Alcoa, Inc.

Table 1. Mechanical Properties for 7075-T6 (clad and bare) and 7075-T6511 Aluminum Alloy

Property	T6		T6511
	Clad	Bare	Bare
Yield stress, σ_{ys}, MPa	448.0	483.0	554.00
Ultimate tensile strength, σ_u, MPa	503.0	538.0	600.00
Modulus of elasticity, E, GPa	72.5	72.5	71.60
Poisson's ratio, ν	0.3	0.3	0.33

3.2 FATIGUE CRACK GROWTH PROPERTIES.

An effective SIF-against-rate relationship had previously been obtained on the thin sheet 7075-T6 aluminum alloy [35 and 36] (the yield stress was 520 MPa and the ultimate tensile strength was 575 MPa). Figure 16 shows this correlation on the data generated on middle-crack-tension (M(T)) specimens (w = 38 mm) [37]. The data generated for three stress ratios correlated very well, except in the near-threshold regime. The baseline relation is fitted to the mean of these data, as shown by the solid curve with solid symbols. The solid symbols are the table-lookup values used in the FASTRAN code. The flat-to-slant crack growth (constraint-loss) regime was defined and the values of constraint (α) were established from variable-amplitude load tests [36]. The location and constraint values for the constraint-loss regime are best established using variable-amplitude fatigue crack growth rate tests instead of constant-amplitude tests. Figure 17 shows another data set for the T6-7075 aluminum alloy. Hudson obtained these data in 1969 [37] on large width M(T) specimens (w = 152.4 mm), which exhibited some differences in the high-rate regime. For rates less than about 10^{-9} m/cycle, the baseline curve (solid curve and solid symbols) was fit to small crack data [37]. This relationship will be used throughout the remainder of the report. In figure 17, the solid lines show the baseline effective SIF-against-rate relation used in the FASTRAN code for the 7075-T6 aluminum alloy material, and is shown in table 2.

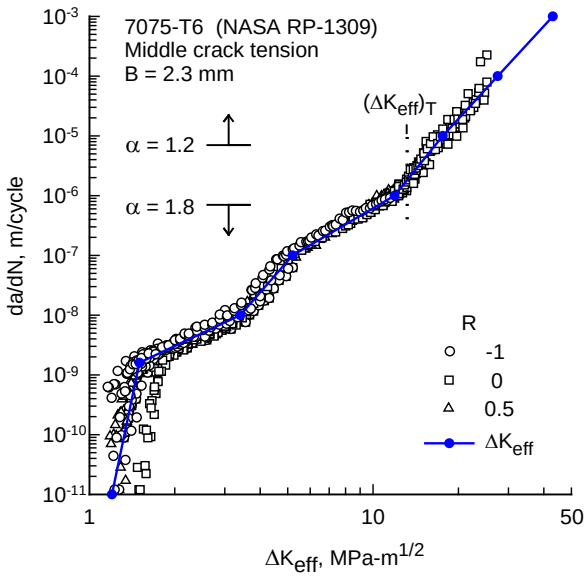

Figure 16. Effective SIF Range-Against-Rate for 7075-T6 Aluminum Alloy Sheet for Various Stress Ratios on Small-Width M(T) Specimens

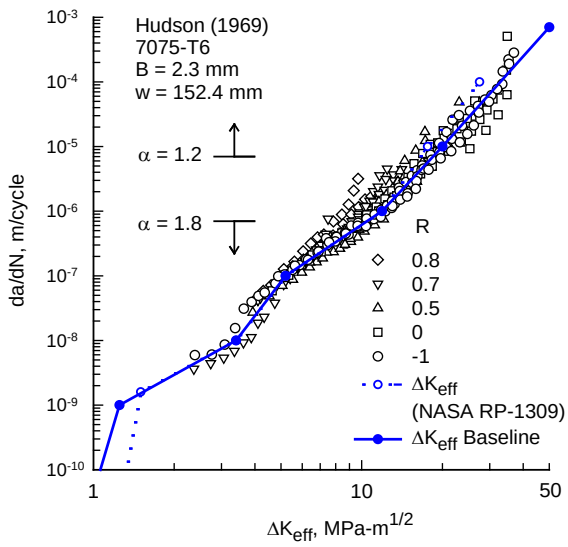

Figure 17. Effective SIF Range-Against-Rate for 7075-T6 Aluminum Alloy Sheet for Various Stress Ratios on Large-Width M(T) Specimens

Table 2. Effective SIF-Against-Rate Relationship for 7075-T6 Aluminum Alloy

ΔK_{eff}, MPa-m$^{1/2}$	da/dN, m/cycle
0.90	1.00e-11
1.25	1.00e-9
3.40	1.00e-8
5.20	1.00e-7
11.9	1.00e-6
20.0	1.00e-5
50.0	7.00e-4
88.0	1.00e-2
α = 1.8	7.00e-7
α = 1.2	7.00e-6

The crack growth relation used in FASTRAN is:

$$da/dN = C_{1k}\,(\Delta K_{eff})^{C_{2k}}\,[1 - (\Delta K_o / \Delta K_{eff})^p]/[1 - (K_{\max} / K_{Ie})^q] \tag{8}$$

where C_{1k} and C_{2k} are the coefficient and power for each linear segment (k), as shown in figure 17, ΔK_{eff} is the effective SIF, ΔK_o is the effective threshold, $K_{\max}$ is the maximum SIF, K_{Ie} (or C_5) is the elastic fracture toughness (which is, generally, a function of crack length, specimen width, and specimen type), and p and q are constants selected to fit test data in either the threshold or fracture regimes. Whenever the applied $K_{\max}$ value reached or exceeded K_{Ie} (or C_5), the specimen or component would fail. The two equations used to express the threshold ΔK_o as a function of stress ratio are as follows:

$$\Delta K_o = C_3\,(1 + C_4\,R) \;\text{ or }\; \Delta K_o = C_3\,(1 - R)^{C_4} \tag{9}$$

Here, ΔK_o was set to zero (C_3 = 0) and the threshold behavior was modeled with multilinear segments. The value of q was set to 2. The table-lookup form is used because many materials, especially aluminum alloys, show sharp changes in the crack growth rate curves at unique values of rates. These sharp changes have been associated with monotonic and cyclic plastic-zone sizes, grain sizes, and environments [37-39].

4. CRACK GROWTH ANALYSIS METHODS WITH RESIDUAL STRESSES.

In the past, elastic superposition methods have been used in crack growth models to account for the effects of various forms of residual stresses. However, this approach assumes that the residual stress field is unaffected by crack growth and loading history. Because crack growth

involves severe plastic deformations around the crack fronts and plastic deformations along the crack surfaces, there is a possibility that the compressive residual stress fields (because of shot peening or cold working) may diminish as the crack grows through the plastic region caused by the residual stress enhancement, thus negating some of the benefits of the residual stresses.

4.1 LINEAR SUPERPOSITION.

Linear superposition techniques are often used when assessing the effects of a known residual stress field on fatigue crack growth. The superposition involves the computation of a residual SIF, K_{rs}, which is associated with the initial pre-existing residual stress field. In the literature, it is common to use the Green's function (GF) or the weight function to calculate K_{rs} due to residual stress distributions, as shown in appendix A for the C(T) specimen. This SIF is then added to the SIF that results from the external applied loads to give the total resultant SIF for the maximum and minimum loads (see equations 10 and 11):

$$K'_{\max} = K_{\max} + K_{rs} \tag{10}$$

$$K'_{\min} = K_{\min} + K_{rs} \tag{11}$$

The SIF range and stress ratio is then calculated as the following:

$$\Delta K = K'_{\max} - K'_{\min} \tag{12}$$

$$R = K'_{\min}/K'_{\max} \tag{13}$$

The SIF range (ΔK) does not change because the SIF from the residual stress is negated; however, the stress ratio R holds the dependence of the SIF ratio from the residual stress. Fatigue crack growth rate is predicted using a correlation of the form:

$$da/dN = f\,(\Delta K, R) \tag{14}$$

The superposition method is widely used, but the dependence of R results in more rigorous calculations. One approach to account for the R-effect on crack growth rate data is from a crack closure model, as used herein. In terms of an effective SIF range, the crack growth rate is:

$$da/dN = C\,(\Delta K_{eff})^{n} \tag{15}$$

where C and n are material constants, $\Delta K_{eff} = U\,\Delta K$ and $U = (1 - S_o/S_{\max})/(1 - R)$. The crack opening stress ratio is of the form:

$$S_o/S_{\max} = f\,(R, S_{\max}/\sigma_o, \alpha) \tag{16}$$

where $S_{\max}$ is the maximum applied stress, σ_o is the material flow stress, and α is a constraint factor (α = 1 for plane stress and α = 3 for plane strain conditions), which accounts for the effects of state-of-stress around a crack front. Here, the $S_{\max}/\sigma_o$ ratio was selected as 0.3, which

is a common practice in the NASGRO life prediction code to simplify the evaluation of crack opening stresses. The crack opening stress ratio, S_o/S_{max}, is also equal to the K_{op}/K'_{max} ratio. The K_{op} value is used in appendix B to calculate the effective SIF range that accounts for the effects of residual stresses using the linear superposition method with a linear cumulative damage crack growth methodology.

The superposition technique is used extensively because of its simplicity, which some researchers have criticized, because it considers only the initial residual-stress field that exists in the uncracked structure, with no acknowledgement of the redistribution of residual stress that occurs as the propagating fatigue crack penetrates the residual stress field with its free or partially free surfaces [40-47]. Other researchers have argued that the redistribution of residual stress is inconsequential [48 and 49].

Regarding linear elastic materials, Bueckner [50] demonstrated mathematically that SIFs resulting from a given applied loading may be computed using the stress distribution in the uncracked structure. Heaton [51] presented a mathematically rigorous proof that generalizes Bueckner's formulation to include both thermal and residual stress fields. The work of Bueckner and Heaton suggests that, for linear elastic materials, the redistribution of applied and residual stresses due to fatigue crack propagation is inconsequential when computing SIFs and subsequent fatigue crack growth through use of equations 12 and 14.

Bueckner's and Heaton's conclusions are applicable to linear elastic materials only. The existence of plastic deformation at the crack tip, even under small-scale yielding conditions, will produce crack-generated residual stresses at the crack tip [52 and 53] and closure along the crack surface of the propagating crack [54 and 55]. The superposition methodology is unable to account for the influence of these effects. Consequently, the use of linear elastic superposition techniques for prediction of the effects of residual stress on fatigue crack propagation may result in crack growth predictions that correlate poorly with experimental observations [43].

4.1.1 AS-MACHINED COMPACT SPECIMENS.

Before analyzing the laser shock-peened compact (C(T)) specimens, it was important to analyze an as-machined C(T) specimen made of the 7075-T6 aluminum alloy material to validate the linear superposition code, *KRS.for*, as shown in appendix B. The C(T) specimens were designed based on the American Society for Testing and Materials (ASTM) E-647 [56] standard with a width (W) of 50.8 mm. A constant-amplitude fatigue crack growth test was conducted at a maximum load P_{max} of 0.98 kN at R = 0.1 with an initial crack length of about 11 mm. Figure 18 shows the measured (symbols) and predicted results (dashed curve) of crack length-against-cycles. The predicted results agreed well with the C(T) test data and verified the *KRS.for* code for no residual stress.

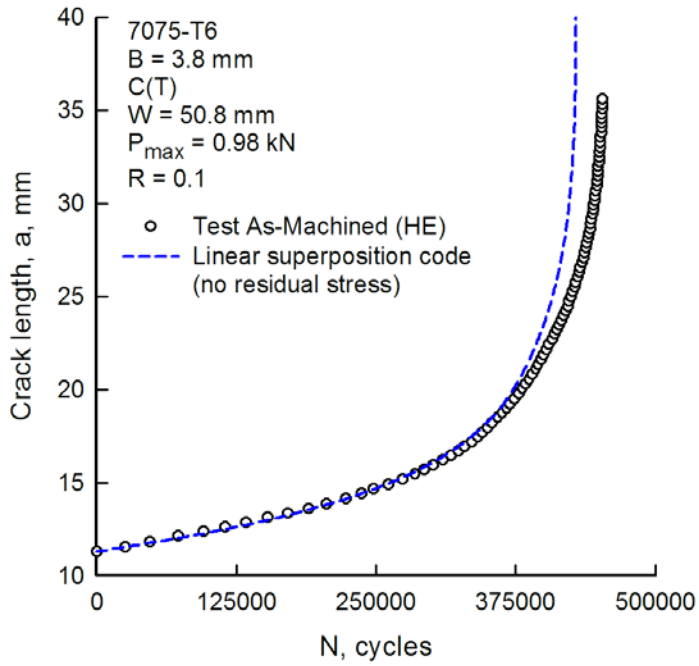

Figure 18. Measured and Calculated Crack Length-Against-Cycles for As-Machined C(T) Specimen Using Linear Superposition Code

4.1.2 LASER SHOCK-PEENED C(T) SPECIMENS.

To measure the effects of LSP residual stresses on fatigue crack growth, C(T) specimens were peened with parameters that should induce nearly constant through-the-thickness residual stresses [57]. Again, C(T) specimens with a width (W) of 50.8 mm and a thickness (B) of 3.8 mm were tested. The laser peening process was performed at Lawrence Livermore National Laboratories with a high peak power Neodymium doped glass slab laser. The LLNL laser has the capability of generating up to 100J of energy, a pulse width of 10 to 100 ns, an average power of 600W, and the ability to be fired at a repetition of 6 Hz. Details of the laser system were discussed by Dane [58] and its use in LSP was discussed by Hammersley et al. [59]. The contour method, a recently developed residual stress measurement technique [60], was used to determine the through-thickness residual stress distribution of the laser shock-peened C(T) specimens, as shown in figure 19. The darkened area shows the laser shock-peened region on the C(T) specimen and the symbols show the residual stresses measured on two different specimens. The solid curve is a tenth-degree polynomial chosen to fit the experimental measurements. The σ_{rs} curve was slightly revised to maintain static equilibrium.

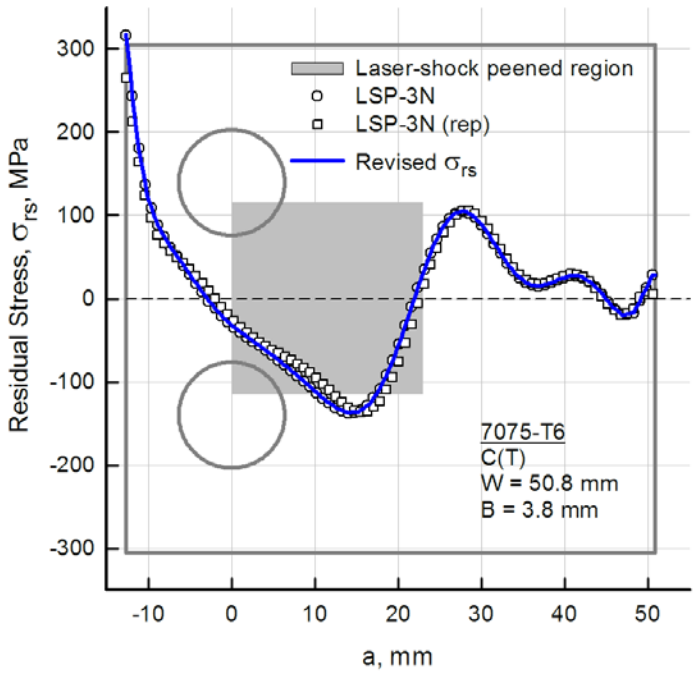

Figure 19. Measured Residual Stresses in Laser Shock-Peened C(T) Specimens

The Wu-Carlsson [61] weight function method was then used to generate the residual SIFs, K_{rs}, from the residual stresses. Figure 20 shows these results with the thin, solid curve as a function of crack length. A large compressive SIF occurred at a crack length of about 21 mm. The thick, solid curve represents the K_{rs} values determined from the GF equations given in appendix A. The GF method produced a similar distribution, but with different magnitudes of residual SIFs. The two tests produced a minimum K_{rs} of approximately -17 MPa√m, whereas the weight function method produced -15.4 MPa√m and the GF method produced -12.6 MPa√m. More research is needed to determine the explanation for the large differences between the weight function and the GF methods.

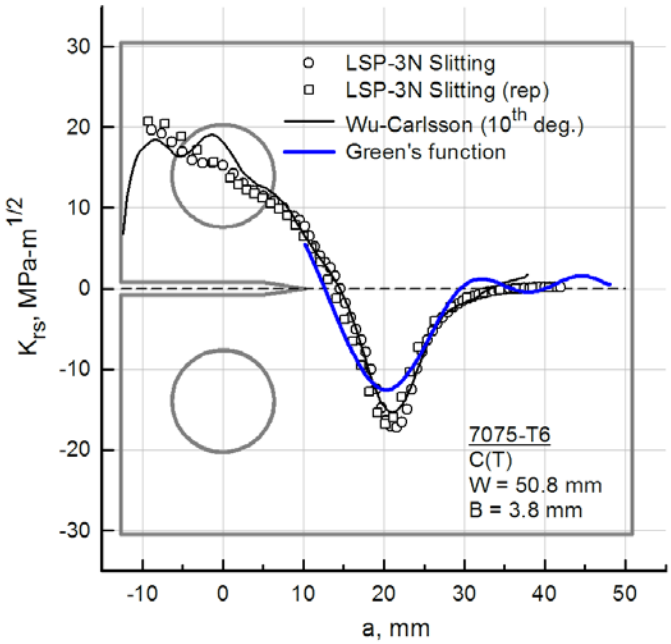

Figure 20. Measured and Calculated Residual SIFs for Laser Shock-Peened C(T) Specimens

The maximum and minimum SIFs, as influenced by the residual SIFs, were calculated for the C(T) specimen using the K_{rs} values determined from the two tests and the two analyses. The results for the first test show the K'_{max}, K'_{min}, K_{rs}, and K_{op} values as a function of normalized crack length (see figure 21). Note that the ΔK_{eff}, as shown, is the difference between K'_{max} and K_{op}. The results from the second test and the two analyses have similar distributions, but somewhat different minimum K_{rs} values around a crack length of about 20 mm (or a/W ~ 0.4). The minimum ΔK_{eff} was about 2.54 MPa√m in this test, which was significantly above the $(\Delta K_{eff})_{th}$ for the 7075-T6 aluminum alloy material.

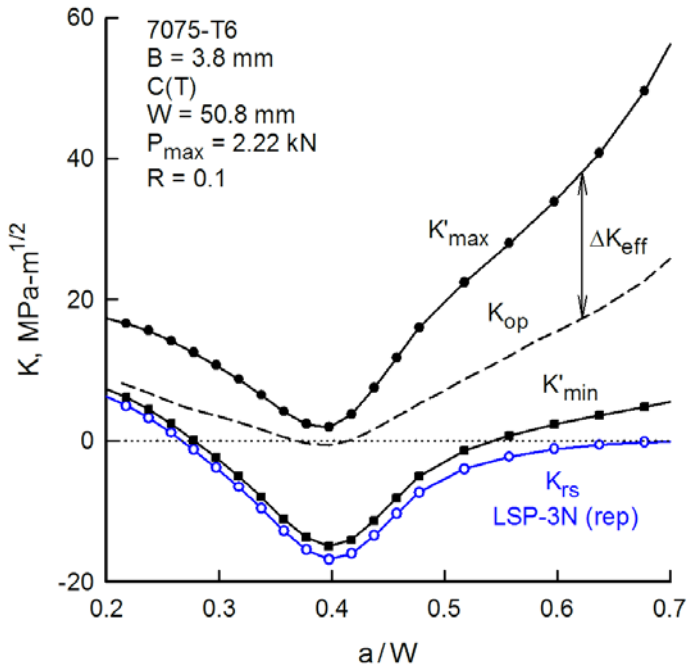

Figure 21. Measured Residual SIFs for Laser Shock-Peened C(T) Specimens and Calculated Maximum and Minimum SIFs

The *KRS.for* code was used to make fatigue crack growth predictions using the K'_{max} and K'_{min} distributions as a function of the normalized crack length; figure 22 shows these results. The symbols show the test results on one specimen and the curves show the predicted crack length-against-cycles using the experimental and numerical results. The single test produced a total life of approximately 400,000 cycles. The two measured K_{rs} results produced too much delay at the minimum ΔK_{eff} and greatly overpredicted the life. Test #1 was predicted to fail at about 880,000 cycles; test #2 was predicted to fail at 1.2 x 10^6 cycles. In contrast, the two numerical results produced much shorter lives than the test. These results show how sensitive the crack growth lives are to the particular minimum effective SIF range results from either the tests or the analyses. The predicted results from the weight function method would have been better with a slightly lower minimum K_{rs} value, such as 3.2 MPa√m instead of 3.6 MPa√m.

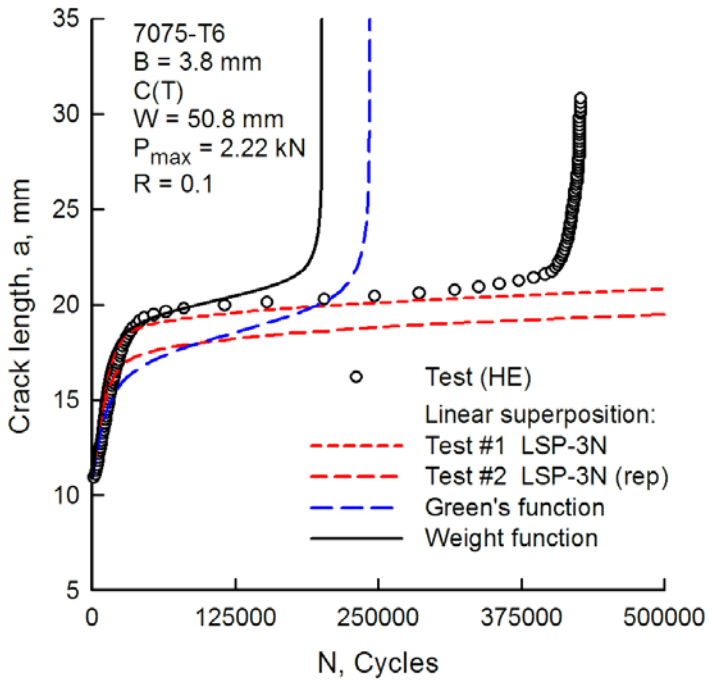

Figure 22. Measured and Calculated Crack Length-Against-Cycles for Laser Shock-Peened C(T) Specimen Using Linear Superposition Code

4.1.3 COLD-WORKED OPEN HOLE SPECIMENS.

An FE code was used in a previous FAA-sponsored research program [62] to analyze a cold-worked hole in the test specimen shown in figure 23 (without a notch or crack). The specimen width (*w*) was 21.6 mm and the specimen was friction-gripped with an *h*/*w* ratio of about 2. The initial radius (*r*) was approximately 3 mm. A mandrel with diametrical interference of 0.268 mm, corresponding to 4.5% CX, was pulled through the hole to induce the compressive residual-stress field. In the final specimens, the hole was reamed to a radius of 4.37 mm to relieve some of the residual stresses around the hole. The details of the test specimen and FEAs are given in references 62 and 63.

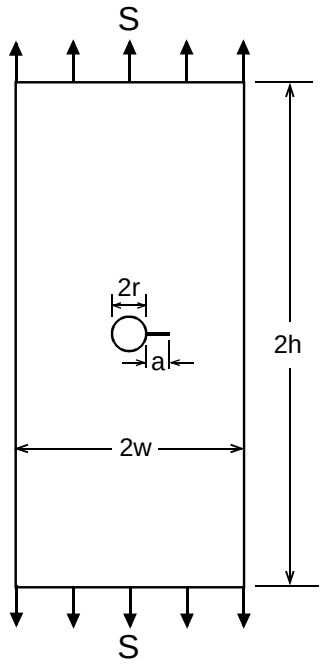

Figure 23. Single Crack Emanating From an Open Hole Subjected to Remote Uniform Stress

The FEA was also used to simulate the process of reaming and notching the hole in the cold-worked specimen. Figure 24 shows the normalized residual stress—as a function of the distance from the hole—after cold-working, reaming, and notching. The solid triangular symbols [63] show the final residual stress distribution predicted to be present in the test specimen.

In the current FAA-sponsored project, another FEA was performed using a much more refined model than in the previous study. Ismonov's results are shown as the open symbols in figure 24, which produced a larger magnitude of residual stresses remaining in the cold-worked, reamed, and notched specimens than the results shown in reference 62.

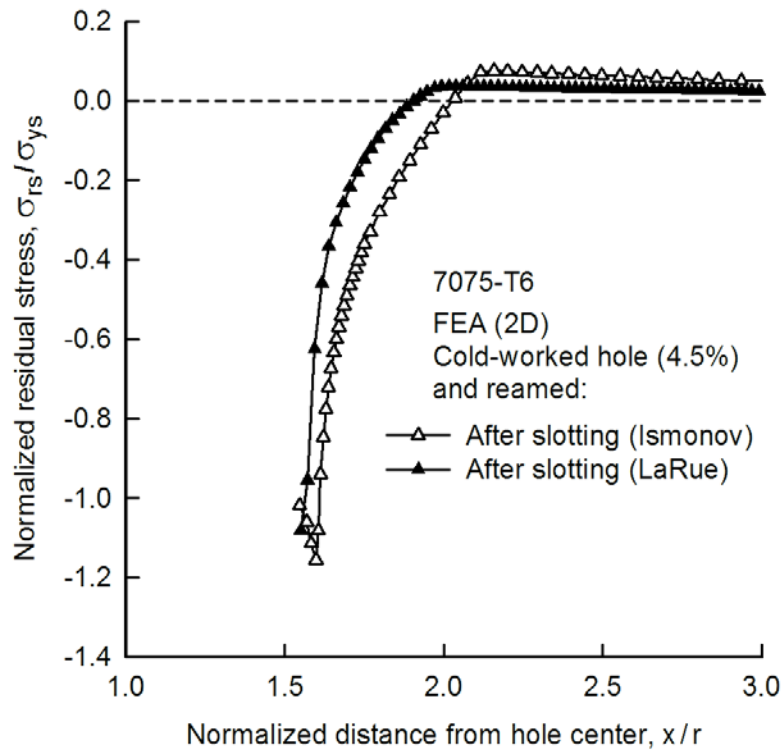

Figure 24. Normalized Residual Stresses After Reaming and Notching Cold-Worked Hole From Two Different FEAs

The linear superposition code, *KRS.for*, was used to analyze fatigue crack growth under the two different residual stress distributions shown in figure 24. Figure 25 shows the residual SIFs using Ismonov's results, the edge of the hole with the electrical discharge machining (EDM) slot, and the various SIFs as a function of crack length-to-hole radius (a/r). The lower dashed curve represents the residual SIFs and the upper dashed curve represents the $K_{\max}$ values. The upper and lower solid curves represent the $K_{\max} + K_{rs}$ and $K_{\min} + K_{rs}$ curves, respectively. The calculated K_{op} values from the *KRS.for* code fall between the two solid curves, and the difference between the upper solid curve ($K_{\max} + K_{rs}$) and the K_{op} curve is the effective SIF range (ΔK_{eff}).

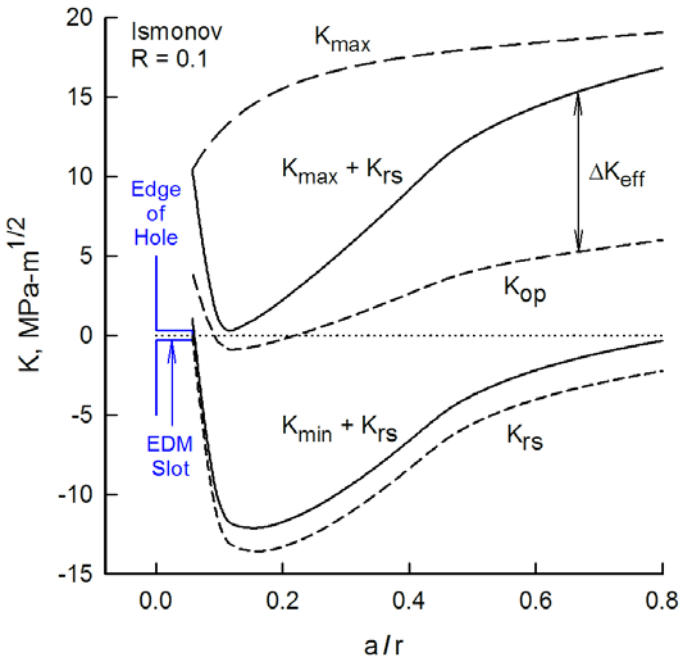

Figure 25. Various SIFs for Notched Cold-Worked Hole as a Function of Crack Length-to-Hole Radius (*a*/*r*) Ratio

Figure 26 shows the measured and predicted crack length-against-cycles for the cold-worked, reamed, and slotted open hole specimens using linear superposition code. As a reference, the constant-amplitude loading calculations with no residual stress are represented as the small dashed curve. Making crack growth life calculations using the residual stress results from LaRue [63] fell an order-of-magnitude short of the test data, while the residual stress distribution from Ismonov's analyses predicted a slightly longer life than the tests. Lower residual stresses from Ismonov's analyses caused the ΔK_{eff} values to be closer to threshold conditions and produced a much longer crack growth life than the results from LaRue's analyses.

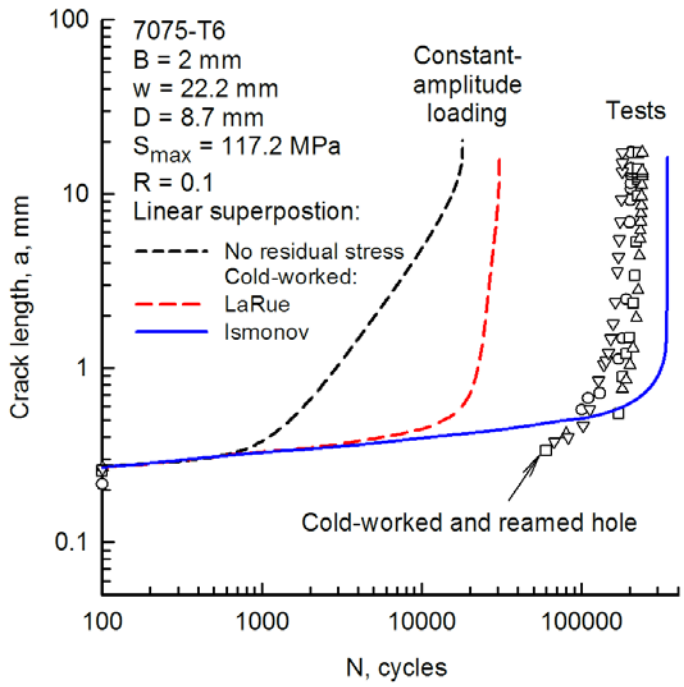

Figure 26. Measured and Predicted Crack Length-Against-Cycles for Cold-Worked, Reamed, and Slotted Open Hole Specimen Using Linear Superposition Code

4.2 NONLINEAR METHOD.

During the past two decades, the FASTRAN life prediction code has been successfully used to predict the fatigue crack growth lives for a wide variety of materials under a wide range of load histories (constant-amplitude and spectrum loading) [64-69]. Using the baseline fatigue crack growth rate data for the material of interest over a wide range of stress ratios and with rates from threshold to near fracture, the code has been able to predict the fatigue crack growth rate behavior under a variety of load histories. The FASTRAN model is based on plasticity-induced deformations around a crack front and the crack closure concept [54 and 55].

Residual stresses are induced by various forms of plastic deformation, such as cold working and LSP. Thus, it would be a natural extension of the crack closure model to simulate the residual stresses through plastic deformation. The model would change the residual stress distribution through applied loading and crack growth. Current methods, such as linear superposition, which are used to account for the influence of residual stresses on crack growth, do not account for any decay in the residual stress field with crack growth [70].

Simulating cold-worked and reamed holes in FASTRAN requires significant modification [71]. The cold working process plastically overloads the material around the hole by inserting a mandrel of slightly larger diameter than the original hole diameter (*r*). The plastically deformed material (or yield zone) forms concentrically around the hole, as shown in figure 27(a). Once the mandrel is removed, a compressive residual stress develops at the edge of the hole because of the elastic material surrounding the hole. In the current study, overloads of specific magnitudes are applied to the FASTRAN model to generate a plastic zone region and compressive residual

stresses that simulate those produced during the cold working process, as shown in figure 27(b). In the previously discussed case of an overload, the modified strip-yield [71] model does not produce the type of yielding that is produced during the cold working process. Whether the simple model can be used with remote overloads to simulate the compressive residual stresses produced during cold working will be studied. A similar model could be developed, which would pressurize the hole in the same way that cold working would. This model may produce a different residual plastic deformation region, but this would require further study if the overload method was unsatisfactory. This approach requires a calibration between either FEAs [62] or some of the closed-form equations that have been developed for cold working [72 and 73]. Comparisons will be made between the residual stresses calculated from both the FEM [63] and the crack closure model.

In addition, the cold-worked hole was reamed to a radius of r_m. The reaming of the hole removed a large amount of the plastically deformed material at the edge of the hole and greatly reduced the extent of the compressive residual stresses. After reaming the hole, an EDM notch was machined into one side of the hole of length a_i, as shown in figure 27(c). The EDM notch, again, removed some plastically deformed material at the edge of the hole. The simulation in FASTRAN is shown in figure 27(d).

An FE code was used to analyze a cold-worked hole in the test specimen shown in figure 23 (without a notch or crack). The specimen width (w) was 21.6 mm and the specimen was friction-gripped with an h/w ratio of approximately 2. The initial radius (r) was about 3 mm. A mandrel with diametrical interference of 0.268 mm, corresponding to 4.5% CX, was pulled through the hole to induce the compressive residual stress field. In the final specimens, the hole was reamed to a radius of 4.37 mm to relieve some of the residual stresses around the hole. The details of the analysis are provided by Daniewicz and Newman [62].

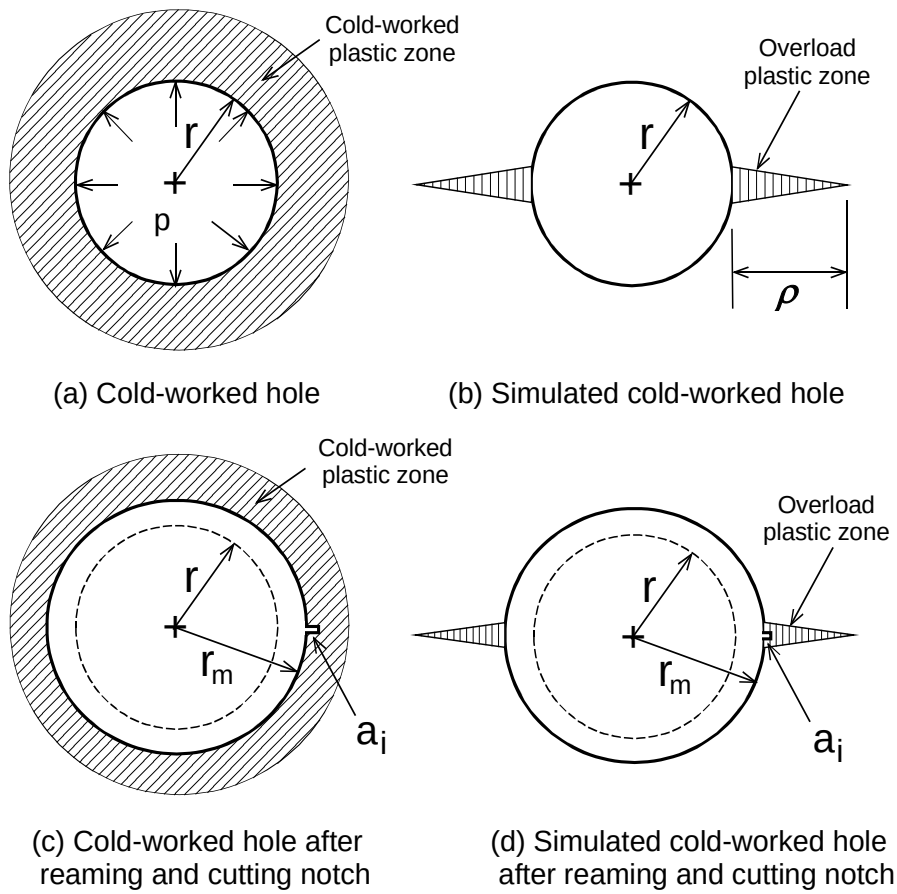

Figure 27. Cold-Worked Hole and Simulated Behavior in FASTRAN

The normalized residual stress (σ_{rs}/σ_{ys}), as a function of the distance from the hole (x/r), is shown in figure 28 as open symbols. The tensile yield zone had extended to about twice the hole radius, and the reverse plastic zone was about 20% of the hole radius. Various tensile overloads (S_{OL}) were applied to the crack-closure model and the resulting residual stress distributions are shown as curves. The end of each curve shows the extent of the tensile plastic zone. The 350 MPa overload matched the tensile plastic zone, but did not produce enough compressive residual stresses in the plastic zone. The solid curve at 420 MPa tended to match the reverse plastic zone size and approximated the residual-stress distribution on the average. The 420 MPa overload will be used to simulate the cold-worked hole.

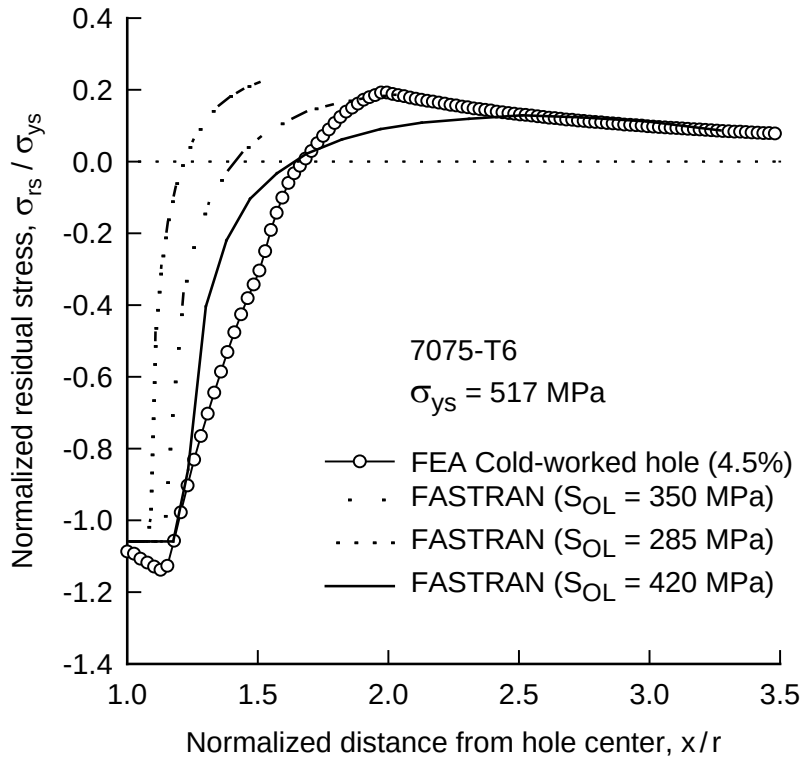

Figure 28. Normalized Residual Stresses for Cold-Worked Hole From FEA and Simulated Behavior in FASTRAN

The FEA was also used to simulate the process of reaming and notching the hole in the cold-worked specimen. The normalized residual stress, as a function of the distance from the hole, is shown as open symbols in figure 29. The circular symbols show the final residual stress distribution predicted to be present in the test specimens. Again, the curves show the results of the reaming and notching simulations in FASTRAN. The solid curve (420 MPa) tended to match the residual stress distribution fairly well. Figure 30 shows the residual plastic deformations in the crack closure model after the overload (solid symbols) and reaming the hole (open symbols) as a function of the distance to the tip of the tensile plastic zone (x/d_{max}). The reaming process greatly reduced the amount of plastic deformation from the cold-worked hole.

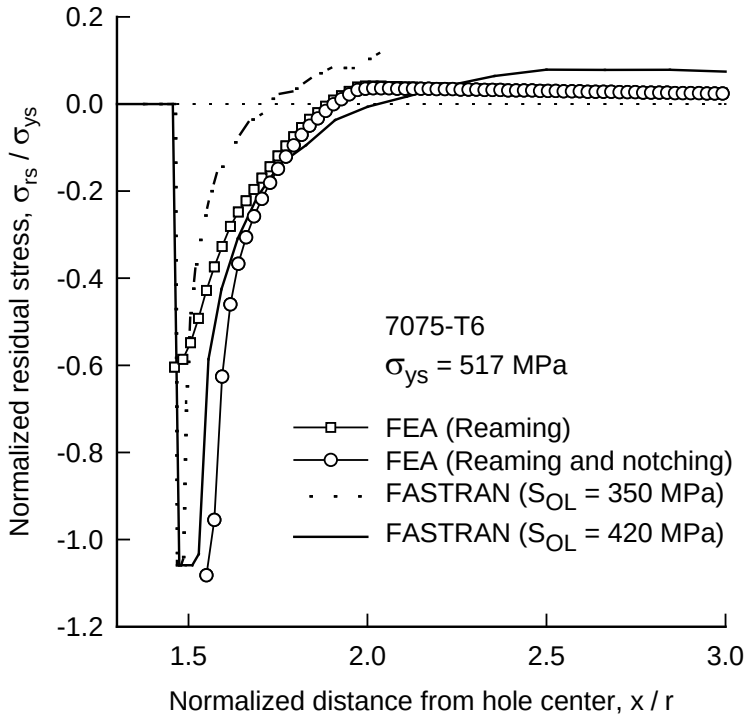

Figure 29. Normalized Residual Stresses After Reaming and Notching Cold-Worked Hole From FEA and Simulated Behavior in FASTRAN

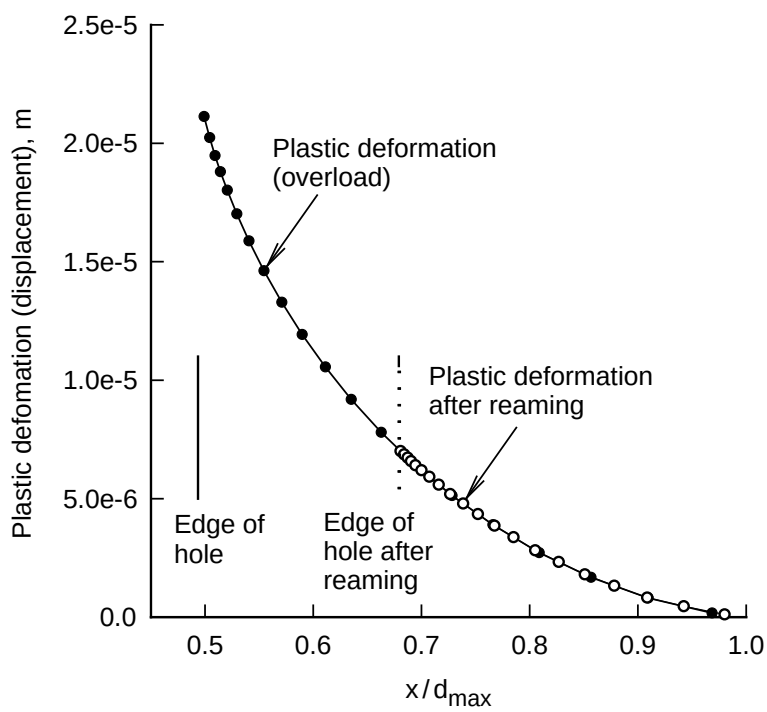

Figure 30. Residual Plastic Deformations in FASTRAN During Simulated Cold Working and After Reaming

4.2.1 THE MSU TESTS.

Rectangular specimens with central holes were tested with and without cold working of the holes. The specimens were approximately 44-mm wide, with plastic shims bonded to the front and back of each grip end to prevent grip-end cracking. Because of the shortened height of these specimens between grip lines, it was found that remote uniform displacement was a more appropriate BC than uniform stress [71]. The tests conducted by LaRue [63], using cold-worked specimens obtained from the SAC, were analyzed with the improved FASTRAN code for two loading conditions: (1) crack growth predictions were made under constant-amplitude loading on single crack-at-an-open-hole specimens, and (2) the cold-worked, reamed, and notched specimens were analyzed. Comparisons were made between all of the tests and the predicted results from FASTRAN.

4.2.1.1 NON-COLD-WORKED HOLE SPECIMENS.

Figure 31 shows all of the constant-amplitude tests conducted at a stress level of 117.2 MPa. An initial notch, 0.25 mm in length, was machined in each specimen on one side of the hole. Two predictions were made with FASTRAN. First, predictions were made for the uniform-applied stress case (dashed curve). These results indicated that something was causing the predicted results to produce much higher crack growth rates than the tests for crack lengths greater than approximately 6 mm; therefore, at this point, the remote BCs on the test specimen were questioned. It was known that remote displacement BCs for an unsymmetrical crack configuration would cause a load transfer to the stiffer ligament that would lower the SIFs for the cracked ligament. Thus, the FADD2D code [74] was used to generate the SIF solution for the remote uniform displacement case [71], resulting in the solid curve in figure 31. The predicted results were in better agreement with the test data, but still fell short for the large crack lengths. It was suspected that there may be something else in the specimen gripping or load train that would further reduce the SIFs for large cracks.

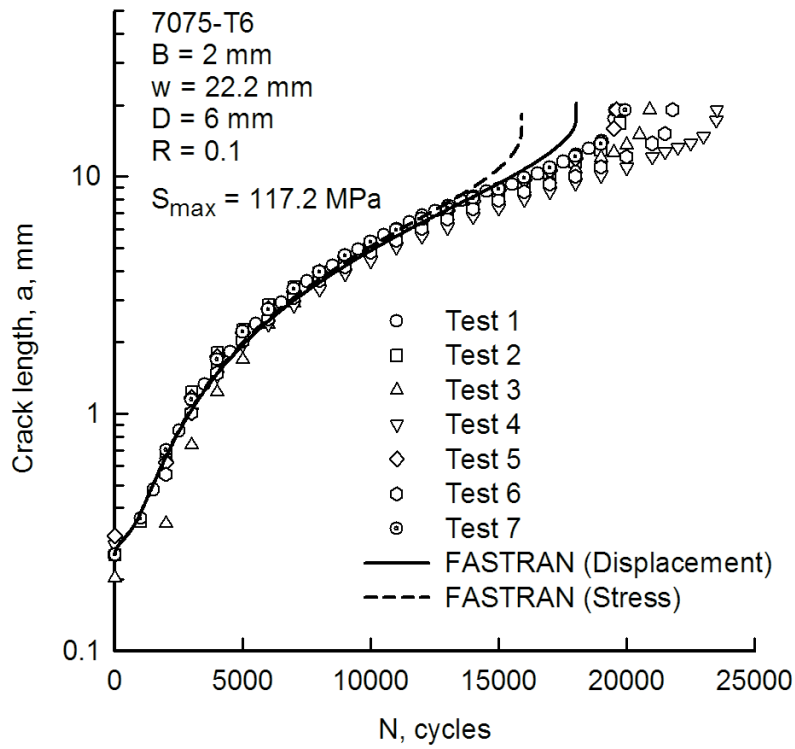

Figure 31. Measured and Predicted Crack Length-Against-Cycles Under Constant-Amplitude Loading for Several Single Crack-at-an-Open Hole Specimens Made of 7075-T6 Aluminum Alloy

4.2.1.2 COLD-WORKED HOLE SPECIMENS.

The cold-worked specimens had an initial hole diameter (*D*) of about 6 mm. A mandrel with diametrical interference of 0.268 mm, corresponding to 4.5% CX, was pulled through the hole to induce the compressive residual stress field. In the final specimens, the hole was reamed to a diameter of 8.7 mm to relieve some of the residual stresses around the hole. The cold-worked and reamed holes were then notched with a 0.25 mm length cut on one side of the hole and the specimens were subjected to a constant-amplitude loading (S_{max} = 117.2 MPa; R = 0.1). The symbols shown in figure 32 represent the results of the four tests. The initial crack length for each specimen is shown at 100 cycles. The cycles required to initiate a crack at the notch, which is estimated to be fewer than a few thousand cycles, is included in the crack length against-cycles data. The dashed curve shows the predicted results for only constant-amplitude loading (no cold working), but using the larger hole radius and same initial notch size. The solid curve shows the predicted results from FASTRAN, which was about 45% short of the average of the four tests. Considering that the residual stresses in the FASTRAN model (figures 28 and 29) were less than those from the FEAs, the comparison was reasonable. The modified FASTRAN predicted the nearly order-of-magnitude enhancement in life due to cold working. Further study is needed to improve the residual stresses caused by cold working.

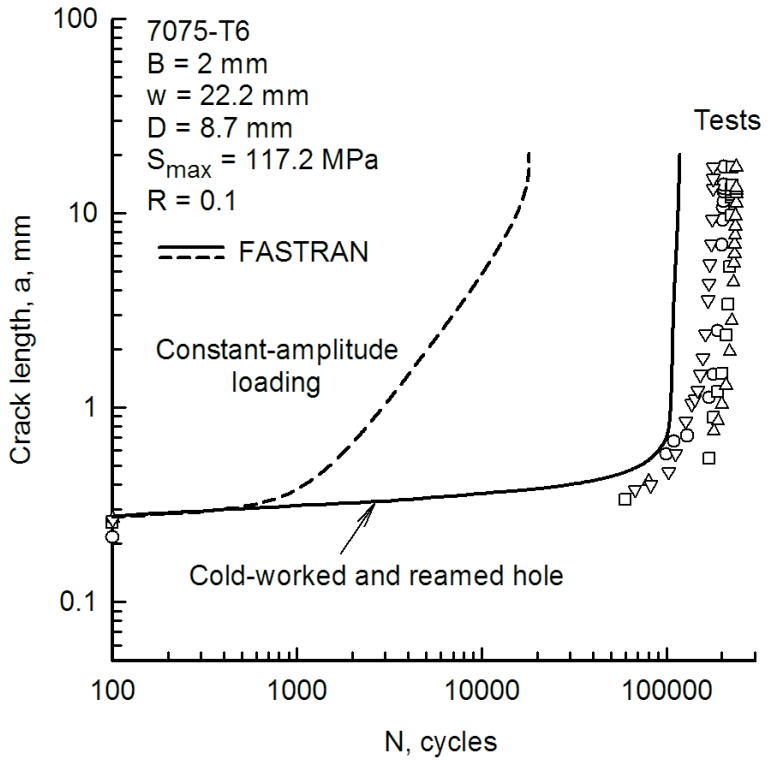

Figure 32. Measured and Predicted Crack Length-Against-Cycles Under Constant-Amplitude Loading After Cold Working, Reaming, and Notching

The enhancement from the crack closure model was due to the higher crack opening stress levels generated in the cold-worked and reamed specimens. Figures 33 and 34 show the crack opening stress ratio as a function of either crack length or cycles, respectively. The dashed curve shows the calculated crack opening stress ratio under constant-amplitude loading (no cold working). The rise in the crack opening stress ratio near the initial crack length was caused by the lower constraint due to the hole. The crack opening stress ratio reached a level that was nearly constant for most of the fatigue life. The rapid drop in the crack opening stress ratio near the end of life was due to the crack rapidly growing to failure (the yield zone became large compared to the uncracked ligament). However, the cold-worked and reamed hole simulation exhibited a much larger rise in the crack opening stress ratio, reaching a value of 87% of the maximum applied stress. As shown in figure 34, most of the fatigue life was consumed while the crack opening stress ratio was at a high level.

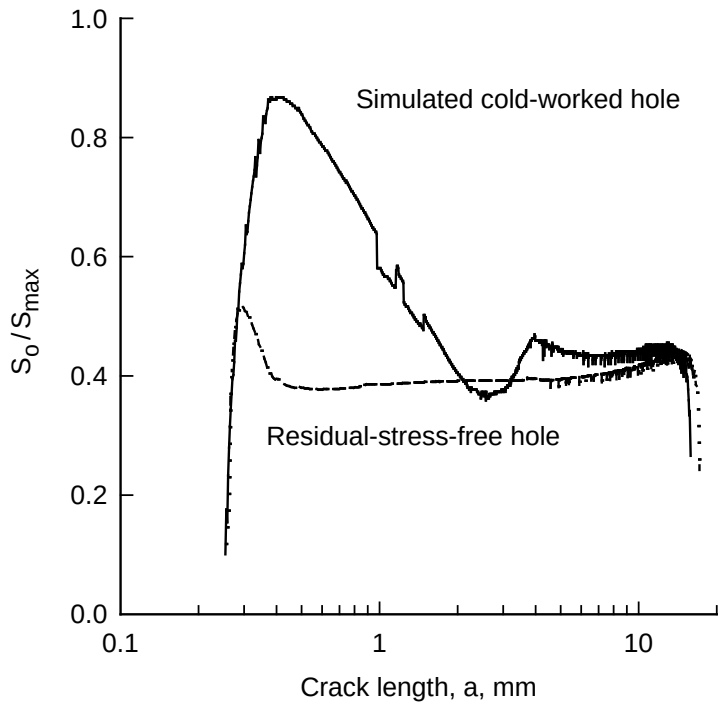

Figure 33. Calculated Crack Opening Stress Levels as a Function of Crack Length During Constant-Amplitude Loading for a Residual Stress-Free Hole and a Simulated Cold-Worked Hole

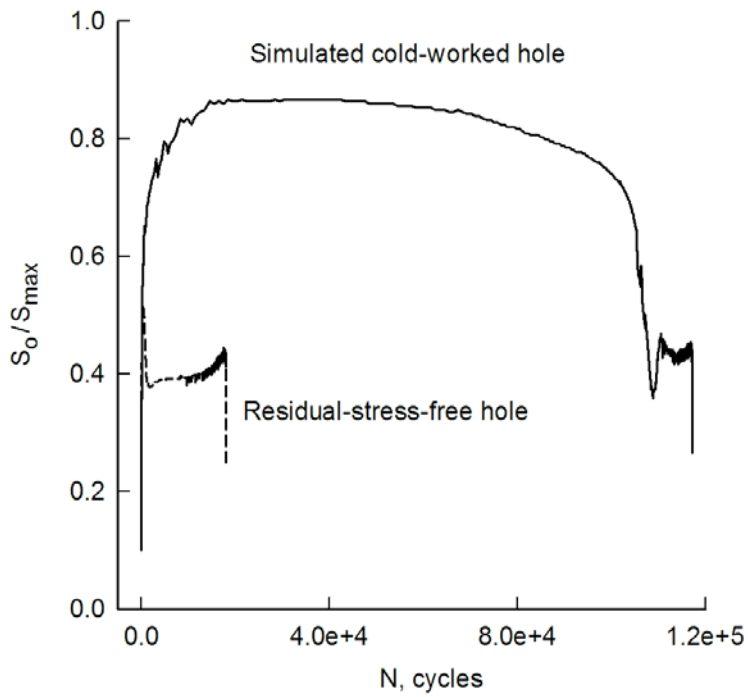

Figure 34. Calculated Crack-Opening Stress Levels as a Function of Cycles During Constant-Amplitude Loading for a Residual Stress-Free Hole and a Simulated Cold-Worked Hole

4.2.2 THE HE TESTS.

Long, dog bone-shaped open hole specimens were cut from 2.0-mm-thick 7075-T6 aluminum alloy sheets, with the long axis of the specimens along the rolling (*L*) direction. Equal numbers of specimens were cut from clad and bare sheets with specimen designations, including C for those cut from clad sheet and B for those cut from bare sheet. The 2.0-mm-sheet thickness is thin enough to ensure that crack lengths are approximately constant through the specimen thickness (1D cracks). A dog bone shape was chosen over a constant-width specimen to avoid problems of failure at the grips due to fretting fatigue, as occurred for earlier tests of straight specimens [62]. The specimens were 380 mm in total length and 89 mm in width at the grip ends. The gripped ends tapered to a central gage section 44.5-mm wide and 89-mm long with a centrally located hole. The central gage section was longer than 1.2 multiplied by the gage width, as required for M(T) specimens, and specimens in ASTM E647 [56] to avoid specimen-specific influence from the grip BCs. The split sleeve CX process was used to induce residual stress at the hole in half of the specimens. Hole size and degree of cold working were selected to be typical of rotorcraft applications. Prior to CX, holes were drilled to 6.35 mm diameter. The CX sleeve was oriented so that the split was parallel to the long axis of the specimen and was sized to obtain a 3% interference fit with the tapered mandrel. After CX, the holes were reamed to 7.1 mm in diameter to remove any undesirable features left by the CX process. The as-machined specimens had holes drilled and then reamed using the same tooling employed on CX specimens, so that their final diameter was also 7.1 mm.

The tests conducted by HE, using specimens obtained from SAC, were analyzed with the improved FASTRAN code for two loading conditions: (1) crack growth predictions were made under constant-amplitude loading on single crack-at-an-open hole specimens at R = 0.1 and 0.5 cyclic loading without cold working of the holes, and (2) the cold-worked, reamed, and notched specimens were analyzed for crack growth under constant-amplitude loading at R = 0.1 and 0.5, respectively. Comparisons were made between these tests and the calculated results from FASTRAN. In addition, predictions made by HE using linear superposition with and without cold working of the holes.

4.2.2.1 NON-COLD-WORKED HOLE SPECIMENS.

Figure 35 shows the measured and predicted crack length-against-cycles results on test specimens conducted at a remote applied stress level of 65 MPa at R = 0.5. The symbols show the tests and the curves show the predictions. The results are presented on a log-log plot so that the results in the early stages of crack growth could be amplified. The test specimens had an initial crack length of about 0.4 mm in length from one side of the central hole. The predicted results using FASTRAN produced faster crack growth in the early stages, but agreed well for larger crack lengths, whereas the predictions made by HE agreed well with the test data.

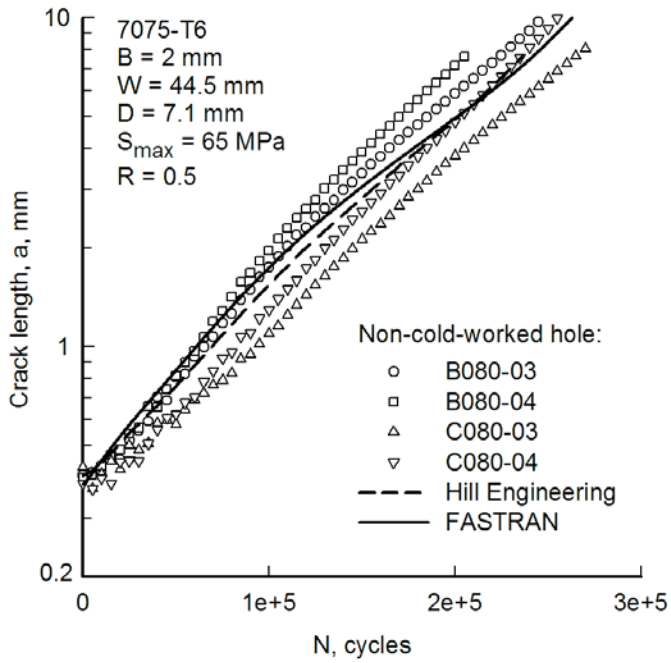

Figure 35. Measured and Predicted Crack Length-Against-Cycles Under Constant-Amplitude Loading for Single Crack-at-an-Open Hole Specimens Made of 7075-T6 Aluminum Alloy at R = 0.5

Figure 36 shows the test and analysis results at R = 0.1 loading. Again, the symbols show the tests and the curves show the predictions. The test specimens had an initial crack length of about 0.4 mm in length from one side of the central hole. The predicted results using FASTRAN agreed in the early stages of crack growth, but fell to the higher side of the test data for large cracks, whereas the predictions made by HE again agreed well with the test data. The reason for the larger discrepancy between the tests and FASTRAN for larger crack lengths was not known. These results are in contrast to those shown in figure 31 for similar open-hole specimens that showed very good agreement.

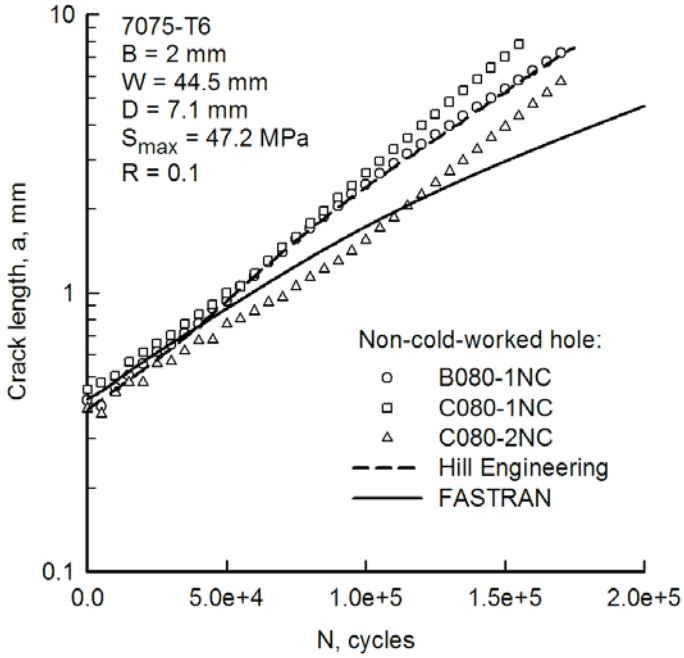

Figure 36. Measured and Predicted Crack Length-Against-Cycles Under Constant-Amplitude Loading for Single Crack-at-an-Open Hole Specimens Made of 7075-T6 Aluminum Alloy at R = 0.1

In an effort to find the reason for the discrepancy for the R = 0.1 data, a comparison of measured and predicted crack growth rates for the two sets of tests are shown in figure 37. The open symbols show additional test data obtained from the NASGRO database for thicknesses of 1 and 2 mm for R = 0.02 loading and data from NASA RP-1309 on 2.3 mm thick material at R = 0. The solid circular symbols show the test data from the HE tests at R = 0.1 and 0.5. The HE (B = 2 mm) and NASGRO (B = 1 mm) test data at low R did not overlap, but agreed well at a rate of 10^{-7} m/cycle, which is at a transition in slopes on the ΔK-rate plot.

In figure 37(a and b), the solid lines show the ΔK_{eff}-rate curve for the 7075-T6 aluminum alloy, and the dashed lines show predictions made for various R values at R = 0.1 and 0.5, respectively. Test data from the NASA and the NASGRO databases are shown for comparison. All of the measured test data from HE fell in the transitional region (10^{-8} to 10^{-7} m/cycle) on the ΔK-rate plots. The R = 0.1 test results from HE fell to the high side of the FASTRAN-predicted results (dashed line at R = 0.1). This is suspected to be the reason for the longer life prediction made with FASTRAN for the R = 0.1 loading condition. The R = 0.5 test results from HE agreed fairly well in the early and late stages of crack growth.

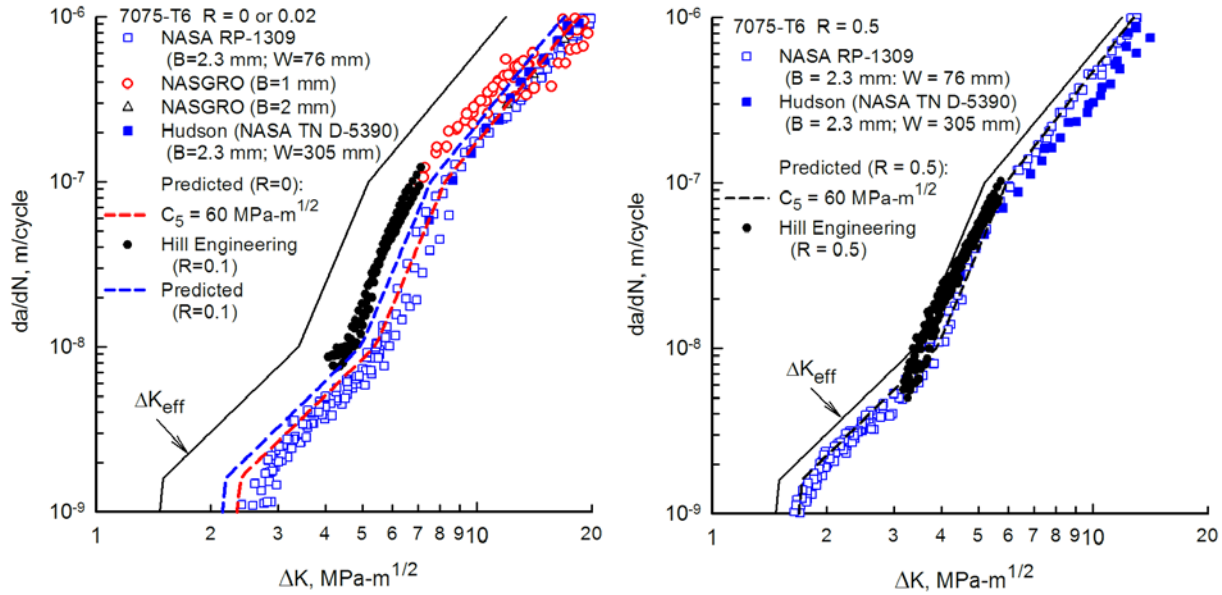

(a) (b)

Figure 37. Measured and Predicted Crack Growth Rates for the 7075-T6 Aluminum Alloy at (a) R = 0.1 and for (b) the 7075-T6 Aluminum Alloy at R = 0.5

4.2.2.2 COLD-WORKED HOLE SPECIMENS.

The cold-worked and reamed holes were notched with a 0.4-mm-length cut on one side of the hole and the specimens were subjected to constant-amplitude loading with either R = 0.1 or 0.5. These test results and calculations are shown in figures 38 and 39 for R = 0.1 and 0.5 loading, respectively. The large dash curve shows the predicted results for only constant-amplitude loading (no cold working), but using the larger hole radius and same initial notch size. The solid curve shows the predicted results from FASTRAN for two overload stress values chosen to account for the cold work compressive residual stresses. The larger overload value (S_{OL} = 410 MPa) results fell close to one of the test results at R = 0.1, but generally fell short of the test data. Whereas, the two overload values tended to bound the test results for R = 0.5.

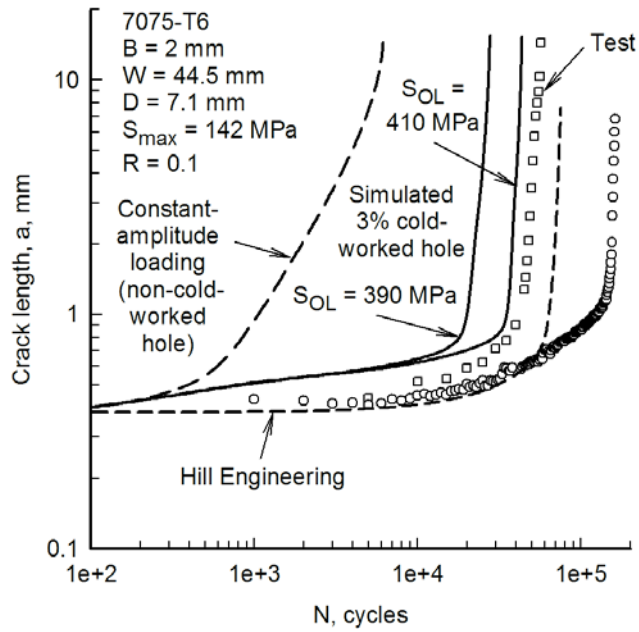

Figure 38. Measured and Calculated Crack Length-Against-Cycles Under Constant-Amplitude Loading After Cold Working, Reaming, and Notching for R = 0.1

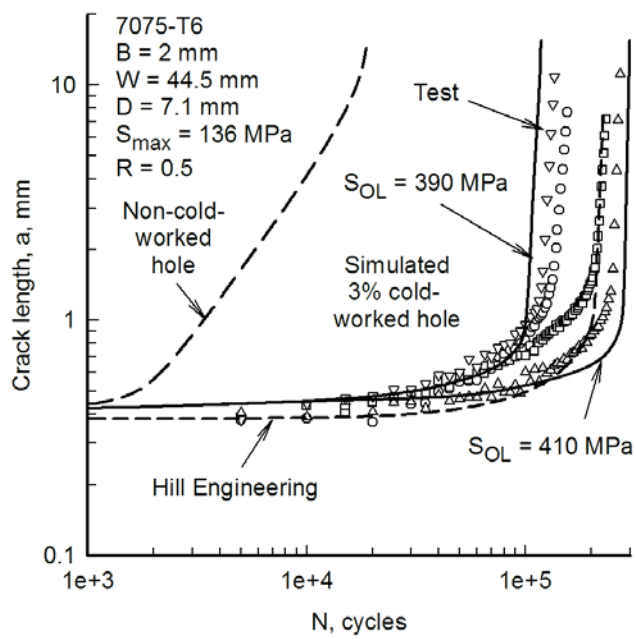

Figure 39. Measured and Calculated Crack Length-Against-Cycles Under Constant-Amplitude Loading After Cold Working, Reaming, and Notching for R = 0.5

5. THE 3D ANALYSES OF THE COLD WORKING PROCESS.

5.1 INTRODUCTION.

Pin or fastener joints are widely used in the aircraft and rotorcraft industries. These joints are also known to be susceptible to fatigue failure due to the localized stress concentrations caused by the presence of the holes. To overcome this problem, a split sleeve CX process [75] became a life enhancement method to mitigate the effect of the stress concentrations by creating a compressive circumferential residual stress field around the hole. In this process, the hole is radially expanded using a tapered mandrel and a split sleeve (figure 40). The diameter of the mandrel with the sleeve is greater than that of the hole. When the mandrel is prefitted in the internally lubricated sleeve and pulled through the hole, the hole is plastically expanded. As the mandrel is removed, the hole undergoes a partial, but not full, elastic recovery, creating the desired compressive circumferential residual stresses. In the final stage of the process, the hole is reamed to the required size.

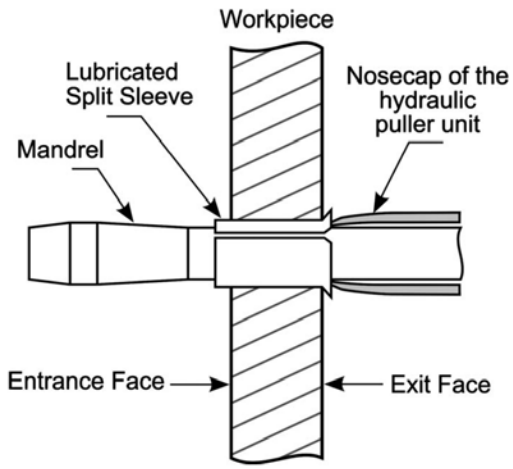

Figure 40. Split Sleeve CX Process Description

Many analytical and numerical studies have been conducted and published regarding the prediction of the residual stresses created by CX. Rich and Impellizzeri [73] and Ball [76] developed 2D elastic-plastic, closed-form solutions for the uniform radial expansion of fastener holes assuming small displacement, plane strain [73], and plane stress [76] conditions. The 2D, 2D axisymmetric, and 3D numerical solutions were obtained using a simplified approach, in which the hole was uniformly expanded to simulate the interference between the mandrel and the hole [71, 72, and 77-79]. The assumption of a uniform expansion inherently limits the accuracy of the predicted residual stress.

Other studies have included the mandrel insertion explicitly to model the process in a more physically realistic way. This is because the hole surface is expanded sequentially (rather than uniformly) in the actual process, starting from the mandrel entrance side toward the exit side of the hole (figure 40), resulting in a variation of the residual stress magnitudes through the plate thickness. Garcia-Grenada [80] conducted a 2D axisymmetric analysis, whereas Papinkos [81] and Chakherlou [82 and 83] performed 3D simulations of cold hole expansion with the mandrel.

However, references 84 thorugh 86 did consider the sleeve in their analyses, but did not include the split in the sleeve, or consider the friction at the interface. The frictionless contact was justified by the assumption of lubricated surfaces. However, the sleeve is only internally lubricated in the actual process. This ensures that, if the hole surface is improperly cleaned after CX, the installed rivets will not slide in the hole and create non-desirable consequences [87]. Hence, the friction at the interface between the outer surface of the sleeve and the hole is not negligible in the cold-working process.

Karabin et al. adopted a slightly different approach to simulate the CX process and studied the influence of two different split geometries for the sleeve: conventional and overlap [88]. They did not explicitly model the mandrel insertion and achieved the hole expansion in a circular disc by applying a uniform radial displacement on the interior surface of the split sleeve. Karabin et al.'s study focused on the residual strains around the hole surface rather than the stress [88].

The current research builds on this previous work in an effort to conduct the most sophisticated and physically realistic simulations of the cold-working process. Rigorous 3D FEA of the CX and reaming processes are described, which include the tapered mandrel insertion, split sleeve, friction, and geometrical nonlinearities (i.e., large strain). As part of the verification process, the numerical results are compared with experimental measurements of residual stress. Next, the influence of various possible friction coefficients (μ) in the range of 0.1 to 0.2 is evaluated. The circumferential stress solutions from the split sleeve model are compared with those from the non-split sleeve model. The effect of different sheet BCs is discussed in section 5.2.

5.2 THE FEA ANALYSIS OF THE COLD WORKING PROCESS.

5.2.1 CONFIGURATION.

Figure 41 shows geometries of the specimen, the sleeve, and the mandrel. The cold working simulations are performed on an 88.90- by 44.45-mm ($h \times 2w$) rectangular sheet with a central hole of 6.07 mm in initial diameter ($2r_i$). In accordance with the experimental work, two different sheet thicknesses were considered. The thickness of the thin specimen is t_p = 2.03 mm, and the thickness of the specimen is t_p = 4.826 mm. The thickness and the length of the sleeve are t_s = 0.20 mm and l_s = 3.80 mm, respectively. The split in the sleeve (figure 41(b)) is aligned at the 12 o'clock position in accordance with the experimental work. It should be noted that the flared end of the sleeve is not included in the FE model to simplify the problem.

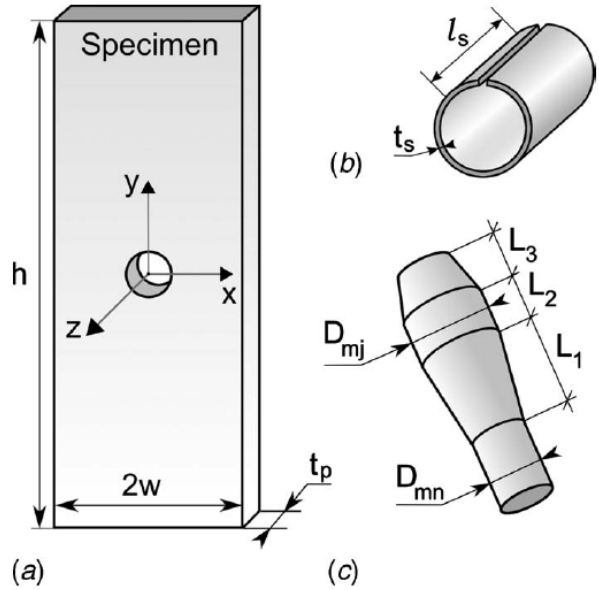

Figure 41. Geometries of the (a) Specimen, (b) Split Sleeve, and (c) Mandrel

The major and minor diameters of the mandrel (figure 41(c)) are: D_{mj} = 5.84 mm and D_{mn} = 5.46 mm, respectively. The lengths of the sections given in figure 32(c) are: L_1 = 6.35 mm, L_2 = 2.36 mm, and L_3 = 5.72 mm.

The amount of cold work is defined as the magnitude of the normalized radial expansion of the hole during the process and is given by:

$$\frac{D_{mj} + 2 \cdot t_s - 2 \cdot r_i}{2 \cdot r_i} \times 100\% \tag{17}$$

where D_{mj} is the mandrel major diameter, t_s is the sleeve thickness, and r_i is the initial hole radius. The cold work is assumed to equal 3% in this study. After the CX, the hole is reamed to a final size $2r$ = 7.07 mm. These dimensions are summarized in table 3.

Table 3. Cold Working Model Dimensions in Millimeters

Variables	Dimensions
h	88.90
$2w$	44.45
$2r_i$	6.07
t_p	2.03
t_s	0.20
l_s	3.80
D_{mj}	5.84
D_{mn}	5.46
L_1	6.35
L_2	2.36
L_3	5.72
$2r$	7.07

5.2.2 MATERIAL MODELS.

The sheet material is 7075-T6 aluminum alloy with the initial yield strength σ_{ys} = 483 MPa. Young's modulus is 72.5 GPa and Poisson's is 0.3. Figure 42 shows the stress-strain curve for the material that was used [89]. Using these data, two different work-hardening material models were considered in the numerical analysis: multilinear isotropic hardening and multilinear kinematic hardening. The kinematic hardening rule approximates the Bauschinger effect, whereas the isotropic hardening rule does not. The material of the split sleeve is stainless steel with a Young's modulus of 210 GPa and a Poisson's ratio of 0.3. For simplicity, the material of the sleeve is assumed to be purely elastic, whereas the mandrel is modeled as a rigid body.

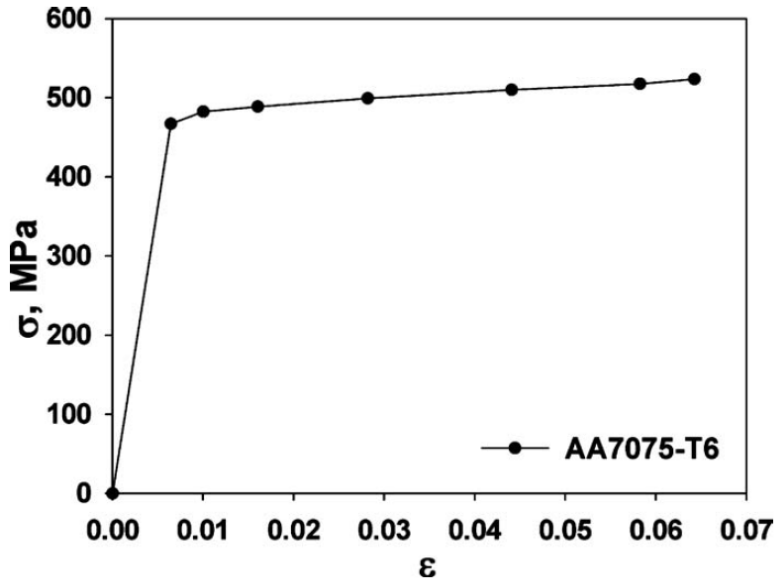

Figure 42. Elastic-Plastic Stress-Strain Curve of the 7075-T6 Aluminum Alloy Sheet

5.2.3 THE FE MODEL.

ANSYS 11.0 is used to carry out the numerical simulations. Using symmetry, only the right half of the sheet was modeled. This would not have been an option if the split in the sleeve was aligned differently than the 12 o'clock or 6 o'clock positions. The FE mesh used is shown in figure 43. The sheet and the sleeve, shown in light green and yellow, respectively, are meshed with 8-noded hexahedral structural solid elements (solid 185). Linear elements are preferred in this analysis over higher order elements, because higher order elements in ANSYS use only the corner integration points for the elastic-plastic analysis [90]. Thus, the linear elements generate solutions with the same accuracy as the higher order elements.

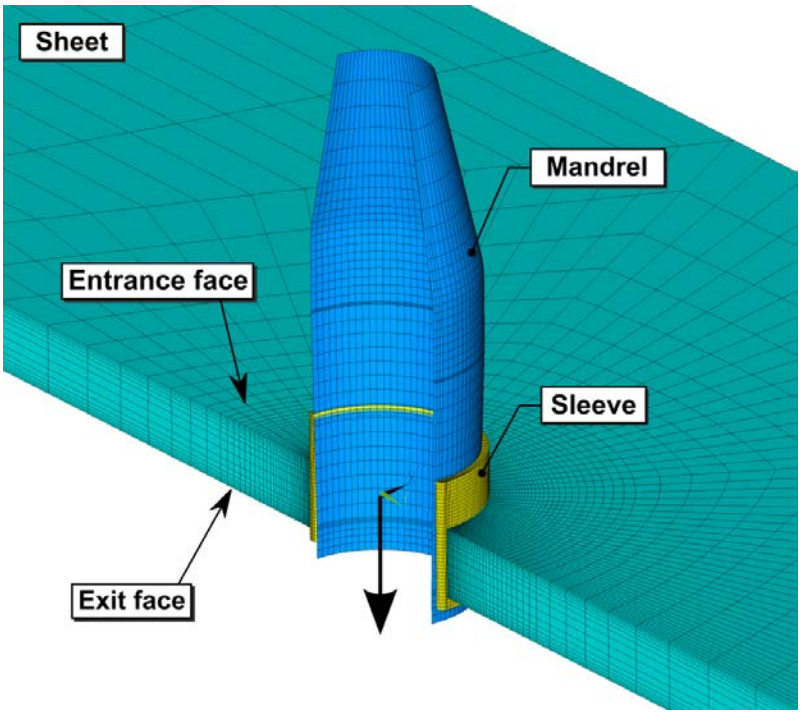

Figure 43. The FE Mesh of the CX Model

Appropriate 3D, four-noded surface-to-surface contact pair elements are used at the interfaces between the mandrel and the sleeve and between the sleeve and the hole, so that the pressure loads can be transferred from one face to another. The Coulomb friction model with friction coefficients in the range from 0.1 to 0.2 was considered between the sheet hole and the outer surface of the sleeve. Frictionless contact was assumed between the mandrel and inner surface of the sleeve. Because the sleeve is internally lubricated in the actual process, the friction coefficient will be negligible in this contact region. Moreover, preliminary results indicated that friction at the mandrel-sleeve interface had negligible influence on the final residual stress results.

As the tapered mandrel is pulled through the hole, the gap between the split edges of the sleeve starts to enlarge. As a result, a small portion of the hole wall corresponding to that particular region loses contact with the sleeve. To facilitate the gradual transition of the sleeve-hole contact from engaged to open status, the sharp split edge of the sleeve was smoothed with a surface fillet of appropriate radius in the FE model during the solution process (figure 44). Without this modification, the abrupt changes in contact status would create a numerical instability and result in a nonconvergent solution.

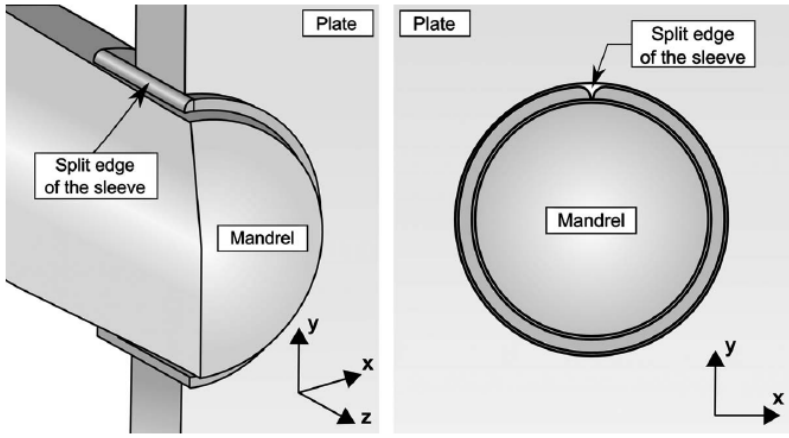

Figure 44. Configuration of the Smoothed Split Sleeve Edge

To model the mandrel as a rigid body, its surface is meshed with the rigid contact elements as shown in light blue in figure 43. Thus, no 3D solid elements are used for the mandrel, reducing the computational cost of the analysis.

5.2.4 BOUNDARY CONDITIONS AND COLD WORKING SIMULATION.

Figure 45 shows the prescribed BCs used in the numerical simulation. The symmetry constraints are shown as small rollers in the figure, whereas the constraints in the *z*-direction, which is the mandrel travel direction, are represented by triangular symbols. The constraint of the sleeve at the mandrel exit end corresponds to the contact with the nosecap of the puller unit shown in figure 40.

The following two BCs were considered in this work:

Case (a)—A single nodal constraint in the *z*-direction at the top corner of the sheet (figure 45(a)) is used to prevent the rigid body motion. This is the primary BC considered in this research because it corresponds to the BCs applied during the specimen preparation in which the operator lightly constrained its one edge as the hole was cold-expanded. The forces in the mandrel travel direction were completely reacted at the tool head.

Case (b)—All outer edges of the sheet are constrained in the mandrel movement direction. This may best represent the BCs of the in situ CX process of the sheet in the real structure. Although this BC was not used during the specimen preparation, it was still included to study the influence of the different plate constraints on the resulting residual stress solutions.

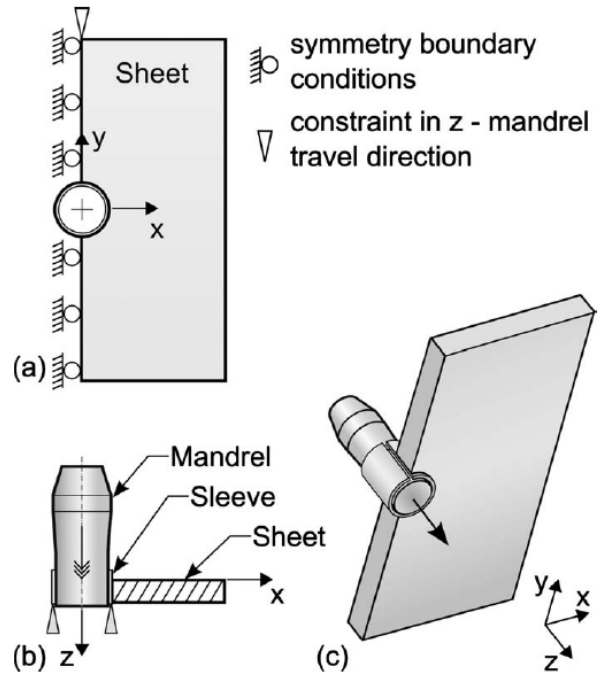

Figure 45. Prescribed BCs Used in the FE Model (case (a) is depicted here)

In the preliminary analysis with a zero or small friction at the interface between the sleeve outer surface and the hole, the plate partially slid out and lost contact with the sleeve at the hole exit side as the mandrel was pulled through the hole. As a result, the sheet with the constraints from cases (a) and (b) underwent excessive bending, leading to unreliable or even nonconvergent solutions. Therefore, the friction of μ = 0.1 or above had to be defined at the sleeve-hole interface to carry out physically realistic process simulations with the appropriate BCs.

Although CX is a dynamic process, it can be modeled in a quasistatic manner because the stress-strain response of the material is not significantly different at the strain rates of interest [78 and 87]. The mandrel insertion is simulated by applying incremental displacements to the mandrel in nearly 50 ramped load steps until it is completely pulled through the hole. Next, the reaming of the cold-expanded hole is simulated by deactivating a layer of elements on the hole surface using the EKILL command in ANSYS. Although the deactivated elements are not physically removed from the model, they contribute almost zero stiffness to the global stiffness matrix of the model [90].

It is suggested that the small deformation theory is applicable for total strain magnitudes up to 5% [82]. A typical CX process will produce strains exceeding 5% and, consequently, large strain effects were included in the FE model by activating the geometrical nonlinearities option during the solution process. Although the strain increments for each load step (or sub-step) were restricted to maintain accuracy, the large strain method has no theoretical upper limit on the total strain or rotation experienced by an element [90].

5.2.5 VALIDATION.

Two different procedures were used to verify the solution accuracy: a convergence study and a boundary inspection. In the first procedure, the FE mesh was repeatedly refined until the variation of residual stresses became negligible. Convergence studies were also performed with respect to the load steps because the number of load steps plays a crucial role in obtaining an accurate solution for a nonlinear analysis.

Although the exact solution of the problem in 3D is unknown, the traction-free BCs can be inspected around the expanded and reamed hole to ensure that the normal and shear stresses are approximately zero. It was found that the absolute values of maximum normal and shear stresses were approximately 2.0% and 3.0% of the material yield strength, which was assumed to be negligible. These values could be reduced by further refining the mesh around the hole, but it would increase computational cost while not significantly altering the final residual stress solution.

5.3 RESULTS.

The residual stress solutions from CX simulations will be given in the form of graphs, where the normalized circumferential residual stress ($\sigma_{\theta\theta}/\sigma_{ys}$, σ_{ys} = initial yield strength) is plotted as a function of the positions around the hole, such as the normalized distance from the hole center (x/r, r = reamed hole radius). The following results pertain to the reamed state of the hole.

5.3.1 THIN SPECIMEN.

5.3.1.1 NUMERICAL SOLUTION VS. EXPERIMENTAL MEASUREMENTS.

In figure 46, the FE solutions are compared with the experimental measurements at various through-thickness positions on the plane y = 0 [57, 91-93]. The dashed and solid curves represent the numerical solutions from the isotropic and kinematic hardening material models, respectively, with the case (a) BC. A friction coefficient of μ = 0.2 is used at the sleeve-hole interface in accordance with general practice in CX simulations [87]. The contour method measurements are given as symbols in the figure. It can be observed that the hoop residual stress distributions in the radial direction (x/r) from both the numerical solutions and the experimental data follow a similar trend, particularly at the through-thickness positions z/t_p = 0.25, 0.75 and in the mid-thickness of the sheet (figure 46(b-d)). At the sheet entrance and exit faces, the residual stress curves from the FEA exhibit sub-surface minimums, whereas the experimental data indicated minimum values at the hole surface (figure 46(a-e)). Also, the numerical solutions indicate that the residual stress magnitude is lowest at the sheet entrance face and highest near the mid-section (figure 46(f)). Differences in the solutions from the isotropic and kinematic hardening material models around the hole surface suggest that there was some reverse yielding in the region. Lower residual-stress magnitudes in the kinematic hardening material model resulted from the Bauschinger effect, in which the material starts yielding faster in reverse loading. This difference was also evident in the solutions before the reaming simulation was performed.

Through-thickness distributions of the residual stress data exhibit large scatter at x/r = 1, as shown in figure 46(f), making it difficult to compare with the numerical solutions. It can be observed, however, that the isotropic hardening material model solutions come out of the scatter band of the experimental data around the mid-thickness of the sheet, slightly overpredicting the residual stress magnitudes at the hole surface. Because the stress magnitudes using the kinematic hardening rule are in better agreement with the experimental measurements, this material model is used for all other computations, the results of which are given in figure 46.

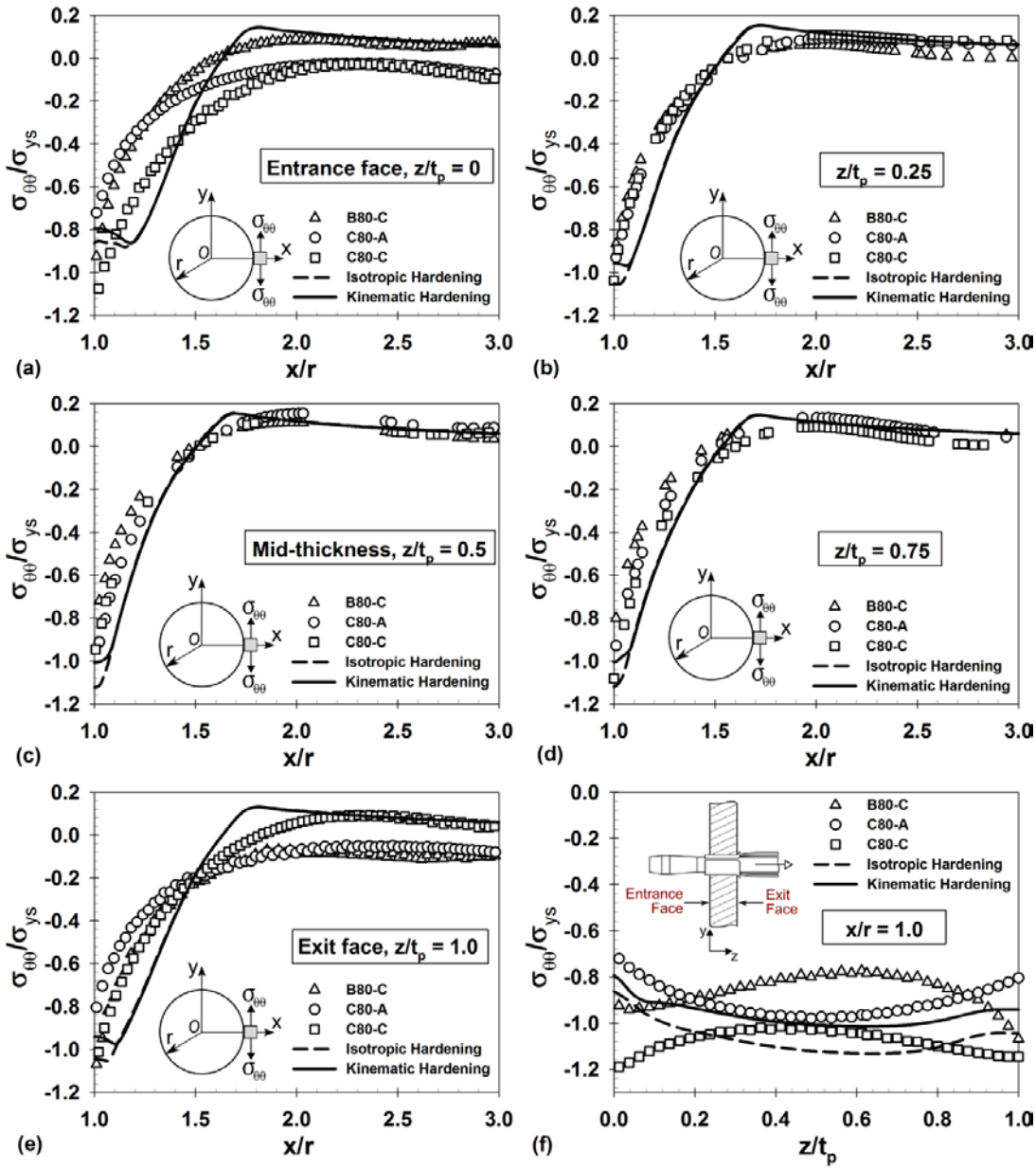

Figure 46. Normalized Circumferential Residual Stress Results From Isotropic and Kinematic Hardening Material Models Compared With Experimental Measurements for Thin Specimen (a) Entrance Face, (b) z/t_p = 0.25, (c) Mid-Thickness, (d) z/t_p = 0.75, (e) Exit Face, and (f) Through-Thickness Direction at x/r = 1 and y = 0

5.3.1.2 THE INFLUENCE OF FRICTION.

Figure 47 gives the residual stress results from the FE model with case (a) BC and with friction coefficients of 0.1, 0.15, and 0.2. The major influence of friction is observed in the area of the mandrel entrance face, where the higher friction coefficient produces hoop residual stresses with lower magnitudes (figure 47(a)). For example, the percentage difference of the residual stress at the hole edge at the entrance face between the friction coefficients of 0.1 and 0.2 is approximately 16%; however, in regions away from the entrance face, the influence of friction was much less significant, as shown in figure 47(b-d). The reason for the variations occurring at the entrance face only is not fully understood because of the complex nature of the process. Thus, this topic needs further investigation to reach any conclusions.

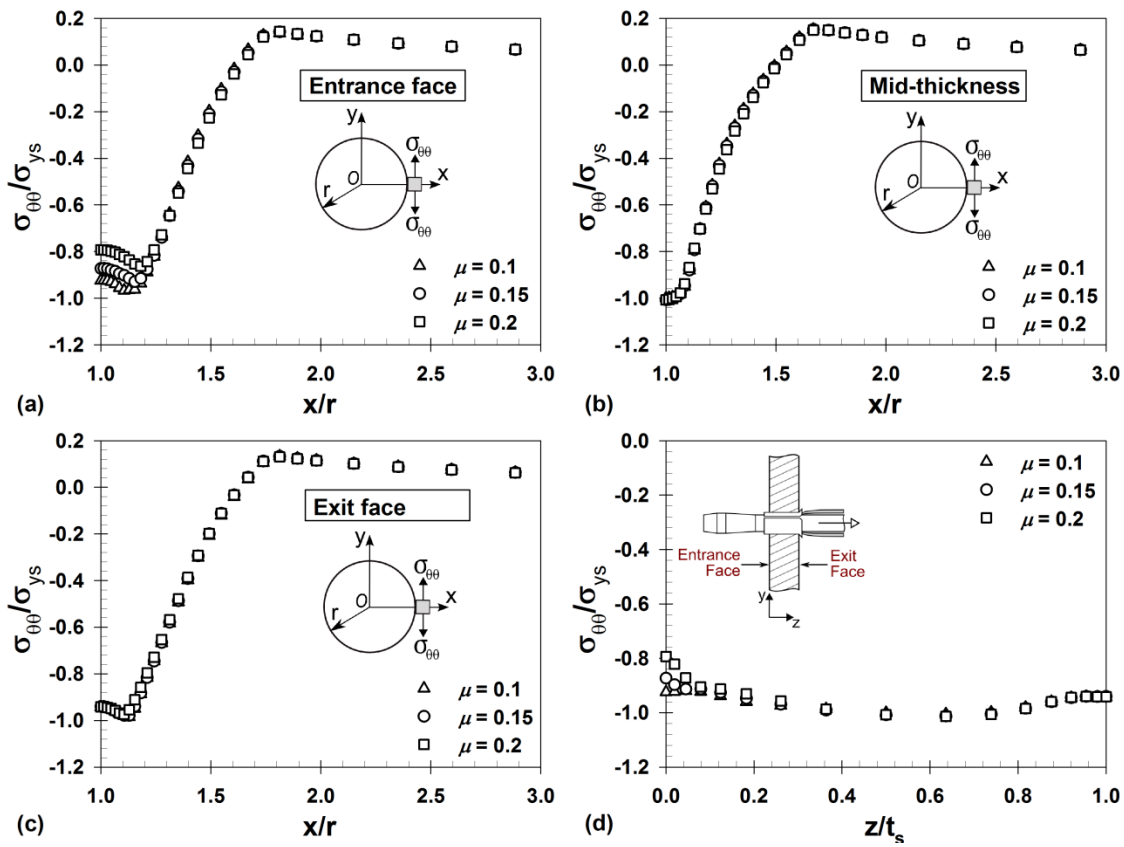

Figure 47. Normalized Circumferential Residual Stress Results for Different Friction Coefficients for Thin Specimen (a) Entrance Face, (b) Mid-Thickness, (c) Exit Face, and (d) Through-Thickness Direction at $x/r = 1$ and $y = 0$

5.3.1.3 SPLIT SLEEVE VS. NON-SPLIT SLEEVE.

Figures 48 and 49 show the residual stress solutions from the FE model implementing a split and non-split sleeve with the case (a) BC and a friction coefficient of $\mu = 0.2$. The stress distributions for the two sleeve types on the plane $y = 0$ show no significant differences (figure 48(a)). However, that will not be when the hoop stress values along the hole circumference are compared. Figure 49 shows the circumferential residual stress contours from

the split and non-split sleeve models. It is observed that the state of stress in the non-split sleeve model is nearly axisymmetric, whereas the split sleeve model produced a nonuniform residual stress field along the hole circumference. This observation is quantified in figure 48(b), in which the normalized hoop stress values are plotted against the angular position from the positive *x*-axis at the hole entrance, mid-thickness, and exit faces. The influence of the split in the sleeve is clearly seen at the sheet entrance face and in the mid-thickness, although negligible variations are observed at the exit face of the sheet. At the entrance face, the hoop residual stress solutions from the split sleeve model are lower in magnitude in the angular intervals $-90° \leq \theta \leq -5°$ and $85° \leq \theta \leq 90°$, and they are higher in the remaining locations. For example, the differences between the stress values at the entrance face at $\theta = \pm 90°$ are nearly 9%. The maximum variation occurs at $\theta = 65°$ with a percentage difference of about 23%. Similarly, the non-split sleeve solutions are larger in the sheet mid-thickness in the angular locations from -90° to -15° and from 85° to 90°. The differences in the stress values at $\theta = -90$ and $\theta = +90$ are 18% and 5%, respectively. Thus, the orientation of the split in the sleeve during the hole-expansion process may have a considerable impact on the subsequent stress states around the hole.

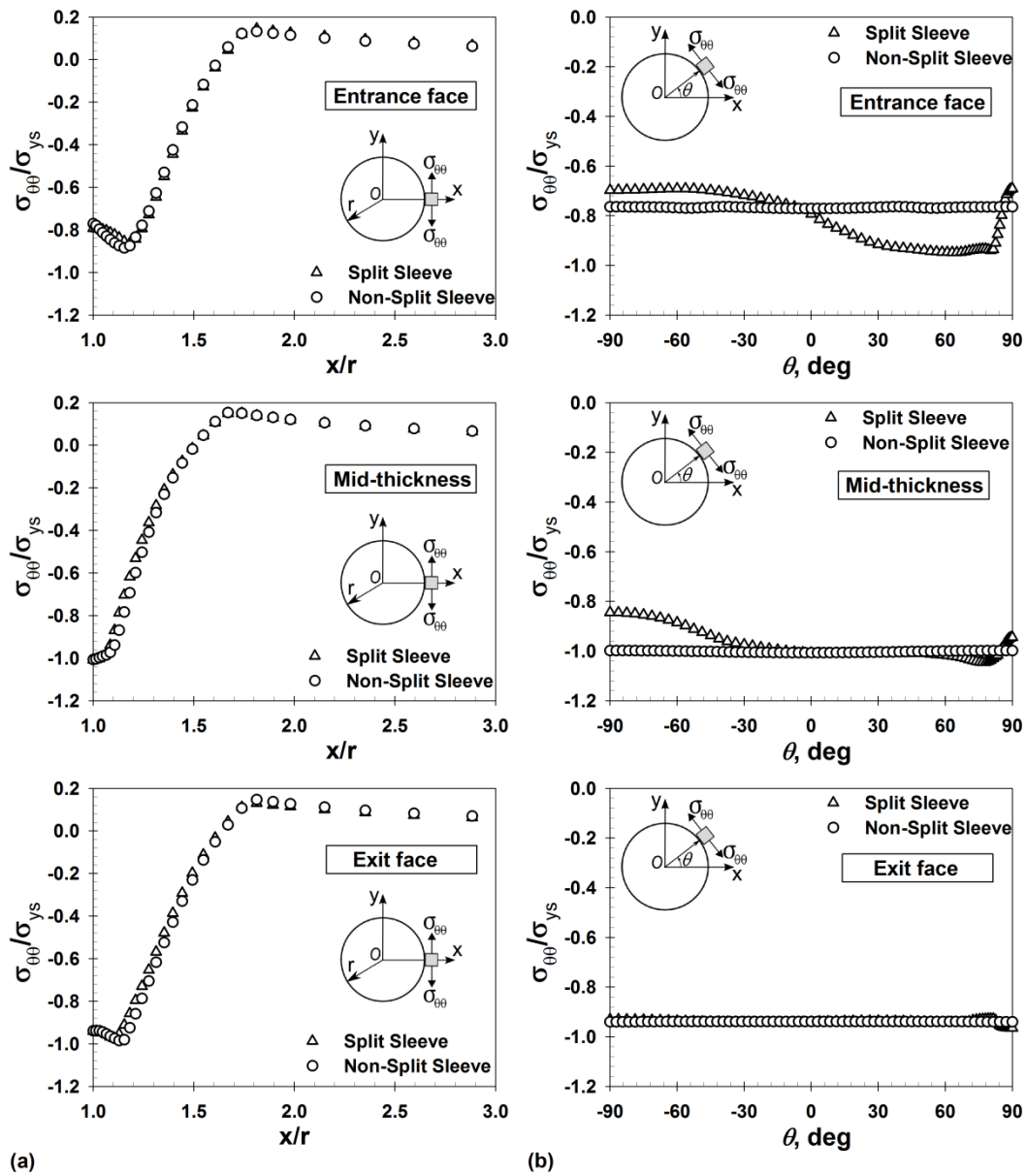

Figure 48. Circumferential Residual Stress Curves From Split Sleeve and Non-Split Sleeve Models for Thin Specimen (a) on the Plane $y = 0$; and (b) at the Hole Surface, with $\mu = 0.2$, and Case (a) BC

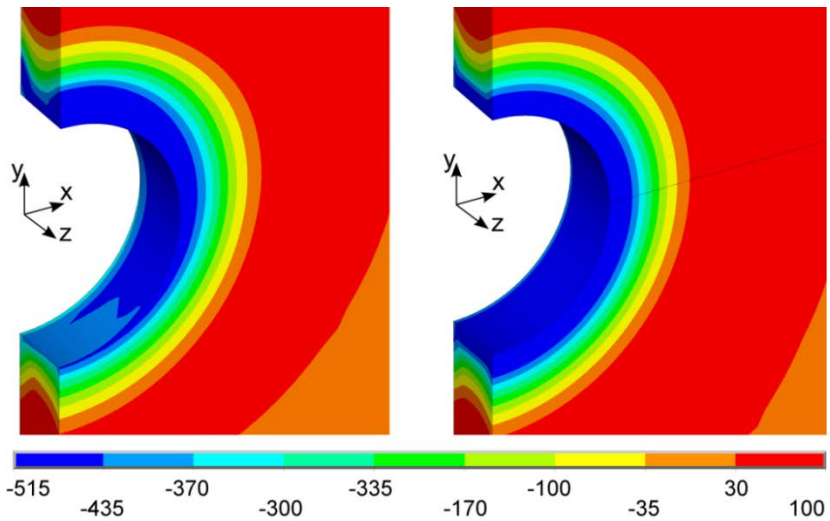

Figure 49. Circumferential Residual Stress Contours (in MPa) Around the Hole Edge of the Sheet for the Split Sleeve (left) and Non-Split Sleeve (right) Models of the Thin Specimen, $\mu = 0.2$, Case (a) BC

5.3.1.4 INFLUENCE OF BCs.

Figure 50 compares the residual stress results from the BCs of cases (a) and (b), with a friction coefficient of $\mu = 0.2$. Although the differences in the solutions from these models are not as significant as in some of the previous comparisons, variations are observed around the mid-thickness and at the entrance face, as shown in figure 50(d). The maximum percentage difference is calculated to be nearly 8% at the hole edge of the sheet entrance face. At the exit face of the sheet, the solutions are approximately identical.

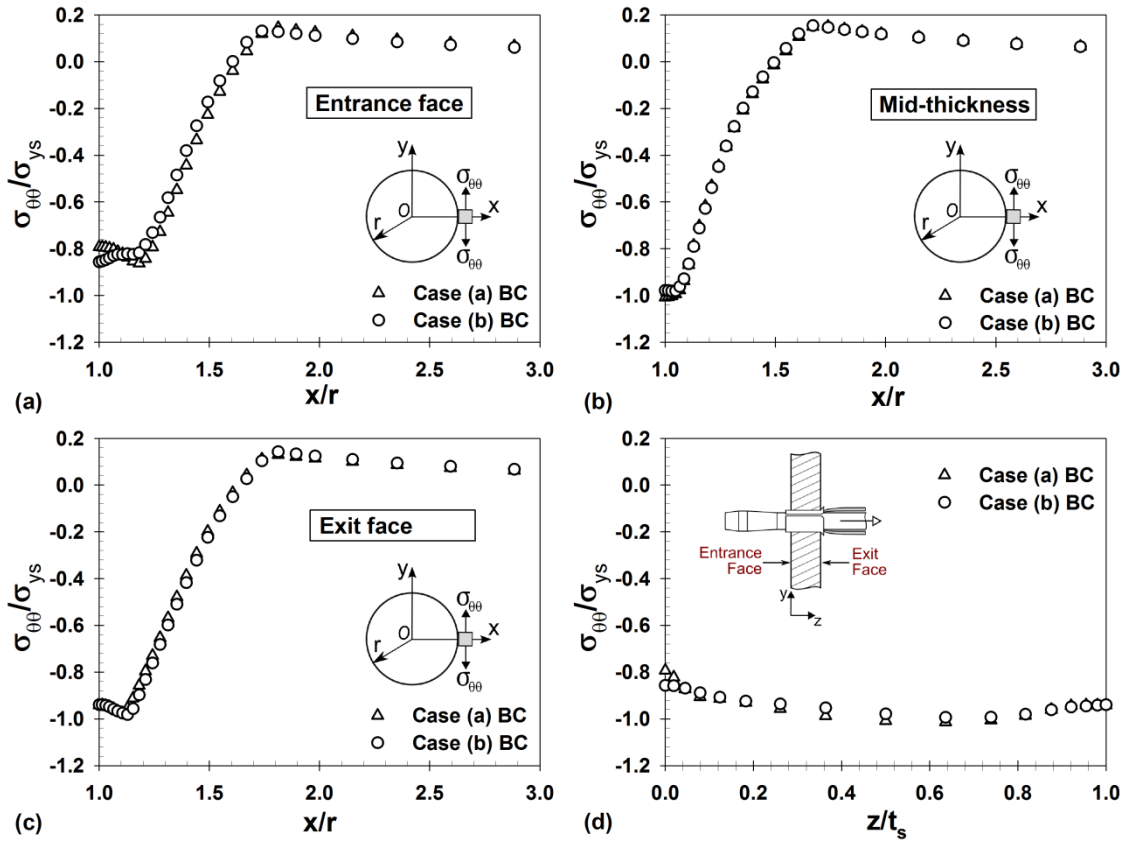

Figure 50. Normalized Circumferential Residual Stress Results for Cases (a) and (b) BCs With $\mu = 0.2$ for Thin Specimen (a) Entrance Face, (b) Mid-Thickness, (c) Exit Face, and (d) Through-Thickness Direction at $x/r = 1$ and $y = 0$

5.3.2 THICK SPECIMEN.

5.3.2.1 NUMERICAL SOLUTION VS. EXPERIMENTAL MEASUREMENTS.

Figure 51 compares the FE solutions with the experimental measurements at various through-thickness positions on the plane $y = 0$. The dashed and solid curves represent the numerical solutions from the isotropic and kinematic work-hardening material models, respectively, with the case (a) BC. Friction coefficient $\mu = 0.2$ is used at the sleeve-hole interface. The HE contour method measurements are represented by symbols in the figure. It is observed that the FEM solutions show a significant reduction in the residual stress magnitudes near the hole entrance face of the thick specimen (figure 51(a)). The residual stress values from the isotropic- and kinematic-hardening models at the entrance edge of the hole is slightly less than a half of the material yield strength (i.e., $\sigma_{\theta\theta}/\sigma_{ys} = 0.48$), whereas the average measured value at the same location is $\sigma_{\theta\theta}/\sigma_{ys} = 0.84$ (compressive). Also, the residual stress curves exhibit sub-surface minimums and the stress field extends deeper into the plate material at the exit face compared to the experimental data (figure 51(e)). However, at all other through-thickness positions the FEA solution correlates well with the measurements (figure 51(b-d)). As shown in figure 51(f), the isotropic-hardening material model gives a better prediction of the residual stress magnitudes at

the hole surface for the thick specimen compared to the kinematic-hardening rule. Therefore, the isotropic-hardening model is used for the remainder of the computations, the results of which are shown in figure 51.

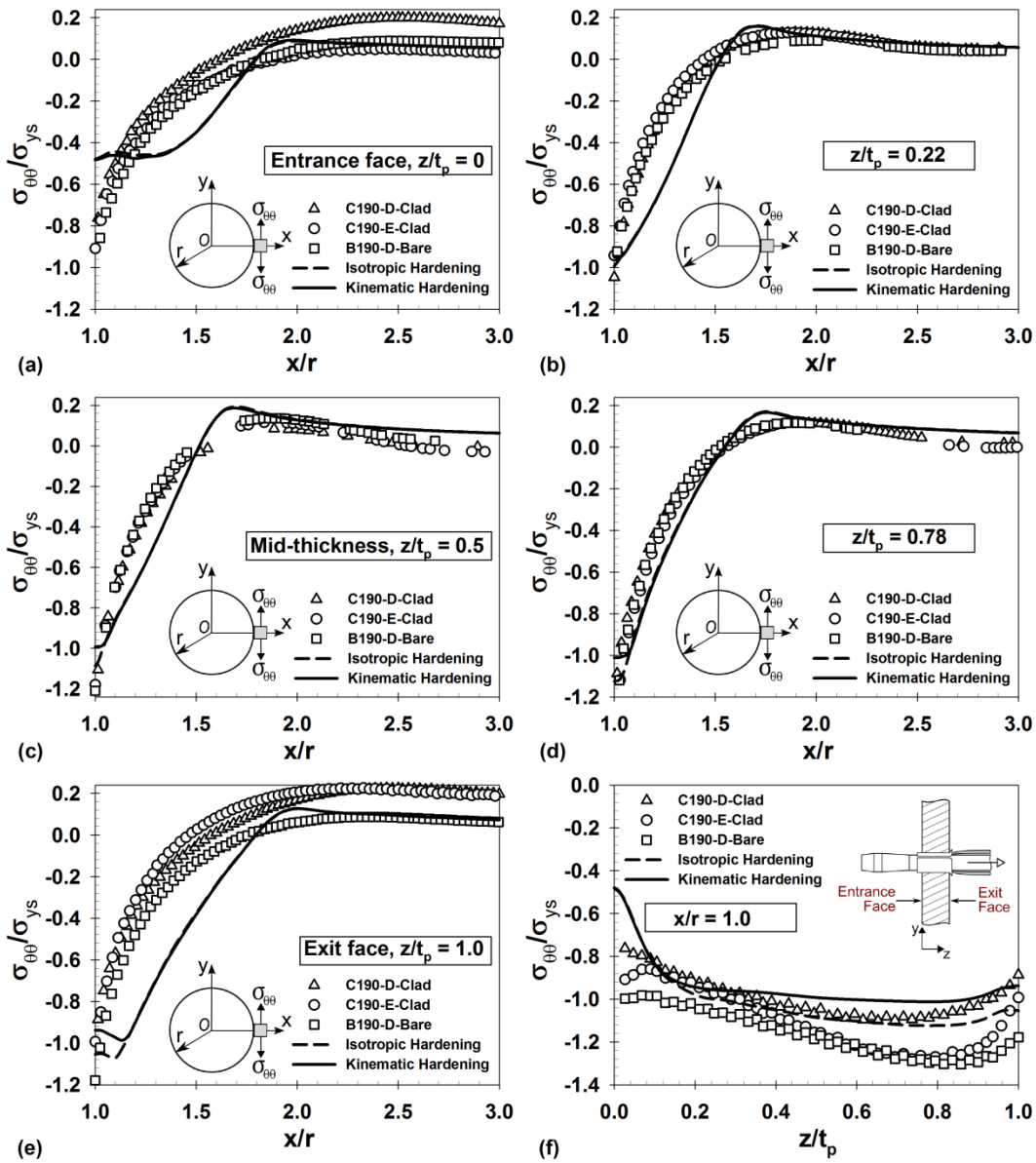

Figure 51. Normalized Circumferential Residual Stress Results From Isotropic- and Kinematic-Hardening Material Models Compared With Experimental Measurements for Thick Specimen (a) Entrance Face, (b) z/t_p = 0.25, (c) Mid-Thickness, (d) z/t_p = 0.75, (e) Exit Face, and (f) Through-Thickness Direction at x/r = 1 and y = 0

5.3.2.2 INFLUENCE OF FRICTION.

Figures 52 shows the residual stress results from the FE model with the case (a) BC and friction coefficients of 0.1, 0.15, and 0.2. The friction does not seem to have much influence on the

results at the plate entrance, mid-thickness, and exit faces. The major variation is observed at the through-thickness position z/t_p = 0.25, where the higher friction coefficient produced higher circumferential residual stress magnitudes (figure 52(d)). The maximum percentage difference in the results between the friction coefficients of 0.1 and 0.2 is approximately 7%.

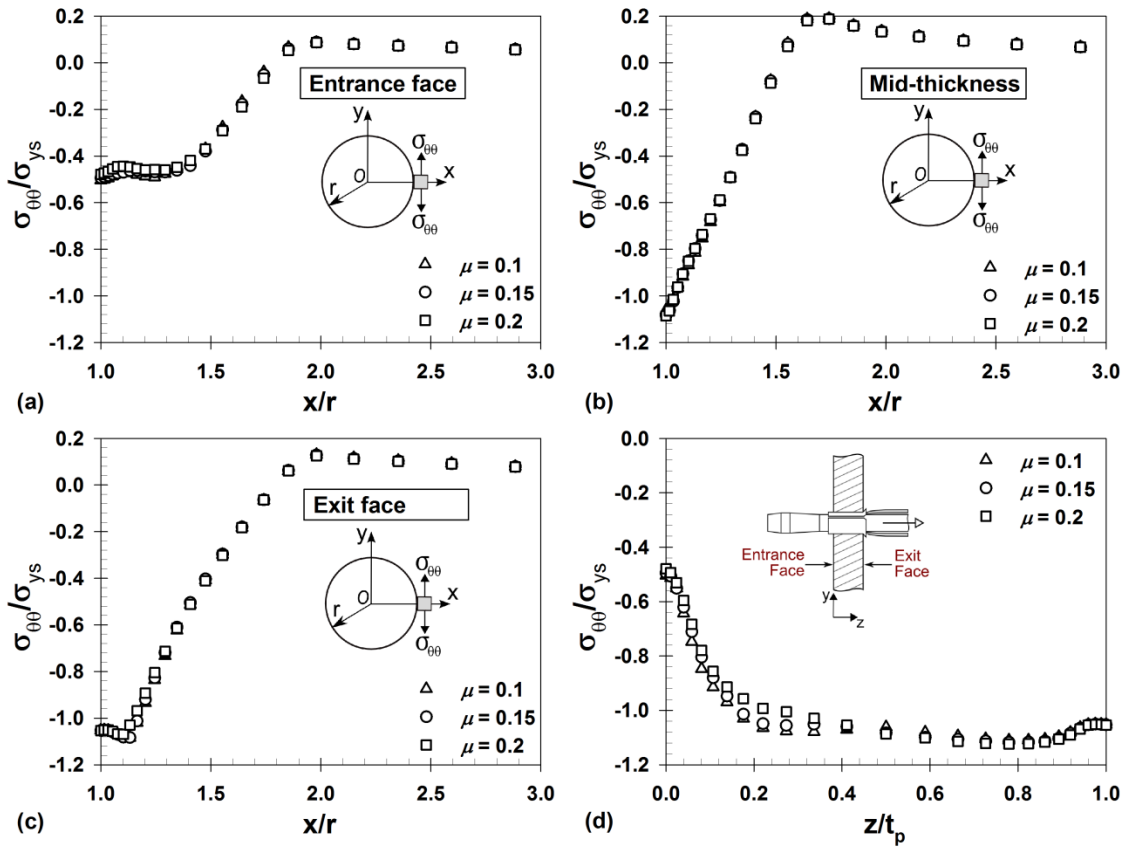

Figure 52. Normalized Circumferential Residual Stress Results for Different Friction Coefficients for Thick Specimen, (a) Entrance Face, (b) Mid-Thickness, (c) Exit Face, and (d) Through-Thickness Direction at x/r = 1 and y = 0

5.3.2.3 SPLIT SLEEVE VS. NON-SPLIT SLEEVE.

Figure 53 shows the residual stress solutions from the FE model implementing a split and non-split sleeve with the case (a) BC and a friction coefficient of μ = 0.2. At the entrance face, the maximum percentage difference between the stress curves is about 8% (figure 53(a)) and the stress magnitudes in the mid-thickness and exit face are nearly the same.

Greater variations are observed when the hoop stress values along the hole circumference are compared. In figure 53(b), the normalized hoop stress values are plotted against the angular position from the positive x-axis at the hole entrance, mid-thickness, and exit faces. As the angular position θ approaches 80°, the residual stress magnitude from the split sleeve model spikes up to $\sigma_{\theta\theta}/\sigma_{ys}$ = 1.05 (compressive) at the entrance hole edge (figure 53(b)). This corresponds to the absolute maximum residual stress variation zone between the split and non-

split sleeve models with a calculated percentage difference of nearly 60%. The fluctuation in the residual stress curve of the split sleeve model along the hole circumference gradually fades away as the through-thickness position z/t_p approaches unity (i.e., exit face). The stress magnitudes from the non-split sleeve model do not exhibit much fluctuation for each through-thickness location as shown in figure 53. At the exit face of the plate, the residual stress solutions from the split and the non-split sleeve models are nearly the same (figure 53(b), bottom).

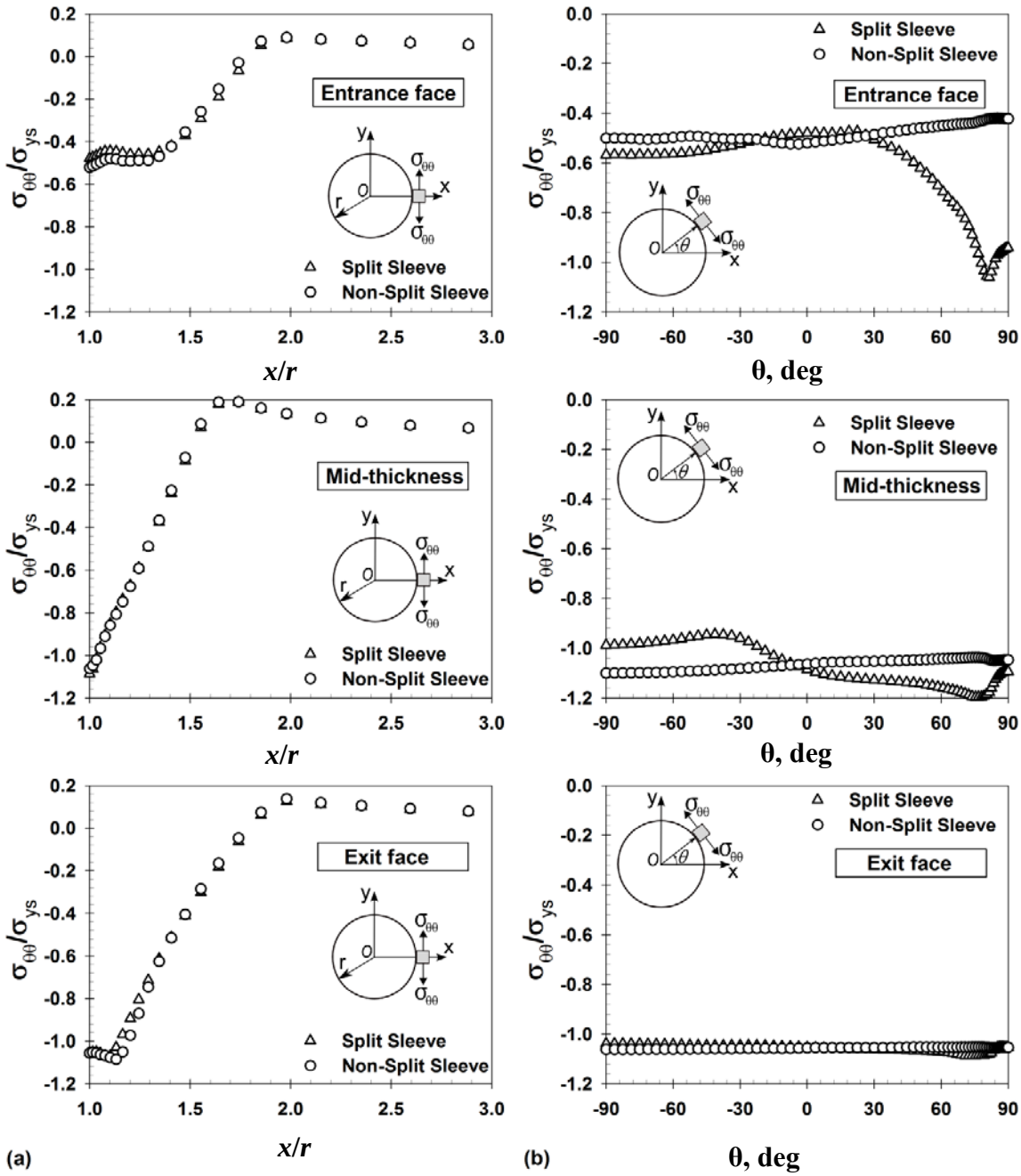

Figure 53. Circumferential Residual Stress Curves From Split Sleeve and Non-Split Sleeve Models for Thick Specimen (a) on the Plane $y = 0$ and (b) at the Hole Surface, with $\mu = 0.2$ and Case (a) BC

5.3.2.4 INFLUENCE OF BCs.

Figure 54 compares the residual stress results from the case (a) and case (b) BCs, with a friction coefficient of μ = 0.2. Implementing the case (b) BC produced residual stresses with considerably lower magnitudes with the highest percentage differences of approximately 28% and 15% at the entrance face and exit faces of the plate, respectively. In figure 54(d), the residual stress magnitudes are plotted in the *z*-direction, in which variations in the solutions are observed from the plate entrance face to the mid-thickness ($0 \leq z/t_p \leq 0.5$) as well as in the area of the exit face with case (b) BC giving lower residual stress values.

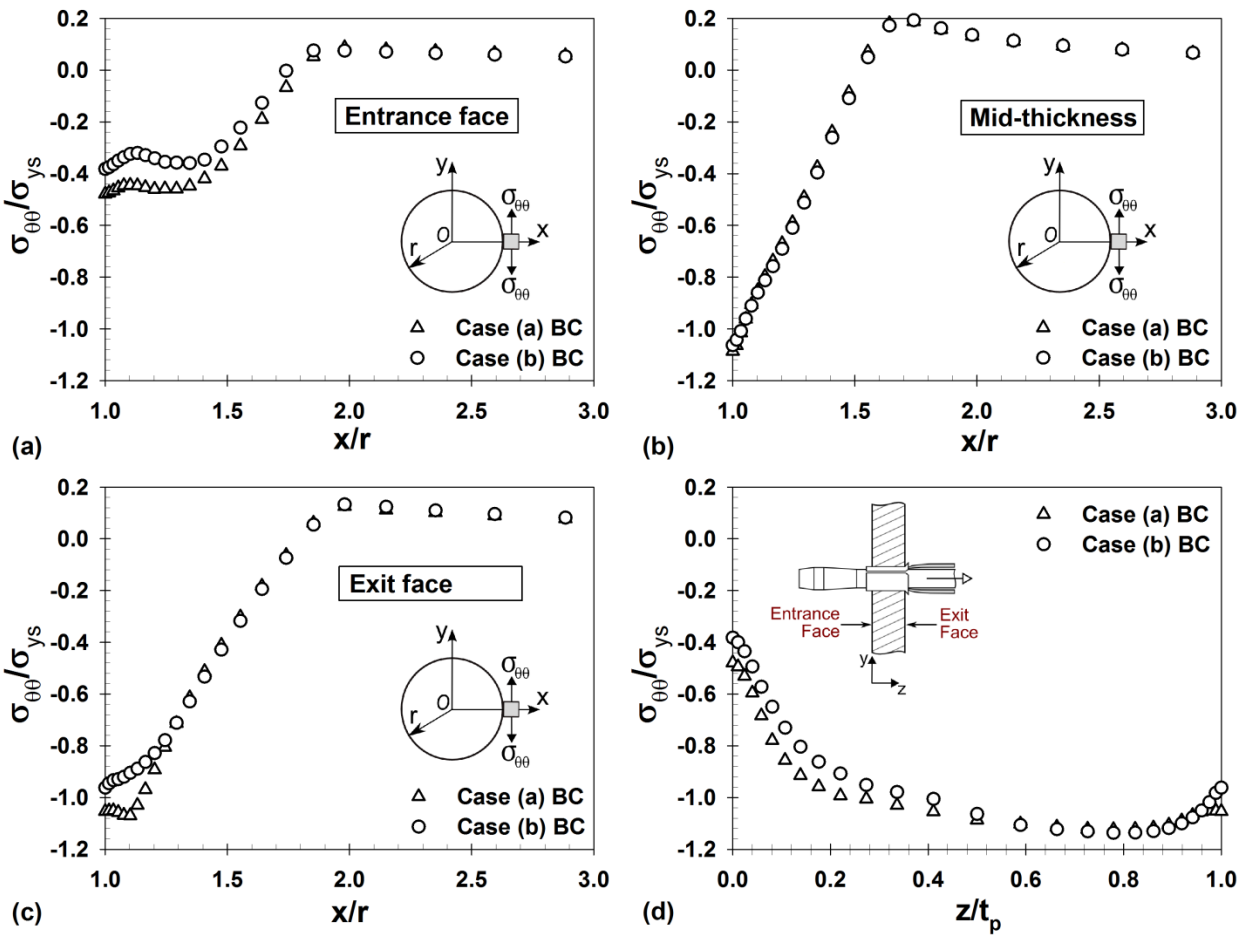

Figure 54. Normalized Circumferential Residual Stress Results for Cases (a) and (b) BCs With μ = 0.2 for Thick Specimen (a) Entrance Face, (b) Mid-Thickness, (c) Exit Face, and (d) Through-Thickness Direction at x/r = 1 and y = 0

5.4 CONCLUSIONS.

Detailed 3D numerical simulations of the CX and reaming processes were carried out on a rectangular aluminum sheet with a centrally located hole. Two different sheet thicknesses were considered. The model included an elastic steel split sleeve and a rigid tapered mandrel. Large strain effects were included in the analysis by selecting the geometrical nonlinearities option in

ANSYS. The CX process was simulated by pulling a tapered mandrel through the hole, whereas the reaming was performed by deactivating a layer of elements along the hole periphery. The following conclusions can be made from this work:

1. The tangential residual stress distributions in the radial direction from the simulation results were in general agreement with the experimental measurements in the subsurface regions of the material. For the thin specimen, the material model employing the kinematic-hardening rule gave a better prediction on the stress magnitudes when compared with the isotropic-hardening rule near the hole surface. For the thick specimen, however, FE solutions with the isotropic-hardening rule compared well with experimental data in the vicinity of the hole. Additional data from more duplicate tests are needed to fully analyze the through-thickness distribution. The FEA results indicated that the residual stress magnitude is the lowest at the entrance face, which is more pronounced for the thick specimen.

2. The mandrel entrance face was found to be the most sensitive region to friction between the sleeve outer surface and the hole of the thin specimen, where the higher friction coefficients produced residual stresses with lower magnitudes. For the thick specimen, the friction does not seem to have much influence on the results at the plate entrance, mid-thickness, and exit faces. The major variation was observed at the through-thickness position $z/t_p = 0.25$, where the higher friction coefficient produced higher circumferential residual stresses. Further research is needed to better understand the influence of the friction coefficient.

3. Inclusion of the split in the sleeve resulted in a nonuniform residual stress field along the hole circumference, whereas the non-split sleeve model created a nearly axisymmetric state of stress. Thus, it is important to know the orientation of the split in the sleeve during the CX process to accurately predict the residual stress magnitude at a specific location around the hole.

4. Greater variations were observed in the solutions for the thick specimen when two different sheet constraints were used (cases (a) and (b)). The highest percentage differences in the hoop stress magnitudes were approximately 28% and 15% at the entrance and exit faces of the plate, respectively. The differences for the thin specimen were primarily at the entrance face and in the mid-section, where a difference of up to 8% was observed.

6. STRESS AND CRACK ANALYSES FOR PIN-LOADED HOLES.

6.1 ELASTIC-PLASTIC STRESS ANALYSIS OF COLD-WORKED PIN-LOADED HOLES.

6.1.1 INTRODUCTION.

Fastener joints have a broad range of applications in many engineering structures. These joints are considered a potential failure location because of the localized stress concentrations caused by the presence of the holes. Pin loading is a well-known problem, that has attracted the

attention of many researchers in the past. Numerous independent techniques have emerged to evaluate the stress state around a pin-loaded hole. Experimental methods include photoelasticity [94-96], moire interferometry [97-98], electronic speckle pattern interferometry [99], and strain gages [95]. Analytical solutions have been developed using linear elasticity with complex variable methods [100-103] and stress functions [104-109]. Noble and Hussain [100], for example, considered the problem of an infinite plate with a circular hole loaded by a pin under frictionless conditions. They formulated the problem in terms of dual series, which are then converted to an equivalent Cauchy-type or airfoil equation, assuming the elastic constants of the pin and the plate satisfy the relationship $(1\text{-}2\nu_1)/G_1 = (1\text{-}2\nu_2)/G_2$, where G and ν denote the shear modulus and Poisson's ratio, respectively. Rao [104] used an inverse method along with a collocation technique to solve for the unknown constants in an Airy stress function satisfying the prescribed BCs. He considered both frictionless and nonzero friction, bonded interfaces, and clearance and interference fit pins. Mangalgiri et. al. [105] extended the work of Rao for pin joints under combined pin and plate loads with frictionless contact. In reference 101, a complex Fourier series, collocation procedure, and iteration technique were used to solve for stresses around pin-loaded orthotropic plates for different levels of friction as well as for the hole clearance. For the case of a rigid pin and zero friction, Muzushima and Hamada [106] also adopted a numerical approach to solve for the stress and displacement distributions around the loaded hole. Ho and Chau's work [107] regarding an infinite plate loaded by a pin is one of the recent closed form solutions that include friction, arbitrary stiffness for the pin material, and uniform and non-uniform shear loads distributed over the pin section. They solve the problem by partitioning it into two auxiliary sub problems. The first sub problem solves for the stress distribution in the plate loaded by a pin of a different material that is perfectly bonded to the plate. The second auxiliary problem needs a solution that allows the normal σ_{rr} and shear $\sigma_{r\theta}$ stress components to cancel out at the top half of the circular boundary ($0° \leq \theta \leq 180°$, $r = R$), whereas the normal and shear contact stress distributions proportional to $sin(\theta)$ and $sin(2\theta)$ are produced at the bottom half of the hole ($-180° \leq \theta \leq 0°$, $r = R$; see figure 55). The sinusoidal radial pin load distribution assumption is also used in the development of an analytical solution for pin-loaded elastic orthotropic plates via complex stress functions for frictionless conditions ($\mu = 0$) [103].

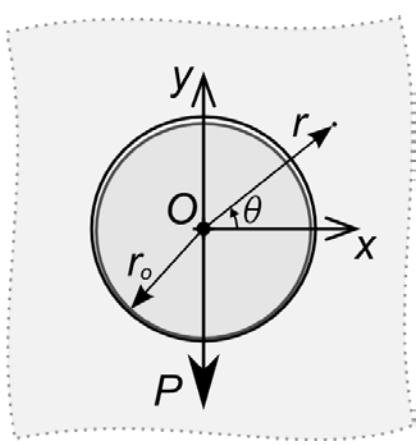

Figure 55. An Infinite Sheet Loaded by a Resultant Pin Load *P*

These analytical solutions are obtained for a linear elastic plate material. However, the problem becomes more complicated if one considers the material non linearity combined with friction and finite plate dimensions. Additionally, pinned connections rarely occur in isolation because most of the structures have multiple pinned connections with dissimilar configurations. This makes the FEM a more desirable approach because it can eliminate these concerns as long as the model size is kept at a reasonable level. The 2D FEA of the pin-loaded plates with an elastic plate, rigid pin, and frictionless contact have been researched [108-110]. Local stress distributions from 2D and 3D FE models with elastic pins and frictionless contact were presented by Iyer [111]. Iyer and Lanza di Scalea consider both pin elasticity as well as friction in their 2D plane strain [113] and plane stress [99] models. Iyer demonstrated that the stress solutions at the interface are largely independent of the material pair if the pin and the plate are metallic and friction is small. Yavari et al. [112] performed a parametric study with respect to some design factors, such as the plate width, edge distance, clearance, and friction at the pinhole interface. Kumar [113] included material plasticity for the case of a perfectly smooth pinhole interface (i.e., $\mu = 0$) and obtained the stress distributions around the hole under constant-amplitude cyclic loading.

The objective of this report is to continue the 2D FE modeling efforts of the pin-loaded hole problem with further sophistication, namely considering the material nonlinearity and friction as well as pre-existing residual stresses around the hole from cold hole expansion. First, convergence studies were performed to validate the elastic and elastic-plastic model results. Furthermore, the FE model with linear elastic material properties was validated using a closed form solution by Ho and Chau [107] and an FE solution by Yavari et. al. [112]. Next, the linear elastic and elastic-plastic solutions were compared, and the influence of the friction was studied. Finally, a compressive residual stress field was introduced around the hole by CX simulation. The CX of a hole, initially developed by the Boeing Company in 1960, is a life enhancement process used to mitigate the effects of the stress concentrations by creating a compressive circumferential residual stress field around the hole [75]. Because this process involves some reverse yielding, the effect of both isotropic- and kinematic-hardening material models were considered. The sheet was then pin-loaded and the subsequent changes in the stress state around the hole were presented.

6.1.2 CONFIGURATON AND MATERIAL MODELS.

Figure 56 shows a rectangular finite sheet with a circular hole as a model configuration. The size of the thin rectangular sheet is 65.0 mm (h) by 44.45 mm ($2w$), with a 7.07-mm-diameter hole ($2r_o$) located at 22.23-mm distance (d) from the bottom edge. The sheet thickness is t = 2.03 mm. The hole is loaded by a neat-fit pin with a magnitude P. The sheet is constrained in the y-direction at the top edge (figure 56). The diameter of the pin is the same as the hole diameter because it is a neat-fit configuration. Out-of-plane bending effects for the sheet are ignored, which can be a reasonable approximation for the dual lap joints. This simplification may not be appropriate for single lap pin joints.

The sheet material is 7075-T6 aluminum alloy with a yield strength of (σ_{ys}) of σ_{ys} = 483 MPa. The Young's modulus and Poisson's ratio are E = 72.5 GPa and ν = 0.3, respectively. Figure 42 shows the stress-strain curve used in the analyses [89]. For the elastic case, only the elastic

domain of the curve is used. Thus, the Young's modulus and Poisson's ratio are sufficient parameters to describe the material behavior. For the elastic-plastic analysis, the stress-strain data in both elastic and plastic domains are used with the von Mises yield criterion. Two different work-hardening material models were considered during the CX simulation: multilinear isotropic hardening and multilinear kinematic hardening. These two hardening models result in different residual stress fields from the CX simulation because of the Bauschinger effect, which is incorporated into the kinematic hardening material model. For simplicity, the pin is assumed to be a rigid body.

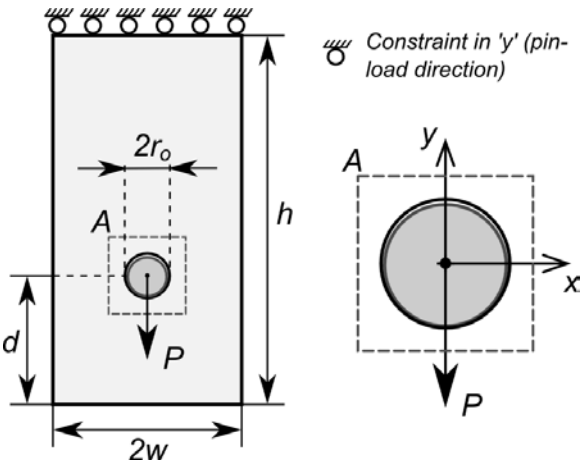

Figure 56. Pin-Loaded Hole Model Configuration

6.1.3 THE FE MODEL AND BCs.

ANSYS [92] was used to carry out the numerical simulations. The 2D plane stress conditions were assumed because of the small sheet thickness. Because of symmetry, one half of the specimen was modeled with appropriate symmetry BCs, which are shown as vertical rollers in figure 57. These rollers are the constraints in the *x*-direction, whereas the horizontal rollers applied at the top edge of the sheet indicate the constraints in the *y*-direction.

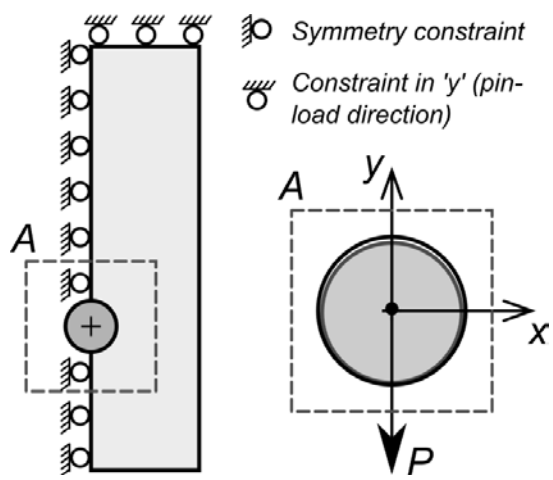

Figure 57. Prescribed BCs of the FE Model

The FE model was meshed using 2D four-noded linear structural elements with a highly refined mesh around the hole edge (figure 58). Rigid-to-deformable surface-to-surface contact elements with an augmented Lagrangian algorithm were used at the pinhole interface so that the normal and shear traction loads can be transferred from the pin to the hole surface. Two different cases were studied regarding the friction. In the first case, the pinhole interface was assumed to be perfectly smooth with zero friction. In the second case, a Coulomb friction model was used with an arbitrary friction coefficient $\mu = 0.2$.

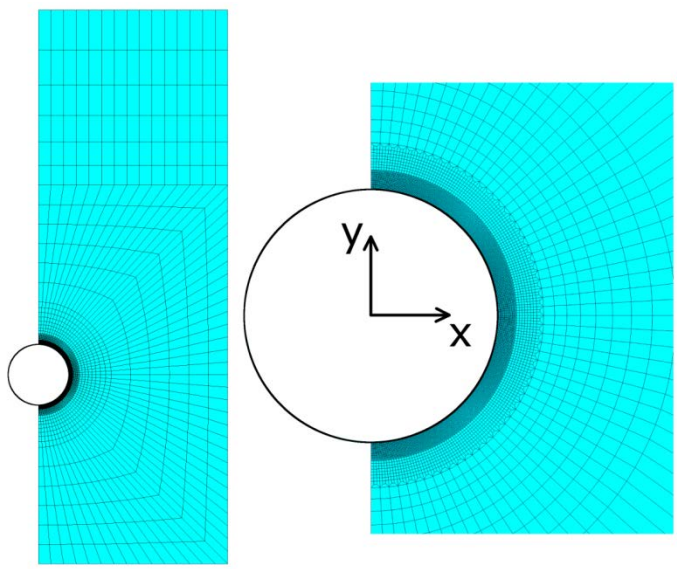

Figure 58. The FE Mesh for the Pin-Loaded Hole Model

Assuming that the pin loading is a sufficiently slow process, it was simulated in a quasistatic manner without considering any dynamic or time-dependent response of the material. The magnitude of the point load *P*, which is applied downward at the center of the pin (figure 57), was gradually increased in several load steps up to the maximum level. Note that the point load is, in general, not realistic because the shear loads are distributed over the pin section in some fashion. However, this does not apply to the current research because the pin was assumed to be rigid.

In the last stage of the study, a residual stress field was created around the hole by CX simulation prior to subsequent pin loading analyses. The CX is a 3D process in which a tapered mandrel is pulled through the hole of the structure and the resulting residual stress field varies through the sheet thickness [114]. Although it is not possible to realistically simulate the actual process in 2D, it can be performed in a rather simplistic way by doing the following:

1. Hole Expansion—Uniform radial displacements, equal to the 2% interference amount, are applied on the nodes of the hole edge. By this means, the hole of the sheet is plastically expanded.

2. Hole Recovery—Preapplied displacements are removed, which causes the partial, but not full, elastic recovery. This step creates the desired compressive residual stresses around the hole edge.

6.1.4 MODEL VALIDATON.

The 2D elastic and elastic-plastic FE models were first validated by performing convergence studies with respect to mesh density and loading increments (i.e., total number of load steps). Figure 59 shows example convergence studies for the elastic-plastic model with friction coefficients μ = 0 and 0.2. In each plot of the figure, normalized stress values (σ_{ij}/σ_{ys}) for progressively refined element sizes L are plotted versus the angular location θ along the hole circumference. The applied normalized pin load magnitude is S_b/σ_{ys} = 1.0, where S_b is the average bearing stress:

$$S_b = \frac{P}{2r_o t} \tag{18}$$

Here, P is the pin load magnitude, r_o is the hole radius, and t is the thickness of the sheet.

It is noted that L is the length of the elements at the hole edge normalized by πr_o. By default, in ANSYS, L was reduced by a factor of three during each mesh refinement. As shown in figure 50(a) and (b)), both radial and hoop stress distributions are easily converged in the frictionless case when L is reduced to $L = 0.01\times3^{-2}$. Including a friction coefficient $\mu = 0.2$ resulted in a slow local convergence in the vicinity of the angular location $\theta = -90°$. Although it may be expected that the radial stress magnitude (σ_{rr}/σ_{ys}) near $\theta = -90°$ could be converged with the smallest element size, $L = 0.01\times3^{-5}$, the hoop stress values ($\sigma_{\theta\theta}/\sigma_{ys}$) require further mesh refinement (figure 59(c) and (d)). Results away from this region are readily converged with the same level of mesh refinement as in the frictionless case (i.e., $L = 0.01\times3^{-2}$). Similar behavior was observed when linear elastic material properties were used for the sheet, suggesting that the friction, as well as the rigid pin assumption, may be the source of the convergence difficulties. Because the smallest element size considered in this study ($L = 0.01\times3^{-2}$) led to an impractically large model size with approximately 450K degrees of freedom, the second level of mesh refinement with $L = 0.01\times3^{-2}$ was chosen to be the final and optimum mesh density for all cases. In the results that follow for $\mu = 0.2$, attention is confined to the interval $-85° \le \theta \le 90°$, where the solutions are converged.

Further validations were done by solving two previously studied independent problems found in the literature: (1) a closed-form solution by Ho and Chau [107] for an infinite sheet and (2) a

numerical solution by Yavari et. al. [112]. The Ho and Chau solution states that, if the pin is assumed to be rigid ($E_{pin} \rightarrow \infty$), the contact stresses are:

$$\sigma_{rr} = \begin{cases} \dfrac{PM_1 sin(\theta)}{\pi r_0} & \text{for} \quad -\pi \le \theta \le 0 \\ 0 & \text{for} \quad 0 \le \theta \le \pi \end{cases}$$
$$\sigma_{r\theta} = \begin{cases} -\dfrac{PM_2 sin(2\theta)}{\pi r_0} & \text{for} \quad -\pi \le \theta \le 0 \\ 0 & \text{for} \quad 0 \le \theta \le \pi \end{cases} \tag{19}$$

The parameters M_1 and M_2 are related to the friction coefficient μ by:

$$M_1 = \frac{6\pi}{3\pi + 4\mu}$$
$$M_2 = \frac{3\pi \times \mu}{3\pi + 4\mu} \tag{20}$$

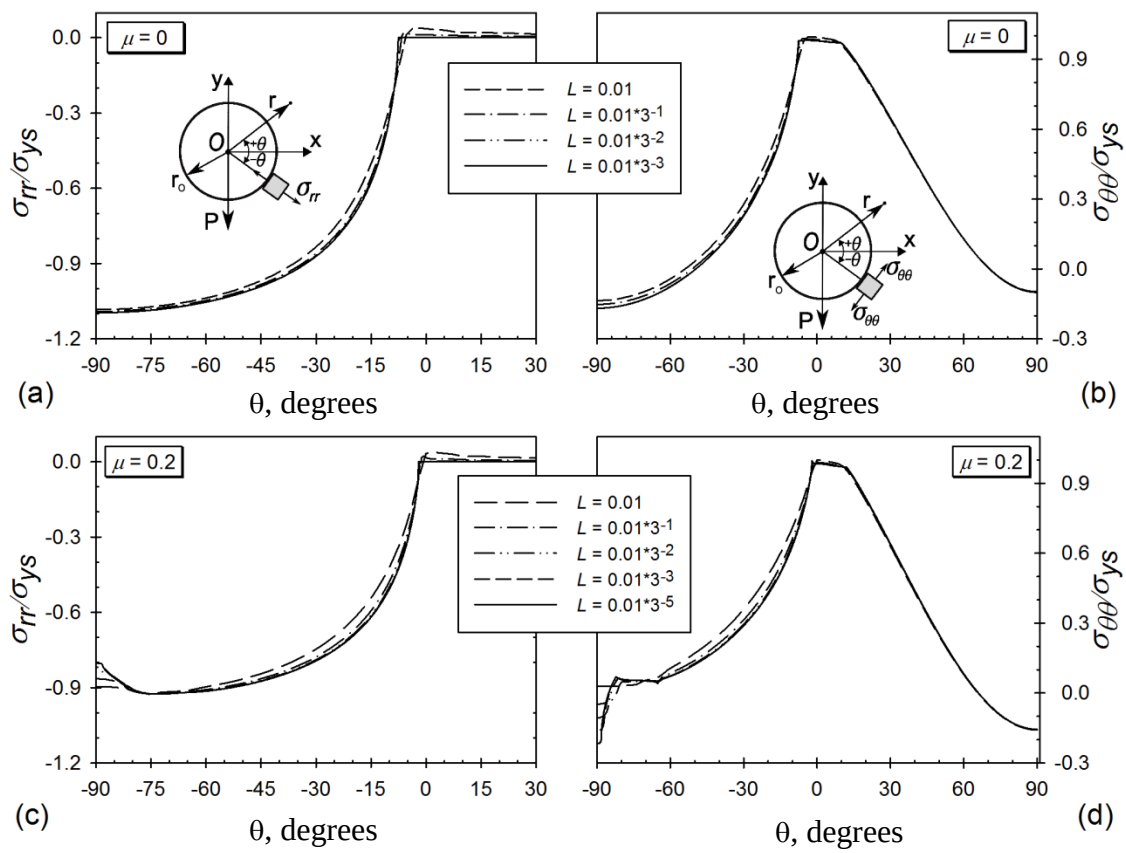

Figure 59. Convergence Studies for Radial and Hoop Stress Distributions at $r = r_o$, L is Element Size at the Hole Edge (normalized by πr_o)

The shapes of the normal and shear stress distributions at the pinhole interface given in equation 19 were assumed during the solution process. The stress components σ_{rr} ,$\sigma_{r\theta}$, and $\sigma_{\theta\theta}$ then determined in the sheet and the pin. For the rigid pin, the hoop stress component $\sigma_{\theta\theta}$ along the hole circumference of the sheet under plane stress conditions was:

$$\sigma_{\theta\theta} = \begin{cases} \dfrac{P}{\pi r_0}\left[\left(\dfrac{2}{\pi} + sin(\theta)\right)M_1 + \left(cos(2\theta) - \dfrac{4}{3\pi}sin(\theta) + \right.\right. \\ \qquad \left.\left. + \dfrac{2}{\pi}sin(2\theta)tanh^{-1}(cos(\theta))\right)M_2 - \left(\dfrac{\nu}{2} + \dfrac{1}{2}\right)sin(\theta)\right] & \text{for } -\pi/2 \le \theta < 0 \\ \dfrac{P}{\pi r_0}\left[\dfrac{2}{\pi}M_1 + \left(cos(2\theta) - \dfrac{4}{3\pi}sin(\theta) + \dfrac{2}{\pi}sin(2\theta)tanh^{-1}(cos(\theta))\right)M_2 - \right. \\ \qquad \left. - \left(\dfrac{\nu}{2} + \dfrac{1}{2}\right)sin(\theta)\right] & \text{for } 0 < \theta \le \pi/2 \\ \dfrac{P(2M_1 + \pi M_2)}{\pi^2 r_0} & \text{for } \theta = 0 \end{cases} \tag{21}$$

where ν is the Poisson's ratio of the sheet material [107].

To model an infinite sheet in ANSYS, a large finite square sheet with w/r_o = 100 was created. A concentrated pin load P per unit thickness was applied downward at the center of the rigid, neat-fit pin, while the top edge of the sheet was constrained in the pin load direction. A modulus of elasticity of E = 72 GPa and a Poisson's ratio of ν = 0.3 were used for the sheet. Figure 60(a and b) show the normal and shear stress distributions along the hole circumference for μ = 0 and μ = 0.2. In addition, a $(sin(\theta))^{0.2}$ function, as suggested in reference 112, is included in the plots. All stress components are normalized as $\sigma_{ij}\cdot(\pi r_o/P)$. As shown in figure 60(a and b), differences are evident for both μ = 0 and μ = 0.2. It is observed from figure 60(a) that the $sin(\theta)^{0.2}$ better approximates the shape of the normal contact stresses rather than the function used in reference 107, which is proportional to $sin(\theta)$ (see σ_{rr} in equation 19). The numerical solution indicates that the edge of the downward slope corresponding to the boundary between the closed and open contact does not start at exactly θ = 0°. The shear stress values are zero everywhere on the hole surface as expected for μ = 0. Greater variations were observed in both shapes and magnitudes of the σ_{rr} , $\sigma_{r\theta}$ stress curves when a friction coefficient μ = 0.2 is considered. As shown in figure 60(b), normal contact stresses found from the Ho and Chau solution are lower in magnitude for -50°≤θ≤ 0° and they are greater in the range -85°≤ θ≤50° with a maximum percentage difference of 27% at θ = -85°. Also, the $(sin(\theta))^{0.2}$ function fails to capture the accurate shape of the normal stress curve when friction is included. Shear stress values are significantly smaller than the FE solutions in the entire range, with a maximum percentage difference of 175% at θ = -84°. Moreover, it was observed that the distribution of the shear stress was not exactly proportional to $sin(2\theta)$ [107].

Comparisons between the hoop stress solutions [107] with the FE results along the hole circumference are shown in figure 60(c and d) for μ = 0 and μ = 0.2, respectively. The

variations in the stress magnitudes shown can be partially explained by the different contact stress distributions used as BCs by Ho and Chau when compared to those predicted by the FE model. Percentage differences between the peak stress values are 11.5% and 18.9% for the cases with μ = 0 and μ = 0.2, respectively. However, it is observed that the analytical and numerical hoop stress curves follow a similar trend. In particular, increasing the friction coefficient raises the peak hoop stress value and lowers the stress magnitudes at the lower values of θ.

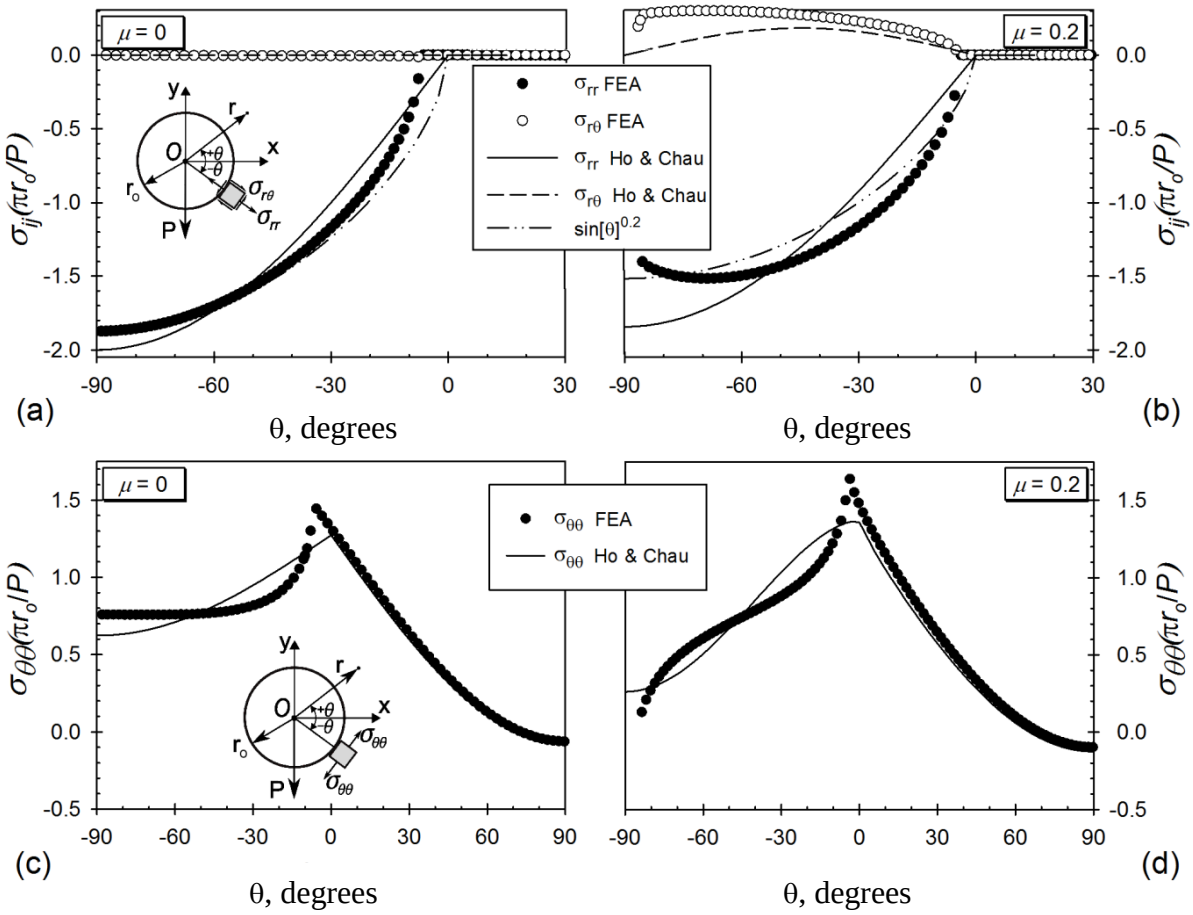

Figure 60. Comparison of Normal, Shear, and Tangential Stress Distributions Along the Hole Circumference ($r = r_o$) With Results [107]

For further validation, Yavari et al.'s 2D numerical analysis [112] regarding the stress distribution around the elastically pin-loaded hole in a finite sheet was replicated. The configuration of that model is similar to the one considered in the present study (see figure 56). The dimensions of the sheet are d = 15.3 mm, $2r_o$ = 6.12 mm, h = 168.3 mm, and $2w$ = 30.6 mm. The pin was modeled to be rigid, whereas E = 70 GPa and ν = 0.31 were used for the aluminum alloy sheet. A pin load P was applied downward at the pin center, keeping the top edge of the sheet constrained in the y-direction.

Figure 61 compares the normalized radial and hoop stress solutions along the hole circumference with the results for μ = 0 and 0.2 [112]. Stress components are normalized as $\sigma_{ij}(\pi\, r_o/P)$. As shown in figure 61(a), the radial stress distributions compare well for both friction levels. Hoop

stress curves were also in good agreement, although slight variations were observed for θ < 0° (figure 61(b)).

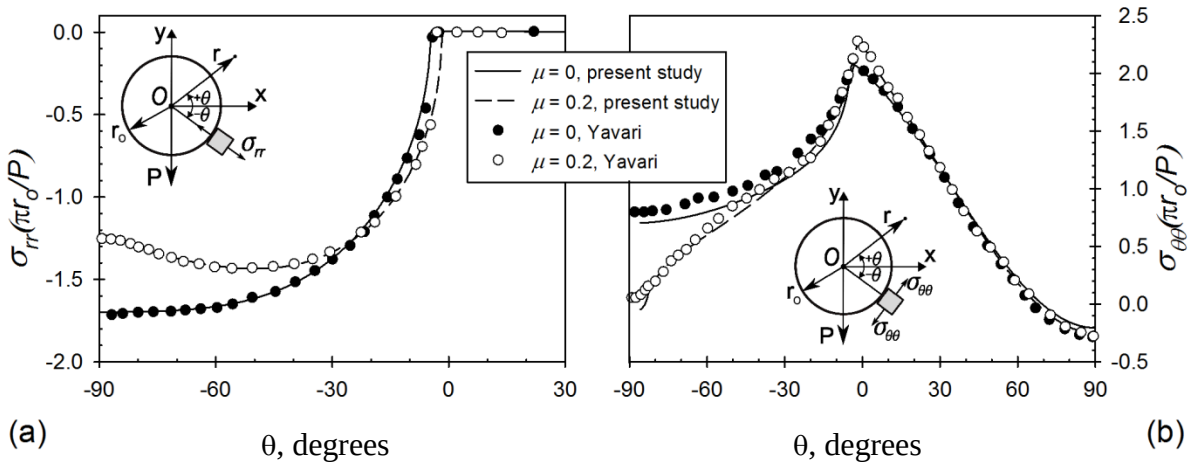

Figure 61. Comparison of the Normal and Tangential Stress Distributions Along The Hole Circumference ($r = r_o$) With Results [112]

6.1.5 RESULTS.

Figure 62 shows the comparisons between the stress solutions from the linear elastic and elastic-plastic models with μ = 0 and 0.2. In figure 62(a and b), normalized radial stress distributions σ_{rr}/σ_{ys} are plotted along the hole circumference for the normalized pin load magnitudes S_b/σ_{ys} = 0.2, 0.6, and 1.0. In general, the results did not vary significantly, although figure 62(b) shows a noticeable difference in the curve shapes for the applied pin load S_b/σ_{ys} = 1, and a friction coefficient μ = 0.2. Figure 62(c and d) shows the significant influence of the material nonlinearity on the hoop stress distributions when the applied load approaches its maximum level. For example, the peak hoop stress values for S_b/σ_{ys} = 1 were reduced by as much as 19% and 25% in the cases with μ = 0 and 0.2, respectively. Further variations were observed in the region θ < 0°, particularly in the frictionless case with S_b/σ_{ys} = 1, where the magnitudes of the hoop stresses from the elastic-plastic models were reduced by a significant amount. The stress solutions for the smaller applied loadings were in good agreement, as expected, because there was little plastic deformation.

The influence of friction can be studied by comparing the radial stress plots in figure 62(a) with that of (b), and the hoop stress plots in (c) with (d). The radial stress values are lower in the case with friction, which was more obvious for higher applied loadings (see figure 62(a and b). For example, when the pin load was S_b/σ_{ys} = 1, the maximum percentage difference between μ = 0 and 0.2 was approximately 22.5% at θ = -85°. It was observed that the friction raised the peak hoop stresses for the elastic material models, particularly when the applied loading was high (compare the open symbols in figure 62(c and d). The percentage difference between the elastic peak hoop stress magnitudes with μ = 0 and 0.2 was approximately 13% when S_b/σ_{ys} = 1. Furthermore, the elastic hoop stress solutions at the lower values of θ were larger with a maximum percentage difference of nearly 120% at θ = -85° when S_b/σ_{ys} = 1. Note that similar

observations were reported regarding friction in previous FE studies with the linear elastic material models [111 and 112]. However, the influence of friction was not the same when the material nonlinearity was included. For the high applied loadings, the elastic-plastic hoop stress values reached the same highest levels, which were approximately unity for both cases of friction (compare the closed symbols in figure 62(c and d). This is a consequence of local material yielding. An additional difference with the elastic model solutions was that friction increased the hoop stress results at the lower values of θ when S_b/σ_{ys} = 1.

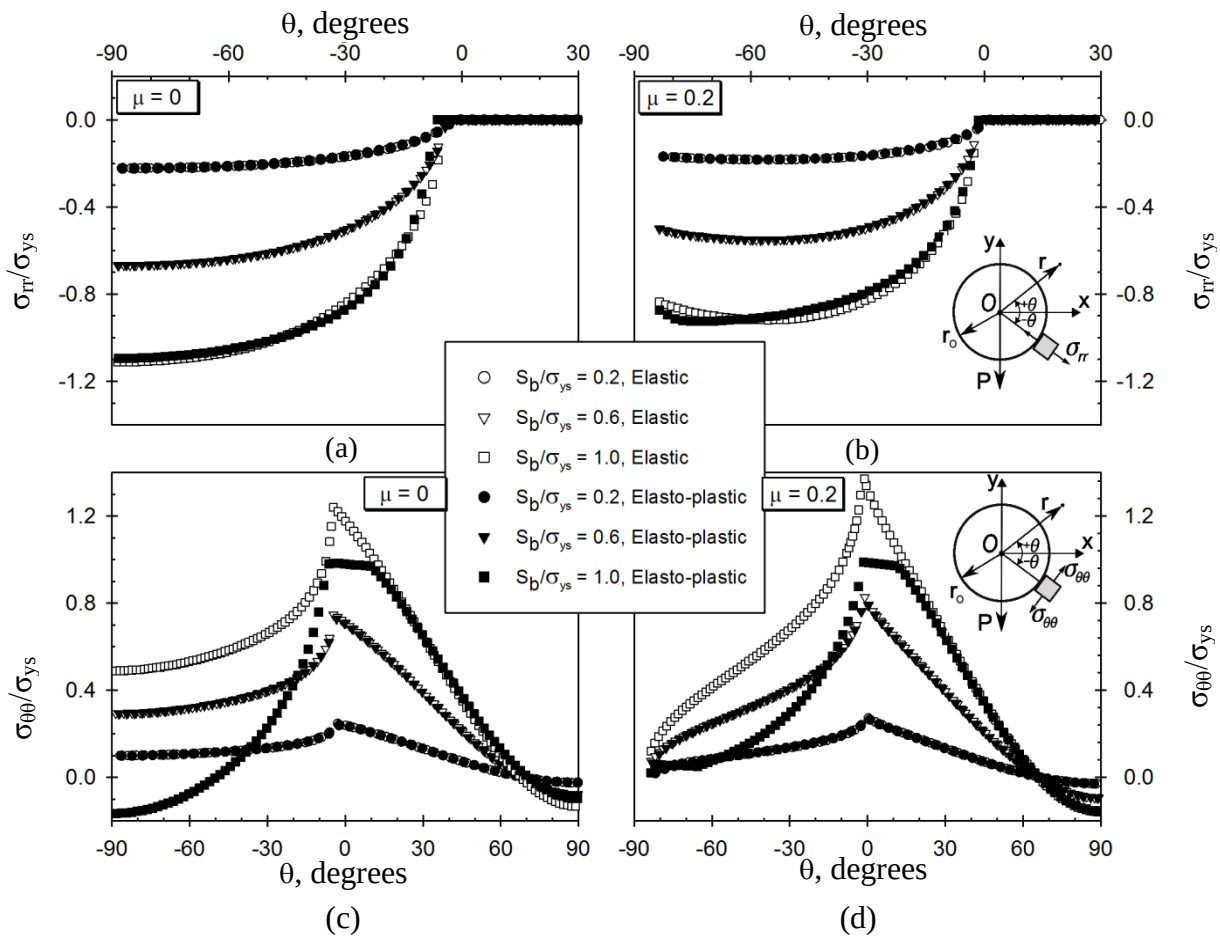

Figure 62. Hoop Stress Distributions Along the Hole Circumference From Elastic and Elastic-Plastic Models

The location of the maximum hoop stress caused concern because it is a susceptible region for crack initiation. For the elastic case, angles corresponding to the peak hoop stresses were approximately θ_{max} = -4.6° and -1.5° for μ = 0 and 0.2, respectively. These values were approximately θ_{max} = -3.6° and -1.0° for the elastic-plastic frictionless case and the case with μ = 0.2. However, when S_b/σ_{ys} = 1, the hoop stress values in the vicinity of these regions were approximately the same when material nonlinearity is included, indicating that the cracks may initiate at around θ = 0° (figure 62(c and d)).

Figures 63 and 64 show the results of the pin-loaded hole with an initial compressive residual stress field created by the CX simulation. In figure 63, the normalized radial stress distributions σ_{rr}/σ_{ys} are plotted along the circumference of the cold-expanded and pin-loaded hole with friction coefficients μ = 0 and 0.2. The radial stress solutions from kinematic- and isotropic-hardening material models were nearly identical. The stress and the influence of friction were very similar to that obtained from the elastic pin loading analyses (see figure 62(a and b)). For example, including friction reduced the radial stress magnitude by as much as 29% at around θ = 85° when the applied loading was S_b/σ_{ys} = 1.0.

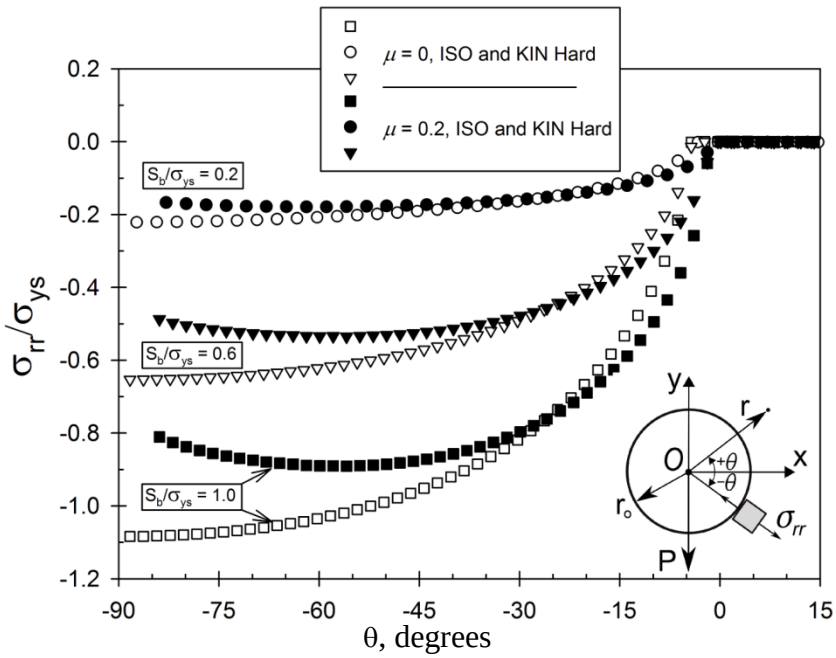

Figure 63. Radial Stress Distributions Along the Circumference of Cold-Expanded and Pin-Loaded Hole

Figure 64 shows the hoop stress distributions of the cold-expanded, pin-loaded hole for the isotropic and kinematic hardening material models for μ = 0 and 0.2. The results indicate that the hoop stress values were higher throughout the pin loading process when the kinematic hardening material model was used. That is because the compressive hoop stress magnitude produced from CX simulation was lower. Lower residual stress values in the kinematic hardening model result from Bauschinger's effect, in which the material more readily yields under reverse loading. It was observed that including friction raises the maximum hoop stress values in both hardening models and for all applied load levels up to S_b/σ_{ys} = 1. The locations of the maximum hoop stresses were approximately θ_{max} = -3.7° and -1.3° for μ = 0 and 0.2, respectively. These values were the same for both hardening models, as shown in figure 64(a and b).

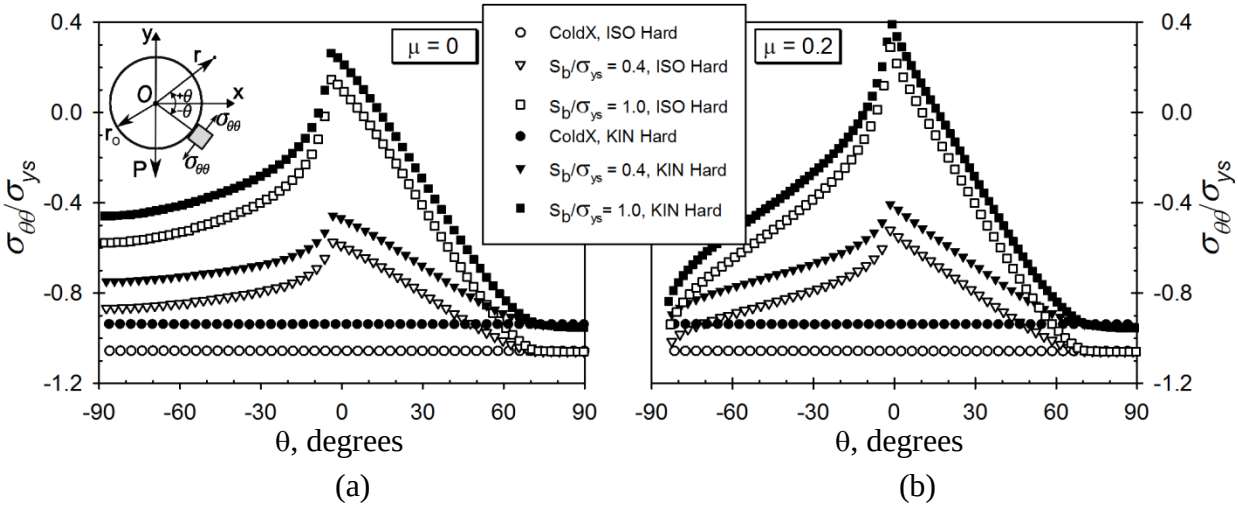

Figure 64. Hoop Stress Distributions Along the Circumference of the Cold-Expanded and Pin-Loaded Holes

Figure 65 shows the hoop stress distributions along the line $y = 0$, as a function of the normalized distance x/R, demonstrating the variation of the residual stress field in the sheet material as the pin load is applied. It was observed that the location of the maximum hoop stress was not at the hole edge, but in the interior region of the sheet material. At the highest load level (i.e., when $S_b/\sigma_{ys} = 1.0$), the hoop stress values for the kinematic hardening model at the hole edge (i.e., at $x/R = 1$) were $\sigma_{\theta\theta}/\sigma_{ys} = 0.23$ and 0.37 for $\mu = 0$ and 0.2. When the applied loading of $S_b/\sigma_{ys} = 1.0$ was removed, the residual stress curve returned to its original state with a negligible residual stress relaxation during the load cycle.

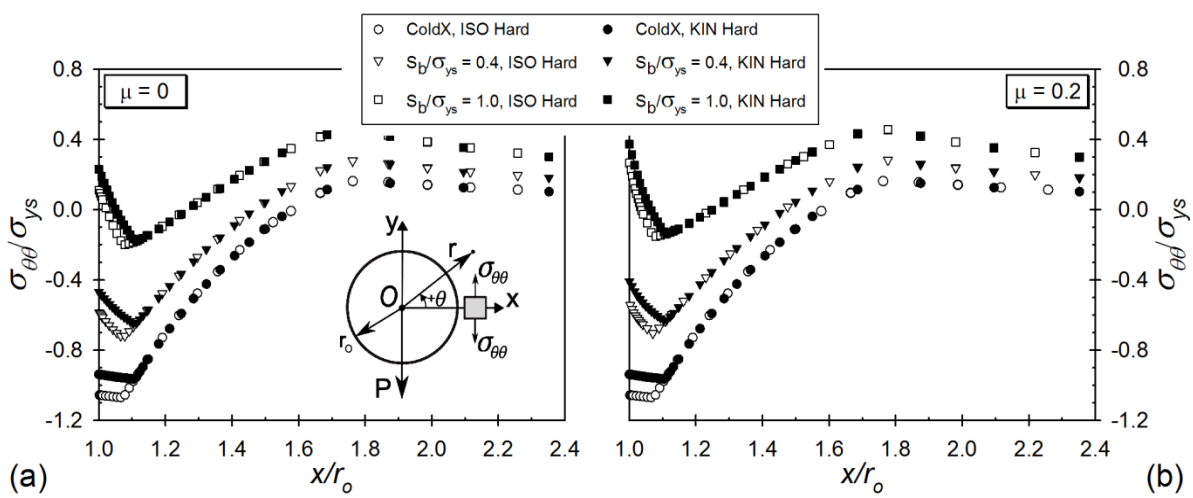

Figure 65. Hoop Stress Distributions Along the Line $y = 0$ Around the Cold-Expanded and Pin-Loaded Holes

6.2 THE SIFs FOR A SINGLE CRACK AT PIN-LOADED HOLE.

6.2.1 THE FE MODEL AND BCs.

Figure 66 shows a crack configuration for SIF computation; it is a 2D rectangular sheet with a single crack emanating from the cold-worked hole. The size of the thin rectangular sheet is 65.0 mm (*h*) by 44.45 mm (2*w*), with a 7.07-mm-diameter hole (2*r*) located at 22.23-mm distance (*d*) from the bottom edge. Two different loading cases were considered: (a) open hole in tension and (b) pin-loaded hole. In case (a), the sheet is loaded in tension with a normal traction applied on the bottom edge, while the sheet top edge is constrained in the vertical direction. For case (b), the hole is loaded by a neat-fit pin downward with a magnitude *P*. The sheet is constrained in the *y*-direction at the top edge (figure 67). The material properties given in section 6.1.2 were used for the 7075-T6 aluminum alloy sheet. The pin is assumed to be a rigid body.

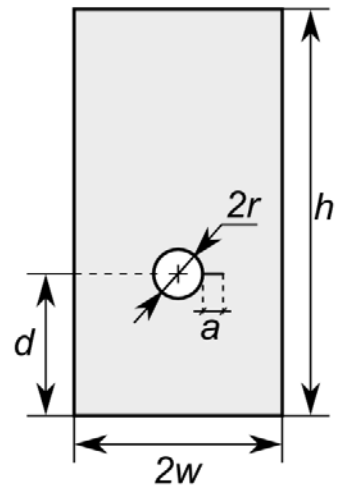

Figure 66. Sheet Configuration: *h* = 65.0 mm, 2*w* = 44.45 mm, 2*r* = 7.07 mm, and *d* = 22.23 mm

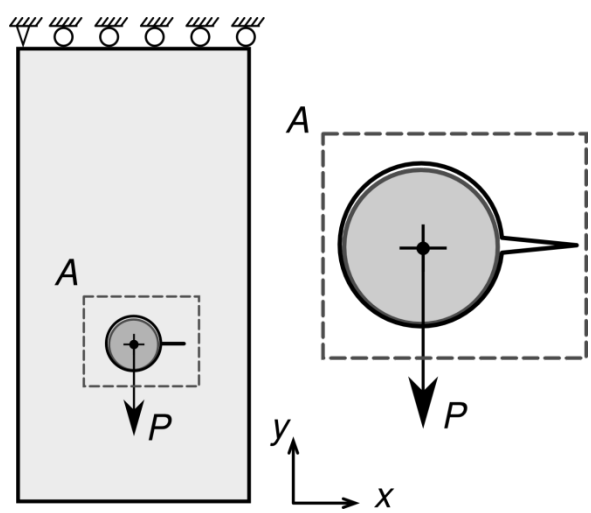

Figure 67. Case (b) Loading for Cracked Pin-Loaded Hole

6.2.2 METHODOLOGY.

Two different approaches were used to obtain mode I SIF solutions (K_I) for the loaded-hole configurations, which are: (a) J-integral approach and (b) weight function technique. K_I values were computed for normalized crack lengths from $(a+r)/w$ = 0.175 to 0.75.

First, an FE mesh was created with a multilinear elastic-plastic material definition for the 7075-T6 aluminum alloy with an isotropic hardening behavior. The model contained highly refined eight-node quadrilateral plane stress elements at the crack tip, as shown in figure 68. A residual stress field was obtained by uniformly expanding the hole of the sheet beyond the elastic limit of the material. Radial interferences considered during CX simulation were:

$$CW = \frac{\Delta r}{r}\% = 2\%,\ 3\%, \text{ and } 4\% \tag{22}$$

where Δr was the amount of radial hole expansion.

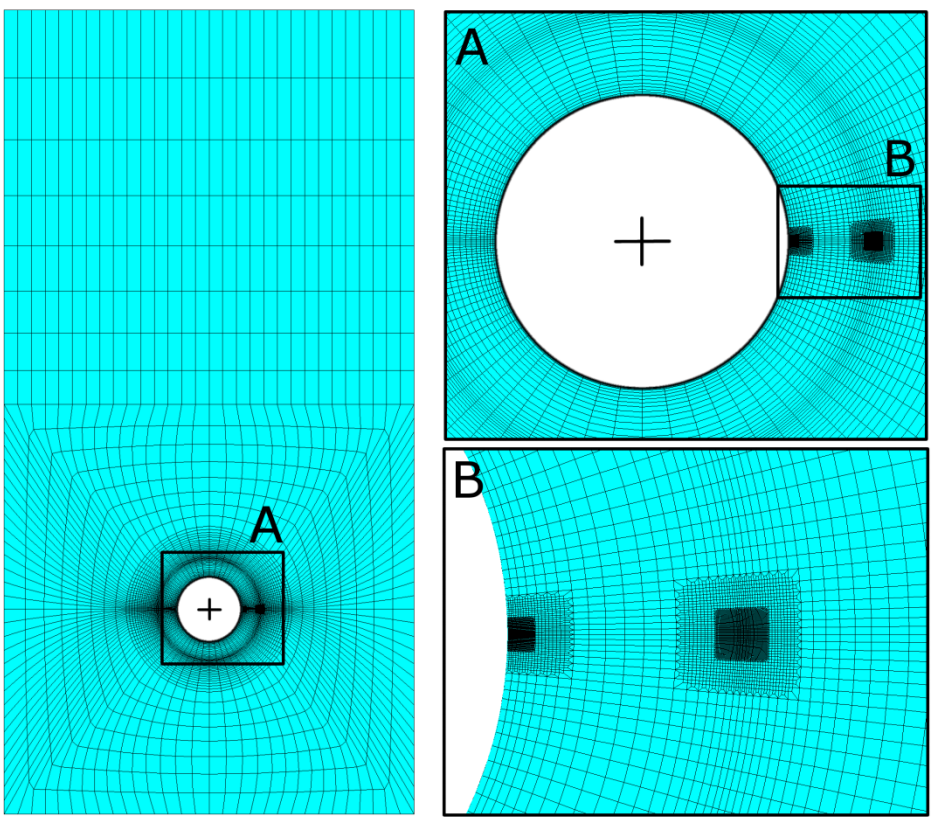

Figure 68. Sample FE Mesh for Cracked Pin-Loaded Hole With $(a+r)/w$ = 0.25

Next, the same meshed model was duplicated with purely elastic material properties. The residual stress field created in the elastic-plastic model was transferred to the elastic model via an ANSYS command INISTATE. The sheet was then loaded in tension and J-integral values were

computed for ten different contours around the crack tip. The mode I SIFs K_I were obtained from the average J-integral value, J_{ave}, using the relationship:

$$K_I = \sqrt{J_{ave} \cdot E} \tag{23}$$

Mode I SIFs K_I for the given crack configuration were also computed using the weight function along with the superposition principle. The weight function specific to a single crack from a hole in an infinite sheet can be expressed as in reference 61:

$$m(\alpha, \xi) = \frac{1}{\sqrt{2\pi a}} \sum_{i=1}^{3} \beta_i(a) \cdot \left(1 - \frac{\xi}{\alpha}\right)^{i-\frac{3}{2}} \tag{24}$$

provided that the crack length satisfies the conditions $a/r \leq 2$. In equation 24, ξ and α are nondimensional quantities $\alpha = a/r$ and $\xi = x/r$ (see figure 69).

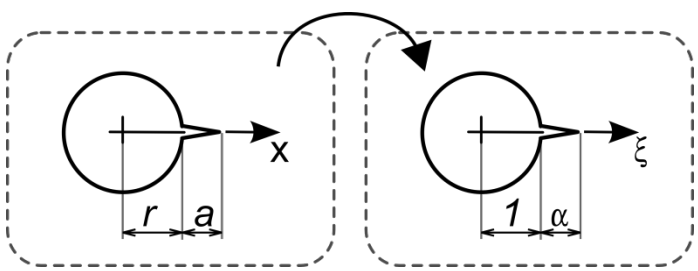

Figure 69. A Single Crack From a Hole in an Infinite Plate

Functions β_i are given by:

$$\begin{aligned} \beta_1(\alpha) &= 2.0 \\ \beta_2(\alpha) &= \left[4\alpha f_r'(\alpha) + 2 f_r(\alpha) + \frac{3}{2} F(\alpha)\right] / f_r(\alpha) \\ \beta_3(\alpha) &= \left[\alpha F'(\alpha) - \frac{1}{2} F(\alpha)\right] / f_r(\alpha) \end{aligned} \tag{25}$$

where

$$F(\alpha) = \left[\sqrt{2}\pi\varphi(\alpha) - 4E_1(\alpha) \cdot f_r(\alpha)\right] / E_2(\alpha) \tag{26}$$

The related functions $\phi(\alpha)$, $E_1(\alpha)$, and $f_r(\alpha)$ in equation 26 are given by:

$$\varphi(\alpha) = \frac{1}{\alpha^2}\int_0^{\alpha} s \cdot \left[f_r(\alpha) \right]^2 ds$$

$$E_j(\alpha) = \sum_{m=0}^{7} \left(\frac{2^{m+1} m! S_m \alpha^m}{\prod_{k=0}^{m} \left(1 + 2j + 2k\right)} \right) \tag{27}$$

$$f_r(\alpha) = 2.2421 - 2.8069\alpha + 4.1784\alpha^2 - 4.3940\alpha^3 + 2.9623\alpha^4 - 1.1899\alpha^5 + 0.2565\alpha^6 - 0.0227\alpha^7$$

and the coefficients S_m are:

S_m: 1.9991, -1.9543, 2.5773, -2.3769, 1.4367, -0.5393, 0.1066, -0.0089.

To obtain the K_I solutions via the weight function technique, the nodal stress distributions along the crack plane were first extracted from an uncracked loaded hole model in ANSYS. The portion of the SIF caused by the linear stress distribution over one element was then computed as follows:

$$\left(\Delta K_I\right)_i = \int_{\xi_{i-1}}^{\xi_i} \sigma_i(\xi) \cdot m(\alpha, \xi) d\xi \tag{28}$$

where $\sigma_i(\xi)$ is the linear stress distribution along the *i*th element (see figure 61), and $m(\alpha,\xi)$ is the weight function given in equation 23.

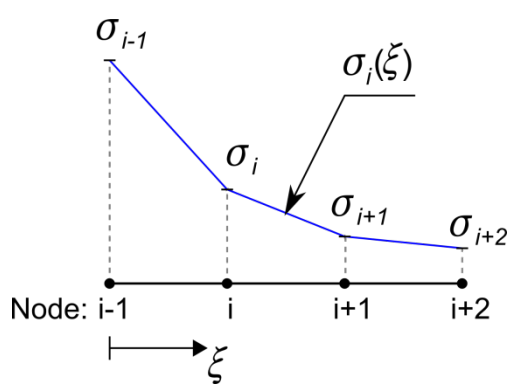

Figure 70. Nodal Contact Stresses

The summation of the ΔK_I for each element on the crack face gives the crack tip SIF K_I because of the corresponding applied pin load:

$$\left[K_I\right]_{inf} = \sum \Delta K_I \tag{29}$$

A correction factor can be incorporated into the $[K_I\,(a)]_{inf}$ solution to account for the effect of the finite width of the sheet as follows [63, 115]:

$$K_I(a) = f(a,w)\left[K_I(a)\right]_{inf} \tag{30}$$

$$f(a,w) = \sqrt{\frac{1}{cos\left(\frac{\pi(2r+a)}{2(2w-a)}\right)} \cdot \frac{sin\left(2\frac{2r+a}{2w-a}\cdot\frac{a}{w}\right)}{\left(2\frac{2r+a}{2w-a}\cdot\frac{a}{w}\right)}} \tag{31}$$

It must be noted that, because of the complex nature of the weight function, the expression in equation 28 could not be analytically integrated. Consequently, a numerical technique was adopted to perform the integration using Gauss-Chebyshev quadrature. This quadrature, as demonstrated by Daniewicz [116], conveniently circumvents the crack tip singularity associated with the weight functions.

Using the given weight function, the SIFs caused by the residual stress field alone, $K_{I.res}$, were computed from the residual stress distribution along the crack edge. Next, the same weight function was used to compute the applied $K_{I.app}$ from the stress distribution along the crack line due to applied remote loading. Finally, these two solutions were superposed with one another to give resulting K_I values for the cold-worked open and pin-loaded holes.

Finally, the boundary-correction factor F for the different crack length was computed by normalizing the K_I:

$$F = \frac{K_I(a)}{S\sqrt{\pi a}} \tag{32}$$

where S is the remote applied stress. The applied stress considered in this study was S = 300 MPa.

6.2.3 RESULTS.

Figure 71 shows the boundary correction factor solutions computed using the two different approaches described above for the cracks in an open hole with lengths from $(a+r)/w$ = 0.175 to 0.75. Symbols represent the J-integral method results, whereas the lines are the weight function solutions. The F values for the residual stress-free hole are also included in the figure for comparison. Note that the results from the weight function technique are given only for the

range 0.175 ≤ $(a+r)/w$ ≤ 0.45 because of the maximum crack length limitation a/r ≤ 2 for the weight function used in this analysis. Solutions from both the *J*-integral method and the weight function technique compare well. It is observed that cold working reduces boundary-correction factors by a significant amount when the crack length is small. The higher interference amount produces greater influence. However, this significant impact diminishes as the normalized crack length $(a+r)/w$ approaches 0.45, after which no influence of cold working is observed.

Figure 72 shows the boundary-correction factors *F* computed using the two different approaches for cracks in a pin-loaded hole with lengths from $(a+r)/w$ = 0.175 to 0.75. Again, the symbols represent the FE model results and the lines are the weight function solutions. The *F* values for the pin-loaded hole with no residual stress are also included in figure 72 for comparison. The solutions from both approaches compare well. The beneficial influence of the cold working process for the pin-loaded hole is evident for the range of normalized crack length $(a+r)/w$ < 0.40. The higher interference amount resulted in greater reduction in *F*. Similar to the open hole case, this impact diminished as the normalized crack length $(a+r)/w$ approached 0.40, after which no influence of cold working was detected.

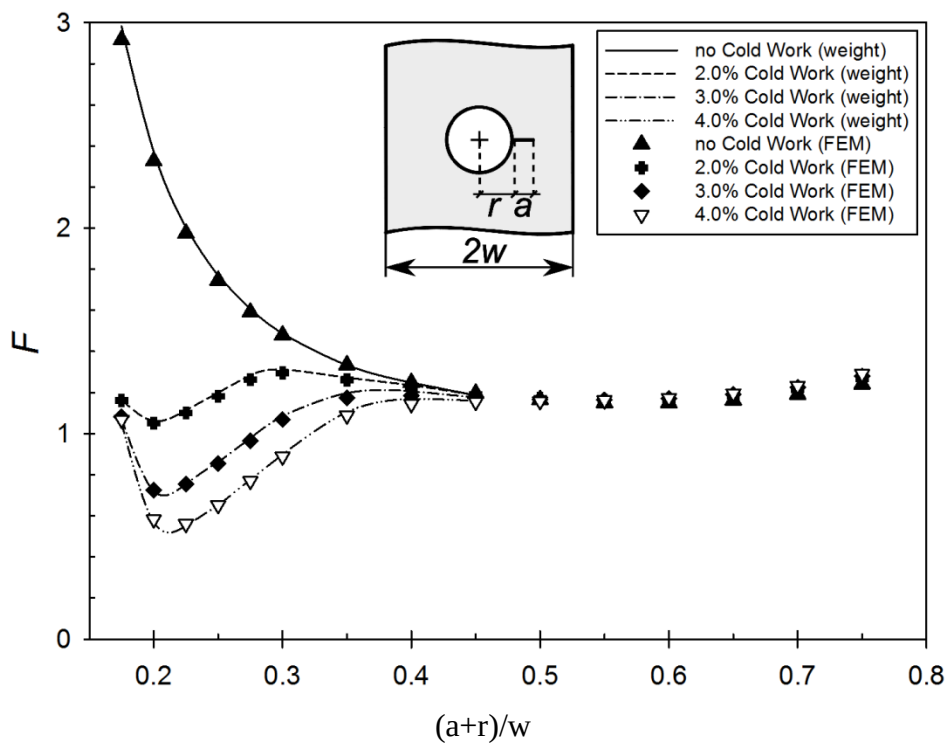

Figure 71. Boundary Correction Factors for a Single Crack From an Open Hole in a Finite Sheet Loaded in Tension

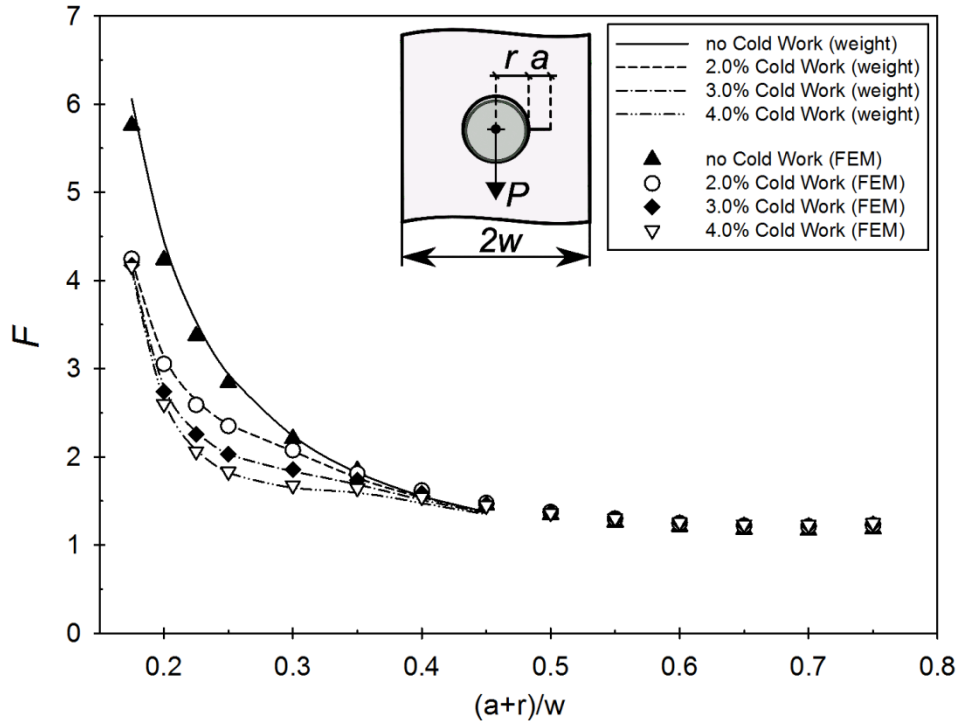

Figure 72. Boundary Correction Factors for a Single Crack From a Pin-Loaded Hole in a Finite Sheet

7. STRESS AND CRACK ANALYSES ON COLD-WORKED ROTORCRAFT COMPONENT.

7.1 CONFIGURATION.

Two-angle specimens connected via pins through eight different holes were loaded remotely in tension by grips, as shown in figure 73. The material used for the 2.4-mm-thick angles was 7075-T6511 aluminum alloy and the pins were made of steel. The width of one angle was larger than that of the other. Figure 74 shows the 2D drawings and dimensions of the small and large angles. All of the holes (except for one critical hole) were cold-worked with 5% radial interference. The critical hole was cold-worked to 3%. The initial diameter of the holes (reamed to a final size of d_f = 4.76 mm after the cold work) was d_o = 4.11 mm.

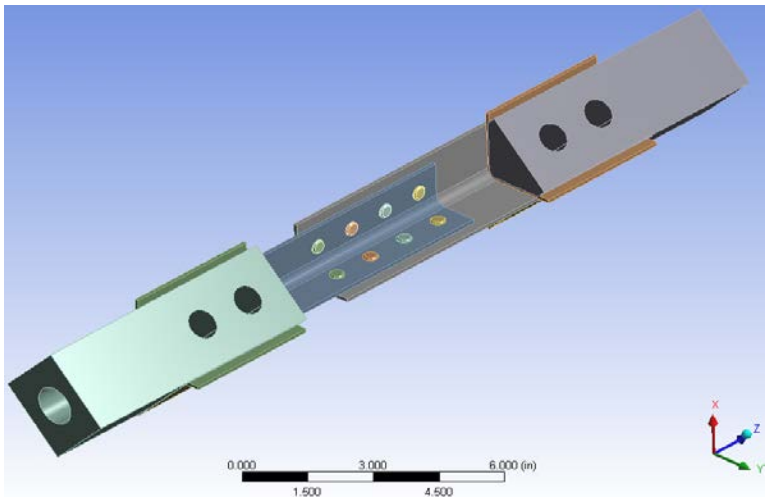

Figure 73. Nested Angle Joint Loaded in Tension

An elastic-plastic pin-loading analysis of non-cold-worked angles was performed in this study to determine the stress fields in the vicinity of the holes. Next, residual stress fields were introduced around the holes from cold working simulations. The produced residual stress fields were then transferred to a purely elastic model to perform pin loading simulations and obtain subsequent stress fields. A single crack was then inserted to one side of the critical hole to study its influence on load distributions to the neighboring holes.

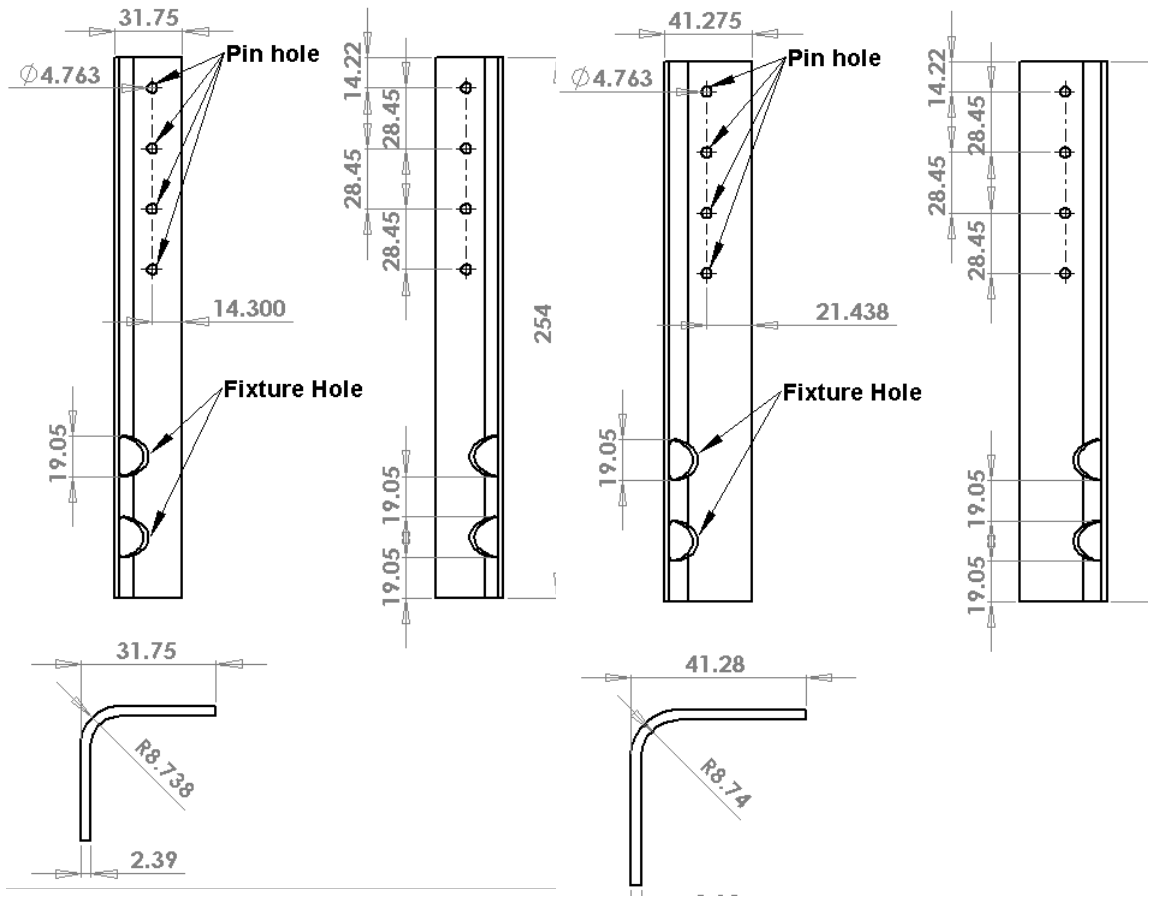

Figure 74. Drawings and Dimensions of Small (left) and Large (right) Angles (units in mm)

7.2 MATERIAL MODEL.

Figure 75 shows a multilinear stress-strain curve for extrusions with thicknesses of 12.7 mm–19 mm. Because the thickness of the angles was much smaller than the given range, the resulting curve [61] was adjusted down by 20.7 MPa (3 ksi) with the recommendation of ALCOA, Inc. The yield stress of the material σ_{ys} = 553.6 MPa was determined from the modified curve. The modulus of elasticity and the Poisson's ratio are E = 71.6 GPa and ν = 0.33, respectively. These material properties, along with the modified multilinear stress-strain curve, were used for the material model. The steel pins were assumed to be purely elastic with E = 200 GPa and ν = 0.3.

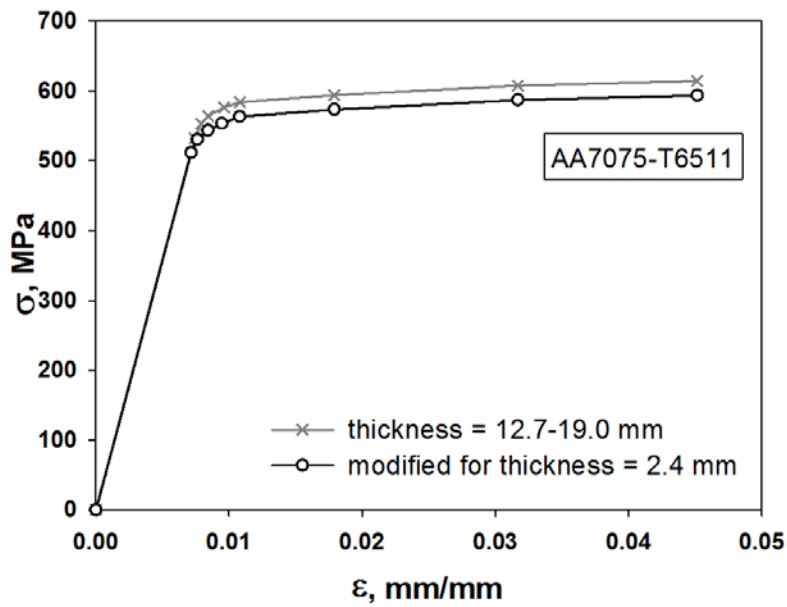

Figure 75. Stress-Strain Curve for 7075-T6511 Aluminum Alloy

7.3 THE FE MODEL AND BCs.

ANSYS Workbench™ 12.0 was used to perform the 3D stress analysis. Figure 76 shows the 3D model, along with the hole labels and applied BCs. It should be noted that the clamped ends are removed to reduce the model size and to avoid complex BCs. Also, preliminary results showed that the *Y*-displacements at the boundaries of the clamped regions shown were reasonably uniform. Therefore, the model was loaded by applying uniform displacement loads at the remote end of angle 2, while constraining the other end of angle 1, as shown in figure 76. A maximum applied displacement of v_{max} = -1 mm created nearly 53 kN reaction force at the remote end of each angle.

It should be noted that the longitudinal symmetry could not be used because of the single critical hole (hole d1) that was cold-worked to a different amount than all others. However, for the stress analysis with non-cold-worked holes, cutting the model longitudinally into two equal sides simplified it even further; the symmetry BCs could then be used across the cut surface.

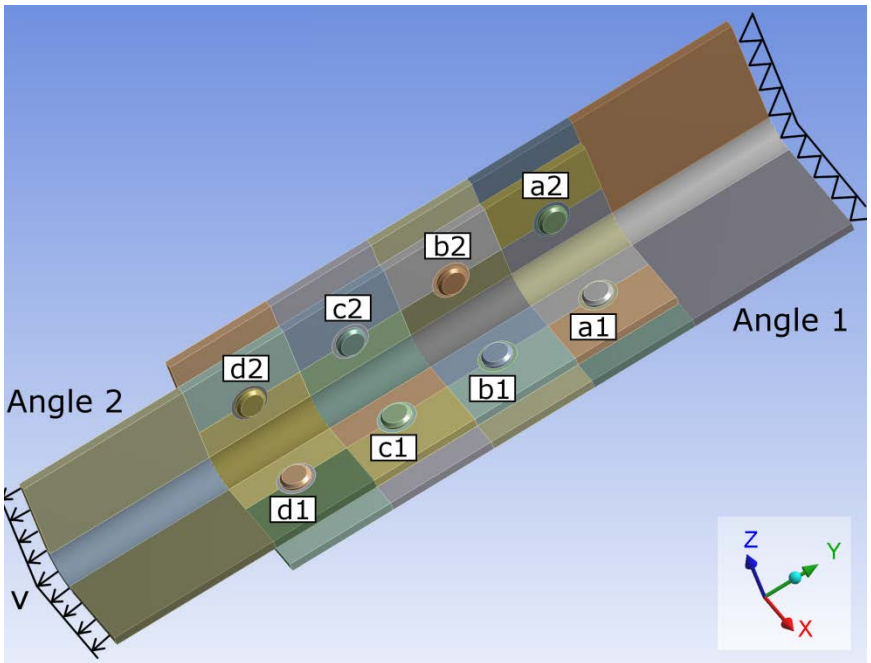

Figure 76. The 3D Model of Pin-Joint Component

Figure 77 shows the FE mesh of the 3D model. The sweep meshing feature of ANSYS was used along with face-mapped meshing to gain a better control of the regions in the vicinity of the pinholes. Six element layers were used along the thickness direction of the angles. A typical FE mesh, including pins and contact regions, consists of nearly 160K elements and 110K nodes. Appropriate contact elements were used at the interfaces between the angles and the pins. A friction coefficient of $\mu = 0.2$ was prescribed between the pins and the holes. All other contacts were assumed frictionless.

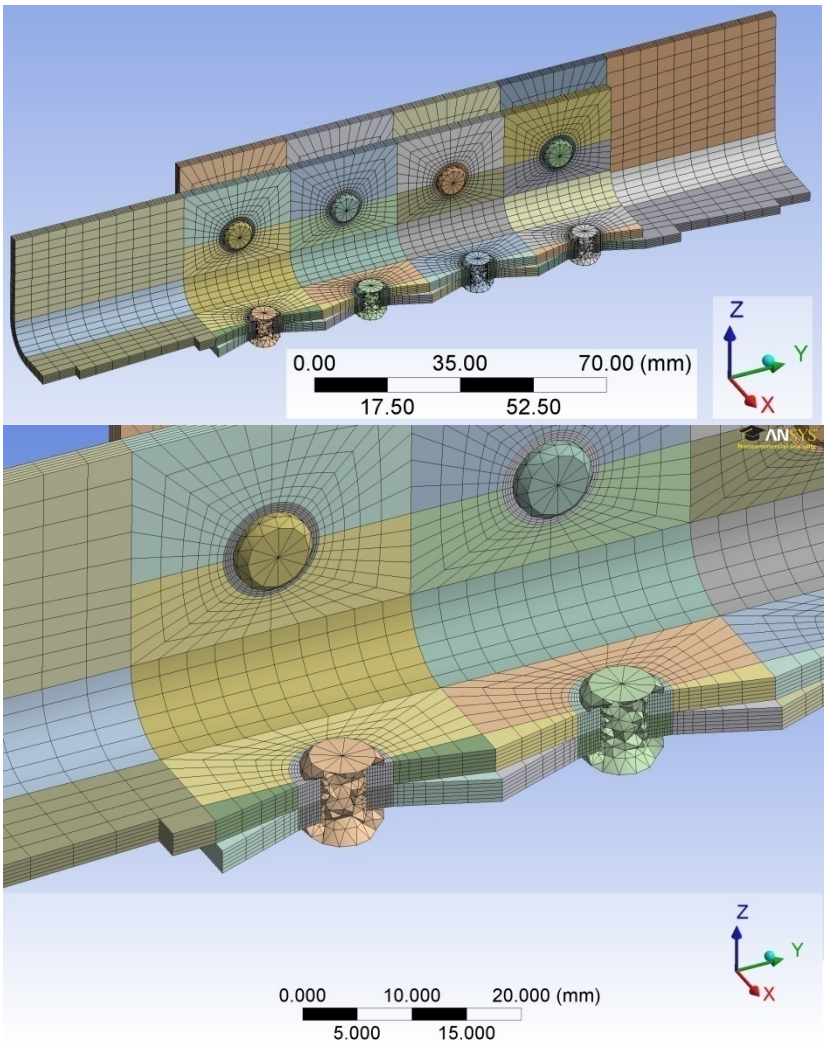

Figure 77. The FE Mesh of the Nested Angle Model

Residual stresses from cold working were created by uniformly expanding the holes of the angles to the corresponding interference amounts. A subsequent reaming simulation was performed by deactivating a few layers of elements around the hole surface. The obtained residual stress fields were then exported to an elastic model for subsequent pinload analysis. This separate model was used for pinloading study because the inclusion of all three processes (cold working, reaming, and pin loading) made modeling overly complicated.

In the final stage, a single crack was inserted into one side of the critical hole (d1) of angle 2 to study its influence on load distributions to the neighboring holes (see figures 76 and 78). Material models for the 7075-T6511 aluminum alloy angles and the steel pins were linear elastic for simplicity. Residual stresses from cold working were not considered in this stage. The model was loaded by applying uniform remote displacements with v_{max} = -1 mm, as described in this section.

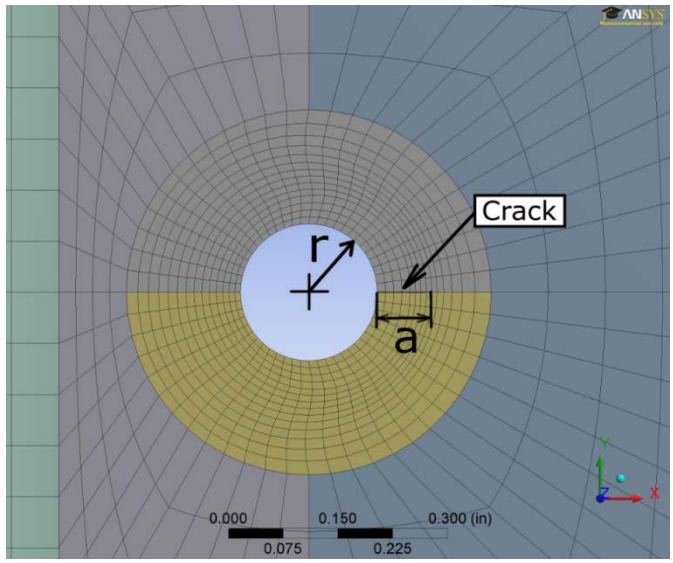

Figure 78. Orientation of the Crack Around Hole d1

7.4 RESULTS.

Figure 79 shows circumferential stress distributions in the vicinity of holes a, b, c, and d (indicated in figure 76) at three different through-thickness locations of each angle: (1) back face (or outer face), (2) mid-thickness, and (3) front face (or inner face). The applied uniform displacement load shown in figure 76 is v = -1 mm (or nearly 53 kN). Note that hole a refers to both a1 and a2 because the stress fields around these two holes are the same due to symmetry. This applies to holes b, c, and d as well. In figure 79(a through d), the normalized hoop stresses ($\sigma_{\theta\theta}/\sigma_{ys}$) along the line perpendicular to the applied loading are plotted versus the distance from the hole center normalized by the radius of the hole (x/r).

First, it is important to consider the variation in stress distributions within angles 1 and 2 around each hole. At hole a (figure 79(a)), the stress distributions in angle 1 are significantly higher than those in angle 2. At hole b (figure 79(b)), the stress curves within two different angles are approximately equal, whereas at holes c and d (figure 79(c and d)), the normalized stresses within angle 2 show much higher values than those in angle 1. Thus, in general, angles 1 and 2 at the same pin joint experience different stress levels.

Next, the through-thickness variation in stress distributions within each angle must be considered. Nearly uniform stress levels are achieved in each angle material, except in the regions near the hole surfaces and in angle 2 around hole a, as well as in angle 1 around hole d. Uniformity of the though-thickness stress distributions may indicate that the sheet-bending effects are negligible in those regions.

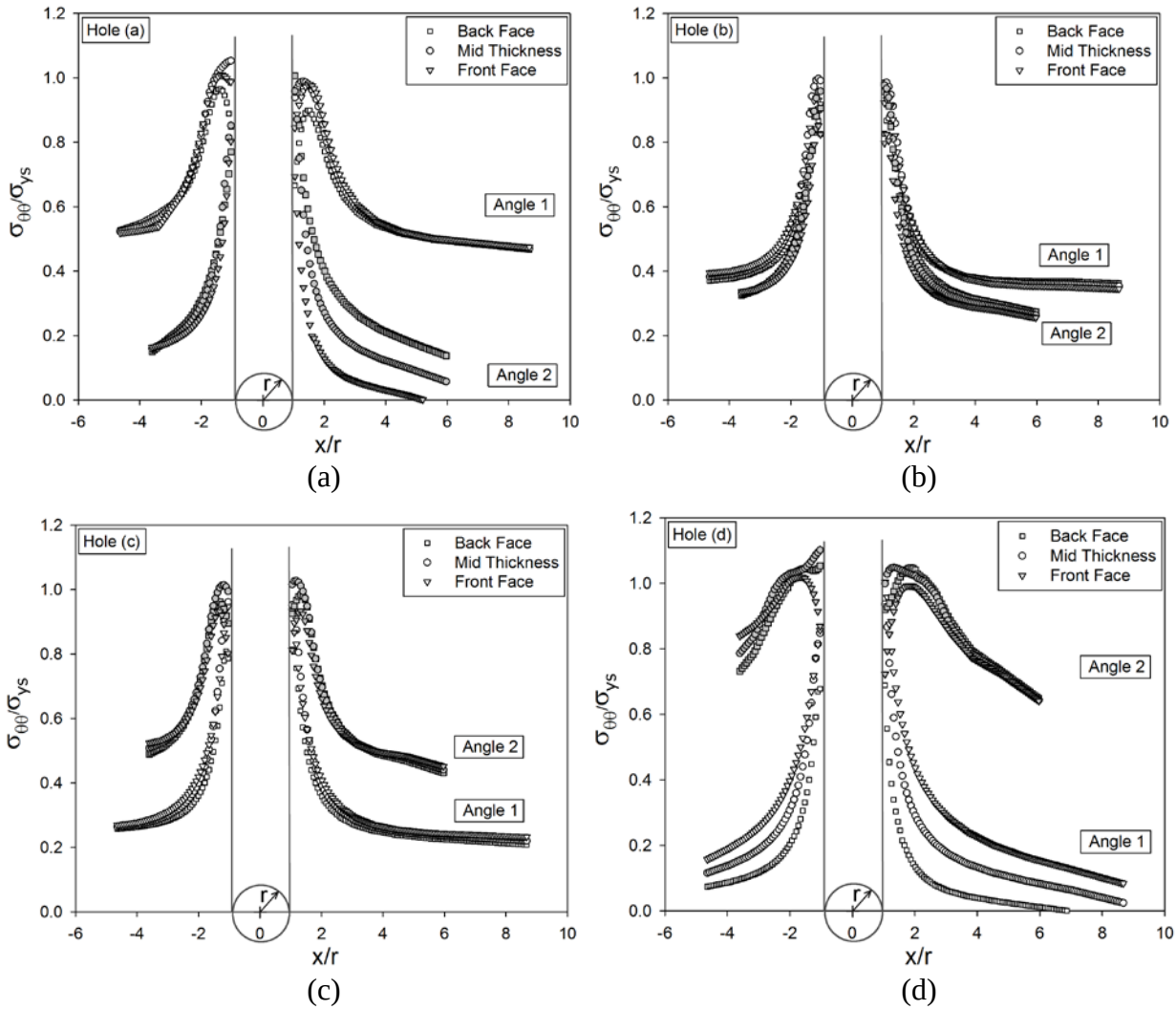

Figure 79. Hoop Stress Distributions Around Holes

Finally, the variation in the stress distributions around different holes within the same angle must be evaluated. It may be observed that the circumferential stress distributions in angle 1 start with the highest values around hole a and decrease toward hole d. On the other hand, the stress levels in angle 2 start with the highest values around hole d and decrease toward hole a. In other words, coming from the clamped region within each angle, the first hole encountered experiences the highest stress levels. This is because the two holes have to resist the greatest number of bypass loads. Hole d of angle 2 is shown to be a critical hole because of the highest overall stress levels around it.

Figure 80 shows subsequent stress distributions in the vicinity of critical hole d1 after the cold-worked angles are pin-loaded to different levels using a purely elastic material model. The stress results are given at three through-thickness locations for each angle: (1) back face (or outer face), (2) front face (or inner face), and (3) mid-thickness. In each figure, the circumferential normalized stresses ($\sigma_{\theta\theta}/\sigma_o$) are plotted along the lines perpendicular to the applied loading versus the normalized distance from the hole center (x/r). Because of the model size limitation

in ANSYS with academic license only, a two-level convergence study was performed to verify these solutions. The stress solutions from the two FE models with four and six element layers across the angle thickness compared well.

The solid circles in figure 80 correspond to the residual stress distribution obtained by cold-expanding the critical hole with 3% radial interference and reaming it to a final size. It can be observed that the back face of angle 2 experiences the highest stress levels at the hole edge for any applied loading when compared with the other two locations. However, the hoop stresses at the hole surface of the back face (figure 80(c)) and the mid-thickness (figure 80(b)) show unrealistically high values for the remote displacement load of v = -1.0 mm because of the elastic material model that was used for angles in the pin loading analysis. This information indicates that the critical hole d1 undergoes plastic deformation at this load level.

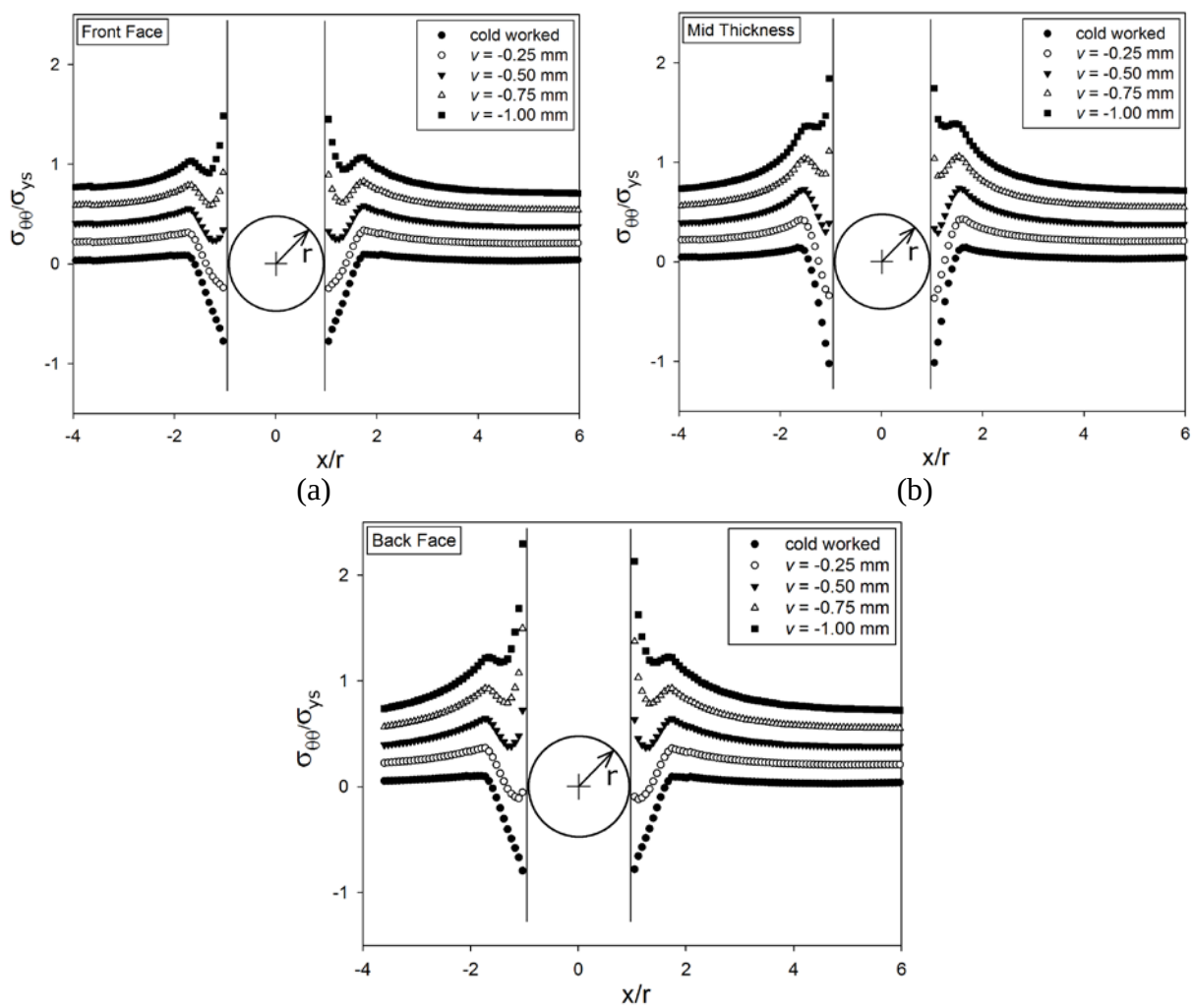

Figure 80. Circumferential Stress Distributions Around Hole d1 in Angle 2 at: (a) Front Face, (b) Mid-Thickness, and (c) Back Face

Finally, figure 81 presents subsequent load distributions to the eight holes in each angle when: (a) there is no crack, (b) a crack with normalized length $(a+r)/r$ = 1.4 is inserted into the critical hole d1, and (c) a crack with $(a+r)/r$ = 1.8 is inserted into the critical hole d1. Here, a is the crack length as shown in figure 78. In each plot, the fraction of the total load is plotted versus the hole designation shown in figure 76. Figure 81(a) shows that holes d1 and d2 use the biggest portion (17%) and holes b1 and b2 use the smallest portion (9%) of the applied remote load. The load distribution does not change significantly when cracks of different sizes are included in the model (figure 81(c and d). For example, including a crack of $(a+r)/r$ = 1.8 increased the load share of holes a2, b1, and b2 by only 1%, whereas it reduced the load share at hole d1 by 1%. Because these are insignificant changes, it was concluded that the presence of a single side crack with lengths up to 80% of the hole radius does not affect the load distributions to the remaining holes.

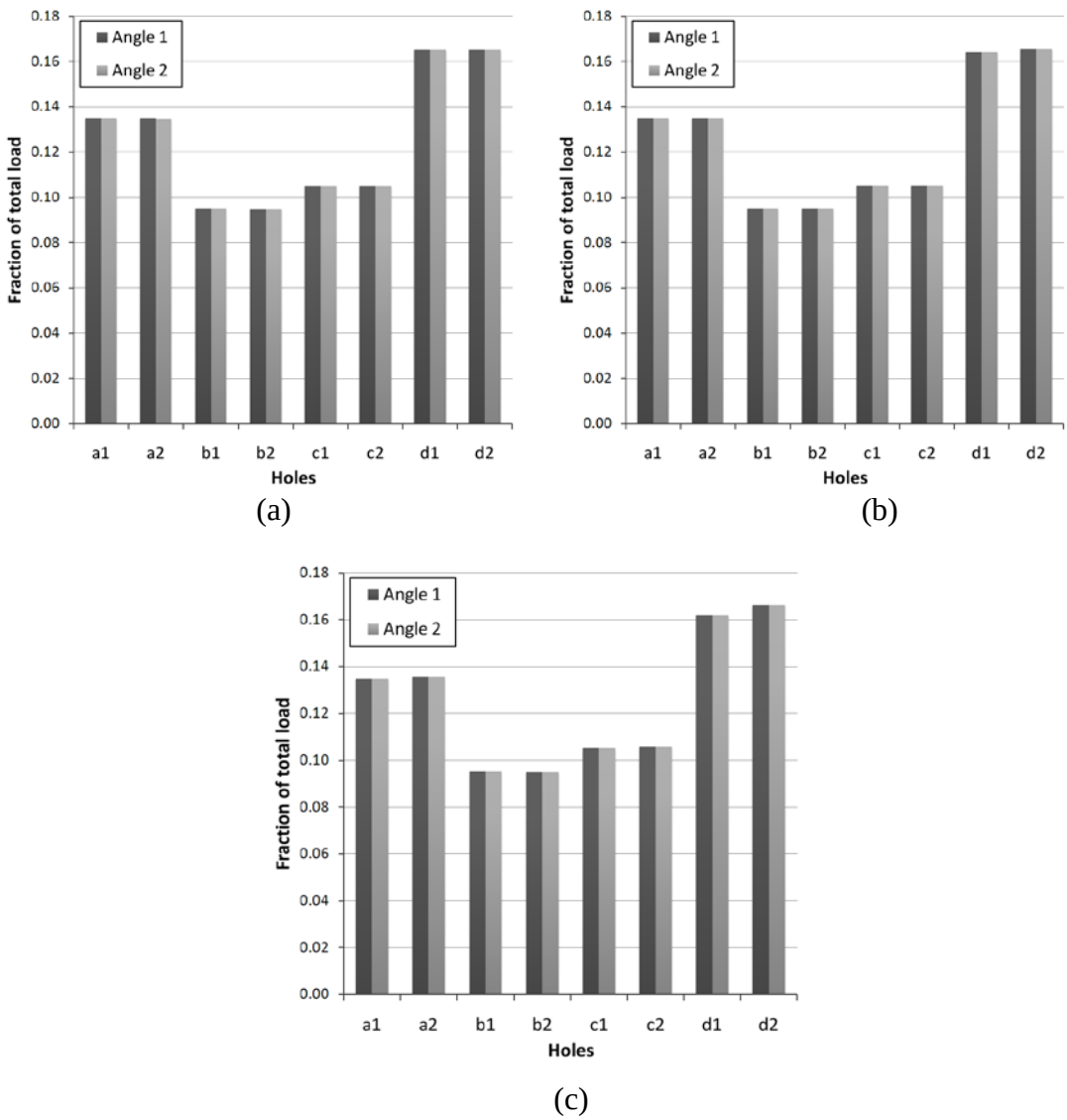

Figure 81. Load Distributions to Each Hole: (a) No Crack, (b) $(a+r)/r$ = 1.4, and (c) $(a+r)/r$ = 1.8

8. CONCLUSION.

Finite element and numerical studies were performed to develop the stress states on tests conducted to study crack growth in residual stress-bearing structural details and materials typical of rotorcraft structures. Companion analyses were also developed to assess the accuracy of typical fatigue crack growth models using either linear superposition or a nonlinear method. In another part of the Federal Aviation Administration-sponsored project, fatigue crack growth tests were carried out on a range of specimens that progressed from very simple to fairly complex. The specimen geometries were one-dimensional (1D) cracks in standard compact specimen (C(T)) specimens, 1D- and two-dimensional (2D) cracks in specimens with open holes, 1D cracks in specimens with pin-loaded holes, and 2D cracks at fastener holes in nested angle specimens with a lap shear joint. Most test series were performed under constant-amplitude cyclic loading, but additional tests of pin-loaded hole and nested angle specimens were performed under variable-amplitude loading. Each test series used a number of identical specimens (replicate tests), as well as specimens in at least two material conditions: (1) as-machined condition (without residual stress) and (2) residual stress-bearing condition. Tests on the C(T) specimens had residual stress induced by laser shock peening and all other tests had residual stress induced by cold hole expansion. Replicate tests provided measures of variability in residual stress and fatigue crack growth. Companion linear elastic fracture mechanics analyses were performed to develop the Green's function (GF) for the C(T) specimen and to develop a linear superposition life prediction code.

Crack growth analyses were performed on the laser shock-peened C(T) specimens and the cold-worked, open-hole specimens using linear superposition, while a nonlinear method was also applied to the cold-worked hole specimens. Using the measured residual stresses, the linear superposition method greatly overestimated crack growth lives in the C(T) specimens, whereas using the residual stress intensity factors computed from either a weight function or GF method fell short of the test data. The 3D elastic-plastic finite element analyses (FEA) were performed on the cold-worked hole process to generate the residual stress distributions used in the linear-superposition method. Crack growth lives predicted using the nonlinear method agreed fairly well with the test data. In addition, an elastic-plastic 2D FEA was performed on the pin-loaded and cold-worked hole configuration. Finally, FEAs were also conducted on the nested angle components under typical cold-worked hole conditions.

9. REFERENCES.

1. Stephens, R.I., Fatemi, A., Stephens, R.R., and Fuchs, H.O., *Metal Fatigue in Engineering*, John Wiley & Sons, New York, New York, 2001.

2. Ozdemir, A.T., Cook, R., and Edwards, L., "Residual Stress Distributions around Cold Expanded Holes," *International Congress on Aeronautical Fatigue (ICAF) Symposium*, Stockholm, Sweden, 1993.

3. "Shot Peening," Metal Improvement Company, Curtis-Wright Corporation, 2006, http:// www.metalimprovement.com

4. Schiffner, K. and Helling, C.D., "Simulation of Residual Stresses by Shot Peening," *Computers and Structures*, Vol. 72, 1999, pp. 329-340.

5. Frija, M., Hassine T., Fathallah, R., Bouraoui, C., and Dogui, A., "Finite Element Modeling of Shot Peening Process: Prediction of the Compressive Residual Stresses, the Plastic Deformations and the Surface Integrity," *Materials Science and Engineering: A*, Vol. 426, 2006, pp. 173-180.

6. Bonner, N.W., Wimpory, R.C., Webster, G.A., Fry, A.T., and Kandil, F.A., "Measurement of Residual Stress Through a Shot Peened Surface Subjected to Successive Material Removal," *Material Science Forum*, Vol. 404, 2002, pp. 653-658.

7. Terasaki, T., Chen, J., Akiyama, T., and Kishitake, K., "Non-Destructive Method for Estimating Residual Stress Distribution in Component Due to Shot Peening," *JSME Journal*, Vol. 42, No. 2, 1999, pp. 216-223.

8. El Tobgy, M.S., Ng, E., and Elbestawi, M.A. "Three-Dimensional Elastoplastic Finite Element Model for Residual Stresses in the Shot Peening Process," Proceedings of the Institution of Mechanical Engineers, *Journal of Engineering Manufacture*, 2004, Vol. 218, pp. 1471-1481.

9. Meguid, S.A., Shagal, G., Stranart, J.C., and Daly, J., "Three-Dimensional Dynamic Finite Element Analysis of Shot-Peening Induced Residual Stresses," *Finite Element Analysis and Design*, 1999, Vol. 31, pp. 179-191.

10. Al-Hassani, S., "Mechanical Aspects of Residual Stress Development in Shot Peening," *Proceedings of the First International Conference on Shot Peening*, Paris, France, 1981, pp. 583-602.

11. Shen, S. and Atluri, S.N., "An Analytical Model for Shot-Peening Induced Residual Stresses," *Computers, Materials and Continua*, 2006, Vol. 4, No. 2, pp. 75-85.

12. Baragetti, S. and Terranova, A., "Non-Dimensional Analysis of Shot Peening by Means of Design of Experiments," *International Journal of Materials and Product Technology*, Vol. 15, No. 1/2, 2000, pp. 131-141.

13. Meo, M. and Vignevic, R., "Finite Element Analysis of Residual Stress Induced by Shot Peening Process," *Advances in Engineering Software*, Vol. 34, 2003, pp. 569-575.

14. "Laser Peening Process," LSP Technologies, Inc., 2006 <http://www.lspt.com/process .asp>

15. Hackel, L.A., "Use of Laser Peening to Enhance Fatigue Life of Aircraft Structures and Turbine Engine Components," *Metal Improvement World*, Vol. 2, 2006, pp. 2-5.

16. Braisted, W. and Brockman, R., "Finite Element Simulation of Laser Shock Peening," *International Journal of Fatigue*, 1999, Vol. 21, pp. 719-724.

17. Ding, K. and L. Ye., "Three-Dimensional Dynamic Finite Element Analysis of Multiple Laser Shock Peening Processes," *Surface Engineering*, Vol. 19, No. 5, 2003, pp. 351-358.

18. Ballard, P., "Residual Stresses Induced by Rapid Impact-Applications of Laser Shocking," Ph.D. Thesis, 1991, Ecole Polytechnique, France.

19. Montross, C.S., Wei, T., Ye, L., Clark, G., and Mai, Y., "Laser Shock Processing and its Effects on Microstructure and Properties of Metal Alloys: A Review," *International Journal of Fatigue*, Vol. 24, 2002, pp. 1021-1036.

20. Ding, K. and L. Ye., "FEM Simulation of Two Sided Laser Shock Peening of Thick Sections of Ti-6Al-4V Alloy," *Surface Engineering*, Vol. 19, No. 2, 2003, pp. 127-133.

21. "FTI Cold Expansion Process," Fatigue Technology Inc., December 2006, <http://www. fatiguetech.com/coldEX_Split_sleeve.html>

22. Ball, D.L., "Elastic-Plastic Stress Analysis of Cold Expanded Fastener Holes," *Fatigue and Fracture of Engineering Materials and Structures*, Vol. 18, No. 1, 1995, pp. 47-63.

23. Priest, M., Poussard, C.G., Pavier, M.J., and Smith, D.J., "An Assessment of Residual-Stress Measurements Around Cold-Worked Holes," *Experimental Mechanics*, Vol. 361, 1995, pp. 361-366.

24. De Matos, P.F., Moreira, P.M., Camanho, P.P., and de Castro, P.M., "Numerical Simulation of Cold Working of Rivet Holes," *Finite Element Analysis and Design*, Vol. 41, 2005, pp. 989-1007.

25. Kang, J., Johnson, W.S., and Clark, D.A., "Three-Dimensional Finite Element Analysis of the Cold Expansion of Fastener Holes in Two Aluminum Alloys," *Journal of Engineering Materials and Technology*, Vol. 124, 2002, pp. 140-145.

26. De Matos, P.F., "The Influence of Residual Stresses on the Fatigue Behavior of 2024-T3 Al Specimens," Thesis, 2003, Universidade do Porto.

27. Kim, C., Kimb, D., Seok, C., and Yang, W., "Finite Element Analysis of the Residual Stress by Cold Expansion Method Under the Influence of Adjacent Holes," *Journal of Material Processing Technology*, Vol. 153, 2004, pp. 986-991.

28. Wang, Z. and Zhang, X., "Predicting Fatigue Crack Growth Life for Cold-Worked Holes Based on Existing Closed-Form Residual Stress Models," *International Journal of Fatigue*, Vol. 25, 2003, pp. 1285-1291.

29. De Matos, P.F., Moreira, P.M., Pina, J.C., Dias, A.M., and de Castro, P.M., "Residual Stress Effect on Fatigue Striation Spacing in a Cold-Worked Rivet Hole," *Theoretical and Applied Fracture Mechanics*, Vol. 42, 2004, pp. 139-148.

30. "Force-Mate Aerospace Bushing Installation," Fatigue Technology Inc., 2006, <http://www.fatiguetech.com/bushings_forcemate.html>

31. Pipkins, D.S., "Assessment of Effectiveness of Permanently Installed Cold Expanded Bushings in Fastener Holes Near Free Edges of Aluminum Panels," *Third Joint FAA/DoD/NASA Conference on Aging Aircraft*, 1999, Albuquerque, NM.

32. Lanciotti, A., Nigro, F., and Polese, C., "Fatigue Crack Propagation in the Wing to Fuselage Connection of the New Trainer Aircraft M346," *Fatigue and Fracture of Engineering Materials and Structures*, Vol. 29, 2006, pp. 1000-1009.

33. "NASGRO Reference Manual," Version 4.02, NASA Johnson Space Center and Southwest Research Institute, 2002.

34. United States Department of Defense, MIL-HDBK-5H: "Metallic Materials and Elements for Aerospace Vehicle Structures," 1998, pp. 3-71.

35. Newman, J.C., Jr., "Effects of Constraint on Crack Growth Under Aircraft Spectrum Loading," *Fatigue of Aircraft Materials*, Delft, The Netherlands, Delft University Press, 1992, pp. 83-109.

36. Newman, J.C., Jr., Wu, X.R., Venneri, S.L., and Li, C.G., "Small-Crack Effects in High-Strength Aluminum Alloys—A NASA/CAE Cooperative Program," NASA RP-1309, May 1994.

37. Hudson, C.M., "Effect of Stress Ratio on Fatigue-Crack Growth in 7075-T6 and 2024-T3 Aluminum Alloy Specimens," NASA TN D-5390, August 1969.

38. Yoder, G.R., Cooley, L.A., and Crooker, T.W., "On Microstructural Control on Near-Threshold Fatigue Crack Growth in 7000-Series Aluminum Alloys," *Scripta Metallurgica*, Vol. 16, 1982, pp. 1021-1025.

39. Piascik, R.S. and Gangloff, R.P., "Environmental Fatigue of an Al-Li-Cu Alloy: Part II. Microscopic Hydrogen Cracking Processes," *Metallurgical Transactions*, Vol. 24A, 1993, pp. 2751-2762.

40. Underwood, J.H., Pook, L.P., and Sharples, J.K., "Fatigue-Crack Propagation Through a Measured Residual Stress Field in Alloy Steel," *Flaw Growth and Fracture, ASTM STP 631*, American Society for Testing and Materials, 1977, pp. 402-415.

41. Fukuda, S. and Tsuruta, Y., "An Experimental Study of Redistribution of Welding Residual Stress," *Transactions of JWRI*, Vol. 7, 1978, p. 67.

42. Chandawanich, N. and Sharpe, W.N. Jr., "An Experimental Study of Fatigue Crack Initiation and Growth from Coldworked Holes," *Engineering Fracture Mechanics*, Vol. 11, 1979, pp. 609-620.

43. Nelson, D.V., "Effects of Residual Stress on Fatigue Crack Propagation," *Residual Stress Effects in Fatigue, ASTM STP 776*, American Society for Testing and Materials, 1982, pp. 172-194.

44. Lam, Y.C. and Lian, K.S., "Effect of Residual Stress and Its Redistribution on Fatigue Crack Growth," *Theoretical Applied Fracture Mechanics*, Vol. 12, No. 1, 1989, pp. 59-66.

45. Wilks, M.D.B., Nowell, D., and Hills, D.A., "The Evaluation of Stress Intensity Factors for Plane Cracks in Residual Stress Fields," *Journal of Strain Analysis*, Vol. 28, No. 3, 1993, pp. 145.

46. Kiciak, A., Glinka, G., and Burns, D.J., "Analysis of Fatigue Growth of Semi-Elliptical Cracks Through Residual Stress Fields," *Proceedings of 6th International Fatigue Congress (Fatigue 96)*, G. Lüjenry and H. Nowack, Pergamon Press, Tarrytown, New York, Vol. II, 1996, pp. 1207-1212.

47. Lee, Y., Chung, C., Park, Y., and Kim, H., "Effects of Redistributing Residual Stress on the Fatigue Behavior of SS330 Weldment," *International Journal of Fatigue*, Vol. 20, No. 8, 1998, pp. 565-573.

48. Parker, A.P., "Stress-Intensity Factors, Crack Profiles, and Fatigue Crack Growth Rates in Residual Stress Fields," *Residual Stress Effects in Fatigue, ASTM STP 776*, American Society for Testing and Materials, 1982, pp. 13-31.

49. Todoroki, A. and Kobayashi, H., "Prediction of Fatigue Crack Growth Rate in Residual Stress Fields," *Key Engineering Materials, Fracture and Strength '90*, Vol. 51-52, 1991, pp. 367.

50. Bueckner, H.F., "The Propagation of Crack and the Energy of Elastic Deformation," *Transactions of the ASME*, Series A-D 80, 1958, pp. 1225-1230.

51. Heaton, M.D., "On the Calculation of Stress Intensity Factors Due to Thermal and Residual Stress Fields," *CEGB Research Report NW/SSD/RR/158*, 1976.

52. Rice, J.R., "Mechanics of Crack-Tip Deformation and Extension by Fatigue," *Fatigue Crack Propagation, ASTM STP 415*, American Society for Testing and Materials, 1967, pp. 247-311.

53. Broek, D., *Elementary Engineering Fracture Mechanics*, 4th Edition, Kluwer Academic Publishers, Dordrecht, The Netherlands, 1986.

54. Elber, W., "Fatigue Crack Closure Under Cyclic Tension," *Engineering Fracture Mechanics*, 1970, Vol. 2, pp. 37-44.

55. Elber, W., "The Significance of Fatigue Crack Closure, Damage Tolerance in Aircraft Structures," *Damage Tolerance in Aircraft Structures, ASTM STP 486,* American Society for Testing and Materials, 1971, pp. 230-242.

56. ASTM E647 Standard Test Method for Measurement of Fatigue Crack Growth Rates, Annual Book of ASTM Standards, ASTM International, 2000.

57. Hill, M.H., VanDalen, J.E., Stuart, D.H., and Minotti, J.R., Jr., "Analytical Tools for Residual Stress Enhancement of Rotorcraft Damage Tolerance–Volume 3: Residual Stress Measurements, Crack Growth Testing and LEFM Analyses," DOT/FAA/AR-xx/xx, V3**.**

58. Dane, C.B., "High Power Laser for Peening of Metals Enabling Production Technology," *Materials and Manufacturing Processes*, Vol. 15, No. 1, 2000, pp. 81-96.

59. Hammersley, G., Hackel, L.A., and Harris, F., "Surface Prestressing to Improve Fatigue Strength of Components by Laser Shot Peening," *Optics & Lasers in Engineering*, Vol. 34, No. 4-6, 2000, pp. 327-337.

60. Prime, M.B., "Cross-Sectional Mapping of Residual Stresses by Measuring the Surface Contour after a Cut," *Journal of Engineering Materials and Technology*, Vol. 123, 2001, pp. 162-168.

61. Wu, X.-R. and Carlsson. J., *Weight Functions and Stress Intensity Factor Solutions*, Pergamon Press, Oxford, New York, 1991, pp. 513.

62. Daniewicz, S.R. and Newman, J.C., Jr., "Development and Validation of Crack Growth Models and Life Enhancement Methods for Rotorcraft Damage Tolerance," FAA Report DOT/FAA/AR-07/50, 2007.

63. LaRue, J.E., "The Influence of Residual Stress on Fatigue Crack Growth," M.S. Thesis, Mississippi State University, 2005.

64. Newman, J.C., Jr., "A Nonlinear Fracture Mechanics Approach to the Growth of Small Cracks," *Behavior of Short Cracks in Airframe Components, AGARD Conference Proceedings*, No. 328, 1983.

65. Newman, J.C., Jr., Swain, M.H., and Phillips, E.P., "An Assessment of the Small-Crack Effect for 2024-T3 Aluminum Alloy," *Small Fatigue Cracks*, The Metallurgical Society, Inc., Warrendale, Pennsylvania, 1986, pp. 427-452.

66. Swain, M.H., Everett, R.A., Newman, J.C., Jr., and Phillips, E.P., "The Growth of Short Cracks in 4340 Steel and Aluminum-Lithium 2090," AGARD R-767, 1990, pp. 7.1-7.30.

67. Newman, J.C., Jr., "Effects of Constraint on Crack Growth Under Aircraft Spectrum Loading," *Fatigue of Aircraft Materials*, Delft, The Netherlands, Delft University Press, 1992, pp. 83-109.

68. Newman, J.C., Jr., Phillips, E.P., and Swain, M.H., "Fatigue-Life Prediction Methodology Using Small-Crack Theory," *International Journal of Fatigue*, Vol. 21, 1999, pp. 109-119.

69. Everett, R.A., Jr., Newman, J.C., Jr., and Phillips, E.P., "The Effects of Machining-Like Scratch on the Fatigue Life of 4340 Steel," *Proceedings of the American Helicopter Society, 55th Annual Forum*, Montreal, Quebec, Canada, May 25-27, 1999.

70. Lam, Y.C. and Lian, K.S., "Effect of Residual Stress and its Redistribution on Fatigue Crack Growth," *Theoretical Applied Fracture Mechanics*, Vol. 12, No. 1, 1989, pp. 59-66.

71. Newman, J.C., Jr., Daniewicz, S.R., LaRue, J., and Le, Dy, "FASTRAN Analyses of Coupons With Residual Stresses Due to Overloads and Cold-Worked Holes," *Ninth Joint FAA/DoD/NASA Aging Aircraft Conference*, Atlanta, Georgia, 2006.

72. Pavier, M.J., Poussard, C., and Smith, D.J., "A Finite-Element Simulation of the Cold Working Process for Fastener Holes," *Journal of Strain Analysis*, Vol. 32, No. 4, 1997, pp. 287-300.

73. Rich, D.L. and Impellizzeri, L.F., "Fatigue Analysis of Cold-Worked and Interference Fit Fastener Holes," *ASTM STP 637, American Society for Testing and Materials*, 1975, pp. 153-175.

74. Chang, C. and Mear, M.E., "A Boundary-Element Method for Two-Dimensional Linear Elastic Fracture Analysis," *International Journal of Fracture*, Vol. 74, 1996, pp. 219-251.

75. Restis, J. and Reid, L., "Process Specification 8101D: Cold Expansion of Holes Using the Standard Split Sleeve System and Countersink Cold Expansion," Fatigue Technology Inc., Seattle, Washington, 2002.

76. Ball, D.L., "Elastic-Plastic Stress Analysis of Cold Expanded Fastener Holes," *Fatigue and Fracture of Engineering Materials and Structures*, Vol. 18, 1994, pp. 47-63.

77. Priest, M.J., Poussard, C.G., Pavier, M.J., and Smith, D.J., "An Assessment of Residual Stress Measurements Around Cold-Worked Holes," *Experimental Mechanics*, Vol. 15, No. 4, 1995, pp. 579-589.

78. Kang, J., Johnson, W.S., and Clark, D.A., "Three-Dimensional Finite Element Analysis of the Cold Expansion of Fastener Holes in Two Aluminum Alloys," *Journal Engineering Materials and Technology*, Vol. 124, 2002, pp.140-145.

79. Kim, C., Kim, D., Seok, C., and Yang, W., "Finite Element Analysis of the Residual Stress by Cold Expansion Method Under the Influence of Adjacent Holes," *Journal of Material Processing Technology*, Vol. 153, No. 4, 2004, pp. 986-991.

80. Garcia-Granada, A.A., Lacarac, V.D., Holdway, P., Smith, D.J., and Pavier, M.J., "Creep Relaxation of Residual Stresses Around Cold Expanded Holes," *Journal of Engineering Materials and Technology*, 2001, Vol. 123, pp. 125-131.

81. Papanikos, P. and Meguid, S.A., "Three-Dimensional Finite Element Analysis of Cold Expansion of Adjacent Holes," *International Journal of Mechanics and Science*, Vol. 40, 1998, pp. 1019-1028.

82. Chakherlou, T.N. and Vogwell, J., "The Effect of Cold Expansion on Improving the Fatigue Life of Fastener Holes," *Engineering Failure Analyses*, Vol. 10, 2003, pp. 13-14.

83. Chakherlou, T.N. and Vogwell, J., "A Novel Method of Cold Expansion Which Creates Near-Uniform Compressive Tangential Residual Stress Around a Fastener Hole," *Fatigue and Fracture of Engineering Materials and Structures*, Vol. 27, 2003, pp. 343-351.

84. de Matos, P.F., Moreire, P.M., Camanho, P.P., and de Castro, P.M., "Numerical Simulation of Cold Working of Rivet Holes," *Journal of Finite-Element Analyses and Design*, Vol. 41, 2005, pp. 989-1007.

85. de Matos, P.F., Moreire, P.M., Camanho, P.P., and de Castro, P.M., "Residual Stress Effect on Fatigue Striation Spacing in a Cold-Worked Rivet Hole," *Theoretical and Applied Fracture Mechanics*, Vol. 42, 2004, pp. 139-148.

86. Pavier, M.J., Poussard, C.G., and Smith, D.J., "Effect of Residual Stress Around Cold Worked Holes on Fracture Under Superimposed Mechanical Load," *Engineering Fracture Mechanics*, Vol. 63, No. 6, 1999, pp. 751-773.

87. Reid, L., Private Communication, *Residual Stress Summit*, Oak Ridge National Laboratory, Oak Ridge, Tennessee, 2007.

88. Karabin, M.E., Barlat, F., and Schultz, R.W., "Numerical and Experimental Study of Cold Expansion Process in 7085 Plate Using a Modified Split Sleeve," *Journal of Material Processing and Technology*, Vol. 189, 2007, pp. 45-57.

89. Rice, R.C., Jackson, J.L., Bakuckas, J., and Thompson, S., "Metallic Materials Properties Development and Standardization," MMPDS-01, DOT/FAA, Springfield, Virginia, 2003, Chapter 3.7.3.

90. ANSYS Inc., Release 11.0 Documentation for ANSYS, Chapter 8.3-12, 2001.

91. Prime, M.B., "Cross-Sectional Mapping of Residual Stresses by Measuring the Surface Contour After a Cut," *Journal of Engineering Materials and Technology*, Vol. 123, 2001, pp. 162-168.

92. DeWald, A.T., Rankin, J.E., Hill, M.R., Lee, M.J., and Chen, H.L., "Assessment of Tensile Residual Stress Mitigation in Alloy 22 Welds Due to Laser Peening," *Journal of Engineering Materials and Technology*, Vol. 126, No. 4, 2004, pp. 465-473.

93. Prime, M.B., Sebring, R.J., Edwards, J.M., Hughes, D.J., and Webster, P.J., "Laser Surface-Contouring and Spline Data-Smoothing for Residual-Stress Measurement," *Experimental Mechanics*, Vol. 44, 2004, No. 2, pp. 176-184.

94. Coker, E.G., Filon, L.N.G., and Jessop, T.D., "A Treatise on Photo-Elasticity," 2nd Edition, Cambridge University Press, United Kingdom, 1957, pp. 524-530.

95. Frocht, M.M., "Photoelasticity," 4th Edition, Vol. II, Wiley Press, New York, New York, 1948, pp. 179-193.

96. Ahmad, I. and Stanley, P., "Deformations and Stresses in Pin-Loaded Tubes Under Axial Tension," *Journal of Strain Analysis*, Vol. 35, No. 5, 2000, pp. 329-345.

97. Cloud, G.L., "Optical Methods for Engineering Analysis," 1st Edition, Cambridge University Press, New York, New York, 1998, pp. 323-340.

98. Herrera-Franco, P.J., Cloud, G.L., and Zimmerman, K., "Moire Study of 2 and 3 – Hole Arrays of Composite Material Fasteners," *International Conference on Advanced Measurement Techniques*, London, United Kingdom, 1987, pp. 25-35.

99. Lanza di Scalea, F., Hong, S.S., and Cloud, G.L., "Whole-Field Measurement in a Pin-Loaded Plate by Electronic Speckle Pattern Interferometry and the Finite Element Method," *Experimental Mechanics*, Vol. 38, No. 1, 1998, pp. 55-60.

100. Noble, B. and Hussain, M.A., "Exact Solutions of Certain Dual Series for Indentation and Inclusion Problems," *International Journal of Engineering Science*, Vol. 7, 1969, pp. 1149-1161.

101. Hyer, M.W. and Klang, E.C., "Contact Stresses in Pin-Loaded Orthotropic Plates," *International Journal of Solid and Structures*, Vol. 21, No. 9, 1985, pp. 957-975.

102. Ho, K.C. and Chau, K.T., "A Finite Strip Loaded by a Bonded-Rivet of a Different Material," *Journal of Computers and Structures*, Vol. 70, 1999, pp. 203-218.

103. Echavarria, C., Haller, P., and Salenikovich, A., "Analytical Study of a Pin-Loaded Hole in Elastic Orthotropic Plates," *Journal of Composite Structures*, Vol. 79, 2007, pp. 107-112.

104. Rao A.K., "Elastic Analysis of Pin Joints," *Journal of Computers and Structures*, Vol. 9, 1978, pp. 125-144.

105. Mangangiri, P.D., Ramamurthy, T.S., Dattaguru, B., and Rao, A.K., "Elastic Analysis of Pin Joints in Plates Under Some Combined Pin and Plate Loads," *International Journal of Mechanics and Science*, Vol. 29, No. 8, 1987, pp. 577-585.

106. Mizushima, I. and Hamada, M., "Stress Analysis Around Circular Hole in Infinite Plate With Rigid Disk," *Bulletin of JSME*, Vol. 26, No. 218, 1983, pp. 1296-1301.

107. Ho, K.C. and Chau, K.T., "An Infinite Plane Loaded by a Rivet of a Different Material," *International Journal of Solids and Structures*, Vol. 34, No. 19, 1997, pp. 2477-2496.

108. Mangangiri, P.D., Dattaguru, B. and Rao A.K., "Finite Element Analysis of Moving Contact in Mechanically Fastened Joints," *Nuclear Engineering and Design*, Vol. 78, 1984, pp. 303-311.

109. Solodivnikov, V.N., "Solution of the Contact Problem for a Pin-Loaded Plate," *Journal of Applied Mechanics and Physics*, Vol. 38, No. 1, 1997, pp. 109-115.

110. Newman, J.C., Jr., Harris, C.E., James, M.A., and Shivakumar, K.N., "Fatigue-Life Prediction of Riveted Lap-Splice Joints Using Small-Crack Theory," *Proceedings of Fatigue in New and Ageing Aircraft Symposium*, Vol. 1, ICAF, 1997, pp. 523-552.

111. Iyer, K., "Solutions for Contact in Pinned Connections," *International Journal of Solids and Structures*, Vol. 38, 2001, pp. 9133-9148.

112. Yavari, V., Rajabi, I., Daneshvar, F., and Kadivar, M., "On the Stress Distributions Around the Hole in Mechanically Fastened Joints," *Mechanical Research and Communication*, Vol. 36, No. 3, 2008, pp. 373-380.

113. Kumar S.K., Dattaguru, B., Ramamurthy, T.S., and Raju, K.N., "Elasto-Plastic Contact Stress Analysis of Joints Subjected to Cyclic Loading," *Journal of Computers and Structures*, Vol. 60, No. 6, 1996, pp. 1067-1077.

114. Ismonov, S., Daniewicz, S.R., Newman, J.C., Jr., Hill, M.R., and Urban, M.R., "Three Dimensional Finite Element Analysis of a Split-Sleeve Cold Expansion Process," *Journal of Engineering Materials and Technology*, Vol. 131, No. 3, 2009, pp. 71-78.

115. Isida, M., "Laurent Series Expansion for Internal Crack Problems," Methods of Analysis and Solutions of Crack Problems, G.C. Sih, ed., Noordhoff International Publishing, Leyden, The Netherlands, 1973, p. 110.

116. Daniewicz, S.R., "Accurate and Efficient Numerical Integration Weight Functions Using Gauss-Chebyshev Quadrature," *Engineering Fracture Mechanics*, Vol. 48, 1994, pp. 541-544.

APPENDIX A—GREEN'S FUNCTION FOR COMPACT SPECIMEN

A.1 INTRODUCTION.

In the aerospace industry, residual stresses are induced in sheets and plates by using shock-peening or laser shock peening (LSP) techniques, or around fastener holes by using the CX process to improve fatigue and crack propagation lives. Structural components machined from plates or forgings may also have internal residual stresses from either the machining or the manufacturing process. Knowledge and measurement of these residual stresses are necessary to establish their influence on structural performance.

There are at least two methods to account for residual stresses on crack growth and fracture. The traditional method is linear superposition, in which tractions from an uncracked body are applied to the crack faces to calculate the stress intensity factors (SIF). The second method is explicitly modeling cracking in the context of nonlinear stress analyses that induce residual stresses from plastic deformations, such as the CX process and forging. The linear superposition method [A-1 and A-2] will be used here to calculate the influence of residual stress distributions on SIFs in the compact (C(T)) specimen, as shown in figure A-1. Bueckner [A-1] and Tada et al. [A-2] have mathematically demonstrated that, for linear elastic materials, SIFs resulting from a given applied loading may be computed using the stress distribution in the uncracked body. The C(T) specimen is widely used to generate the baseline fatigue crack growth rate properties for a material. The data generated on C(T) specimens are then used to predict the fatigue crack growth lives of structural components. Residual stresses are a concern and may be present in the material from the machining or manufacturing processes, such as friction-stir welding, or by the various life enhancement methods, such as LSP. The presence of these unknown residual stresses may inadvertently influence the baseline properties and should be accounted for in crack growth and fracture analyses. Knowledge of the residual stresses would allow the use of the Green's function (GF) to calculate the residual SIFs to determine baseline material fatigue crack growth and fracture properties. It should be noted that partial crack closure, crack-face contact along the crack surfaces, is not accounted for in the GF analyses. Some residual stress distributions may cause negative SIFs that are valid, as long as the total applied SIF and the crack-face displacements are positive. Negative crack-face displacements indicate partial crack closure. Residual stress distributions or loading that will cause partial crack closure are beyond the scope of the present work.

The objective of this appendix is to develop the GF for the standard C(T) specimen, as shown in figure A-2. The GF is the SIF due to a pair of concentrated forces applied to the crack surfaces. The GF can then be used to calculate the residual SIF (K_{RS}) for an arbitrary residual stress distribution along the crack path. Finite element (FE) [A-3 through A-6] and boundary element [A-7] analyses were used to obtain SIFs over a wide range of crack-length-to-width (a/W) ratios and in concentrated force locations along the crack surfaces from the front face to near the crack tip. The results were compared with boundary collocation results from the literature [A-8 through A-10]. These results were then used to develop an improved GF equation for the C(T) specimen. As a validation of the newly developed wide-range equation, SIFs were calculated on a C(T) specimen subjected to a stress distribution induced by the standard pin loading without a

crack starter notch or crack, and the results were compared with the solutions from the literature [A-10 and A-11].

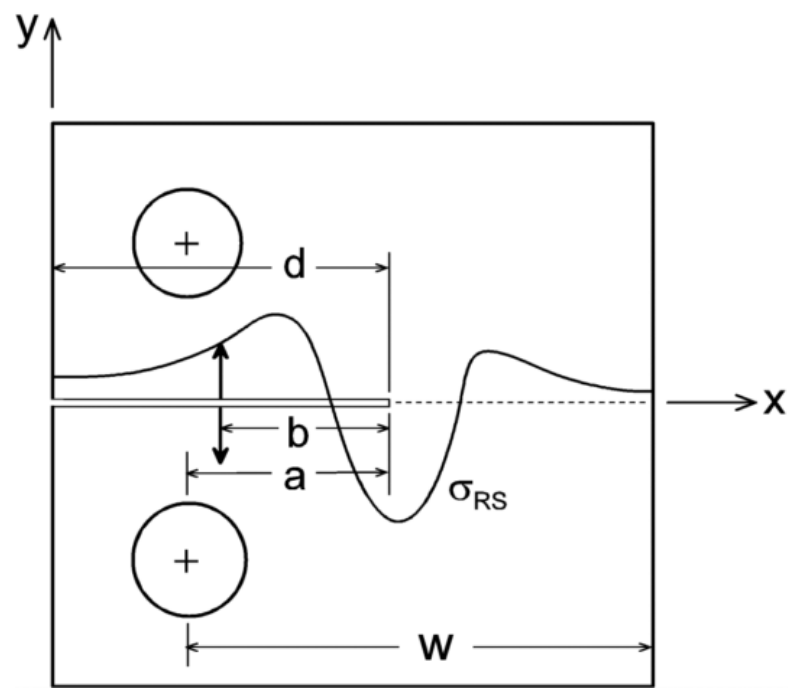

Figure A-1. The C(T) Specimen Subjected to Arbitrary Residual Stress Distribution Along Crack Plane

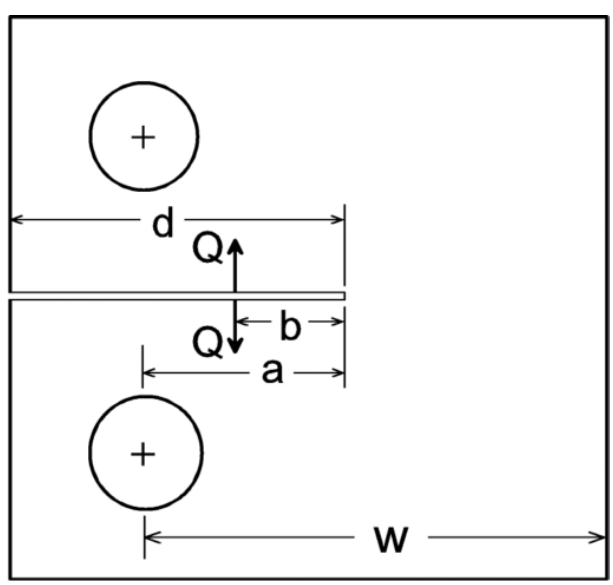

Figure A-2. The C(T) Specimen Subjected to a Pair of Concentrated Forces on Crack Surfaces

A.2 ANALYSES.

Herein, two methods have been used to calculate SIFs for various crack lengths in the standard C(T) specimen subjected to a pair of concentrated forces applied to the crack surfaces (figure A-2). The new results are compared with previous results from a boundary-collocation analysis [A-8].

The FRANC2DL FE code [A-3 through A-6] was used with the *J*-integral option to extract the SIFs from the stress-strain fields around the crack tip location. Two-dimensional, FE models having about 50k to 60k degrees of freedom and using a ring of six-noded quarter-point elements around the crack tip and eight-noded elements elsewhere were used under plane stress conditions. It should be noted that solution for a concentrated load is independent of the state of stress; thus, plane stress conditions were selected for convenience. The minimum element size at the crack-tip location was 0.0025w. The (a/W) ratios varied from 0.2 to 0.9, with nodal forces applied at various locations along the crack surfaces.

The FADD2D [A-7] code was also used to validate and conduct stress analyses for a pair of simulated forces applied at the crack mouth location ($b/d = 1$) for various a/W ratios. The forces were simulated by applying linear shear traction over a small region ($0.1w$) along the front face at the crack mouth. The code was also used to calculate the SIFs for the standard C(T) specimen with simulated pin loading for a/W ratios from 0.2 to 0.9. The boundary element models had 200 quadratic elements on the external boundary, 36 quadratic elements on each hole boundary with and without a contact pressure simulating pin loading over ±45 degrees on the hole, and 30 to 60 linear elements along the crack surface.

A.3 RESULTS.

The GF for the C(T) specimen was obtained by conducting stress analyses of the specimen subjected to a pair of concentrated forces per unit thickness, Q, applied on the crack surface, as shown in figure A-2. The SIF is:

$$K_Q = 2Q/\sqrt{(2\pi b)}\, F(a/W, b/w') \qquad \text{(A-1)}$$

for $0.2 \leq a/W \leq 0.9$ and $0 \leq b/d \leq 1$, where w is the width of the specimen and w' is the distance from the force to the back face of the specimen ($w' = 1.25\ w + b - d$). The leading term in equation A-1 is the exact solution for a pair of forces applied to a semi-infinite crack surface in an infinite body [A-2]. The function F is the boundary correction factor that accounts for the influence of the external boundaries on the SIF, such as the width, height, and location of the holes.

A boundary-collocation analysis and the original GF equation are given in references A-7. In the original stress analysis, the location of the concentrated forces were restricted to b less than a, and forces applied between the standard pinhole centerline and the front face (crack mouth) were not allowed.

Figure A-3 shows a comparison of the various boundary correction factors calculated for the C(T) specimen subjected to a pair of concentrated forces. The normalized boundary correction factor, $F \cdot (1 - \Delta)^{3/2}$, is plotted against Δ (= b/w'). The original SIF solutions are shown as solid symbols and the dashed curves are from the original GF equation for various *a/W* ratios. The figure shows how the original equation overestimated the boundary correction factors for *a/W* ratios less than approximately 0.4. The open symbols are the results from FRANC2DL and the diamond symbols are the results from FADD2D for a pair of forces applied at the crack mouth. The solid curves show the improved equation for the boundary correction factor. The equation is given by:

$$F(\alpha,\Delta) = (1 + A_1\,\Delta + A_2\,\Delta^2)\,[1 - 1.05\,(1-\alpha)^9\,(\Delta/\Delta_o)^3]\,/\,(1-\Delta)^{3/2} \qquad \text{(A-2)}$$

$$A_1 = 3.6 + 12.5\,(1-\alpha)^8$$

$$A_2 = 5.1 - 15.32\,\alpha + 16.58\,\alpha^2 - 5.97\,\alpha^3$$

$$\Delta_o = 0.8\,\alpha + 0.2$$

where $\alpha = a/W$, $\Delta = b/w'$, $0 \le \Delta \le \Delta_o$, and $0.2 \le \alpha \le 0.9$. (The parameter w' was used in the normalization because the exact solution for mode III loading [2] has this normalizing parameter. This form would also be useful for mode I loading.) Equation A-2 is within ±1 percent of the numerical results for $\alpha > 0.4$ and within ±1.3 percent for $0.2 \le \alpha \le 0.4$.

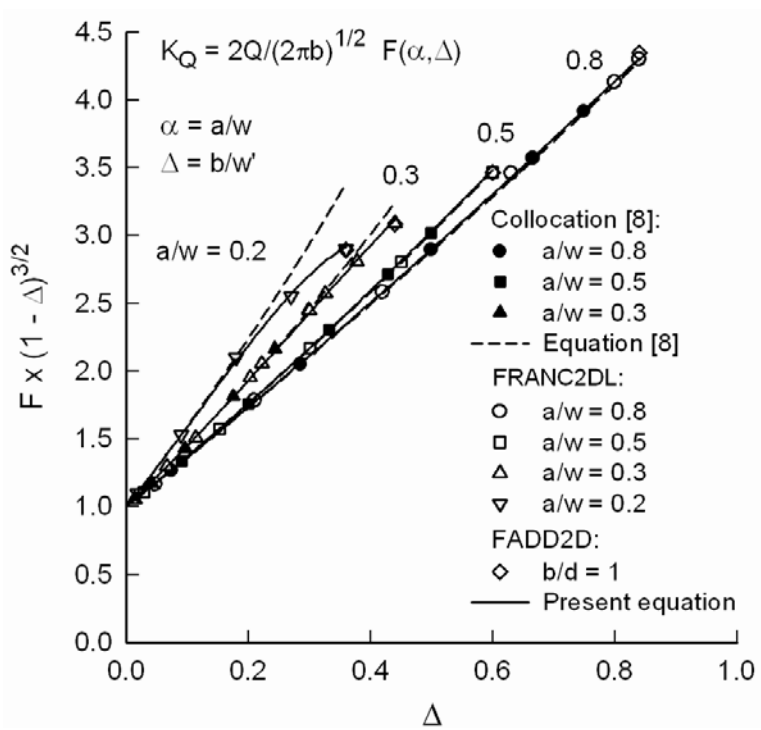

Figure A-3. Comparisons Among Normalized Boundary Correction Factors for C(T) Specimen With Pair of Concentrated Forces Applied to Crack Surfaces

Figure A-4 shows a comparison of results for a pair of concentrated forces applied at the crack mouth ($\Delta = \Delta_o$) as a function of *a/W*. The dashed curve shows the original equation, which demonstrates how the equation over-estimated the results for $a/W < 0.4$. However, the original equations were not intended for concentrated forces applied between the pinhole centerline and the crack mouth. The circle and square symbols show the FRANC2DL and FADD2D results, respectively, which agree well with each other. Some slight differences (~1%) occur for very deep cracks ($a/W \geq 0.7$). The solid curve shows the present equation A-2, which agrees within about ±1 percent of the FE and boundary element code results.

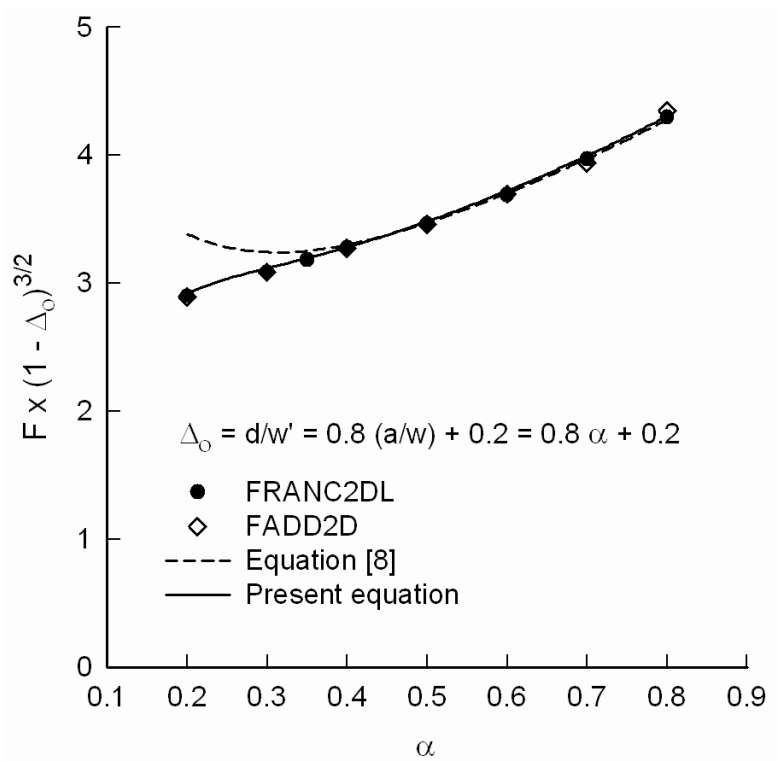

Figure A-4. Comparisons Among Normalized Boundary Correction Factors for Pair of Concentrated Forces Applied at the Crack Mouth

A.4 EXAMPLE.

The improved SIF equation GF for the standard C(T) specimen can be used to calculate the SIFs for various residual stress distributions along the crack surfaces. The location for the pair of concentrated forces can be at any location along the crack surface from the crack tip to the crack mouth for $0.2 \leq a/W \leq 0.9$.

To validate the improved equation, a standard C(T) specimen was analyzed without a crack-starter notch or crack. Next, the stress fields for two cases were analyzed: (1) the C(T) specimen subjected to simulated pinhole contact loading and (2) the C(T) specimen with no hole, but with concentrated forces applied at $y/w = \pm 0.525$w and $x/w = 0.25$ (location of the top and bottom of the holes, if they were present). The specimen width was 1.0 unit and the specimen was

subjected to a unit load, $P/B = 1$, where B is the plate thickness. Figure A-5 shows the normal stress plotted along the crack-plane axis (center line, $y = 0$). The solid curve shows the normal stresses for the standard C(T) specimen (no crack) with pin loading and the dashed curve is the specimen with no holes with only concentrated forces. The holes had a strong influence on the normal-stress distribution.

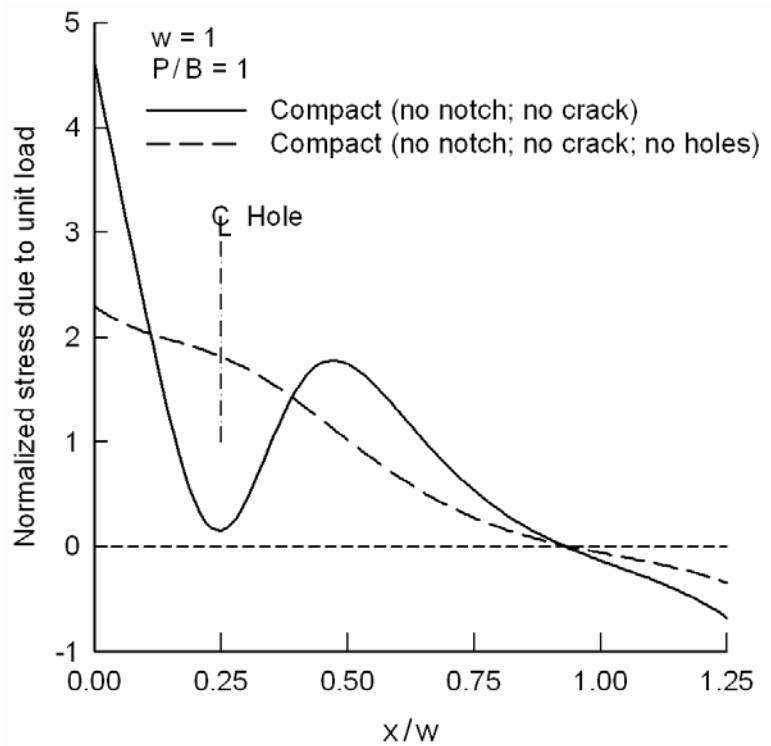

Figure A-5. Normal Stresses Along Crack Plane With and Without Holes in a C(T) Specimen (no crack) Subjected to Splitting Forces at $y/w = \pm 0.525$

These results were then used with a numerical integration scheme to calculate the SIFs due to the normal stresses as a function of a/W. Table A-1 shows a comparison of the normalized K solutions for the standard C(T) pin-loaded hole specimen from the boundary collocation analysis [10], the equation in the ASTM standards [11], FADD2D, and the numerical integration of the GF (equations A-1 and A-2). The K solution from the ASTM standards was obtained by fitting to the boundary collocation results [A-10 and A-11]. The standard solution and FADD2D agreed within 1%, while the difference between FADD2D and the GF method was also within 1%.

Table A-1. Comparison of Normalized SIFs for Standard C(T) Specimen

The *a/W*	Boundary Collocation [10]	Standard ASTM Solution [11]	FADD2D	Numerical Integration (GF)	Difference From FADD2D %
0.2	4.29	4.274	4.316	4.354	0.88
0.3	5.63	5.621	5.641	5.666	0.44
0.4	7.27	7.279	7.272	7.267	-0.07
0.5	9.63	9.659	9.623	9.667	0.46
0.6	13.64	13.65	13.76	13.76	0.00
0.7	21.57	21.55	21.74	21.73	-0.05
0.8	41.13	41.20	41.33	41.26	-0.17
0.9	---	121.9	121.6	121.2	-0.32

A.5 CONCLUDING REMARKS.

The GF for the standard C(T) specimen was developed, and it can be applied over a wide range of crack configuration parameters and for any arbitrary residual stress distribution along the crack path from the front face to the back face. The FE and boundary element analyses were used to obtain SIFs over a wide range in (a/W) and in concentrated force locations. These results were compared with previous boundary collocation results from the literature and were used to improve the GF equation. As a validation of the newly developed wide-range equations, SIFs were calculated on a C(T) specimen subjected to a stress distribution induced by the standard pin loading without a crack-starter notch or crack and were compared with the well-known solution from the literature. The accuracy of the GF equation is within approximately ±1.3% of the numerical analyses over a wide range in a/W ratios from 0.2 to 0.9.

A.6 REFERENCES.

A-1. Bueckner, H.F., "The Propagation of Cracks and the Energy of Elastic Deformation," Transactions of the ASME, Series A-D 80, 1958, pp. 1225-1230.

A-2. Tada, H., Paris, P.C., and Irwin, G.R., "The Stress Analysis of Cracks Handbook," Third Edition, The American Society of Mechanical Engineers, 2000.

A-3. Wawrzynek, P.A. and Ingraffea, A.R., "Interactive Finite Element Analysis of Fracture Processes: An Integrated Approach," *Theoretical and Applied Fracture Mechanics*, No. 8, 1987, pp. 137-150.

A-4. Wawrzynek, P.A. and Ingraffea, A.R., "FRANC2D: Two-Dimensional Crack Propagation Simulator, Version 2.7 User's Guide," NASA CR 4572, 1994.

A-5. Gondhalekar, S., "Development of a Software Tool for Crack Propagation Analysis in Two-Dimensional Layered Structures," Masters Thesis, Kansas State University, 1992.

A-6. James, M.A. and Swenson, D.V., "A Software Framework for Two-Dimensional Mixed Mode-I/II Elastic-Plastic Fracture," *Mixed-Mode Crack Behavior*, ASTM STP 1359, K.J. Miller and D.L. McDowell, Eds., American Society for Testing and Materials, West Conshohocken, Pennsylvania, 1999, pp. 111-126.

A-7. Chang, C.C. and Mear, M.E., "A Boundary Element Method for Two-Dimensional Linear Elastic Fracture Analysis," *International Journal of Fracture*, Vol. 74, 1996, pp. 219-251.

A-8. Mall, S. and Newman, J.C., Jr., "The Dugdale Model for Compact Specimen," *Fracture Mechanics: Sixteenth Symposium*, ASTM STP 868, M.F. Kanninen and A.T. Hopper, Eds., American Society for Testing and Materials, Philadelphia, Pennsylvania, 1985, pp. 113-128. (Also NASA TM-85714, October 1983).

A-9. Newman, J.C., Jr., and Mall, S. "Dugdale Plastic Zone Size and CTOD Equations for the Compact Specimen," *International Journal of Fracture*, Vol. 24, 1984, pp. R59-R63.

A-10. Newman, J.C., Jr., "Stress Analysis of the Compact Specimen Including the Effects of Pin Loading," *Fracture Analysis—Part II*, ASTM STP 560, American Society for Testing and Materials, Philadelphia, Pennsylvania, 1974, pp. 105–121.

A-11. Srawley, J.E., "Wide Range Stress Intensity Factor Expressions for ASTM Method E 399 Standard Fracture Toughness Specimens," *International Journal of Fracture*, Vol. 12, 1976, pp. 475-476.

APPENDIX B—LINEAR SUPERPOSITION LIFE PREDICTION CODE

B.1 INTRODUCTION.

The FORTRAN code, *KRS.for*, was developed and used to calculate fatigue crack growth rate *da/dN* in a residual stress field for a general through-thickness crack configuration. This code uses the superposition technique to calculate fatigue crack growth. The superposition technique is the addition of the applied stress-intensity factors (SIF) due to external loads and residual SIFs from internal residual stresses to give the maximum and minimum resultant SIFs as a function of normalized crack length (a/W). The residual stresses or residual SIFs as a function of crack length were obtained by either experimental or numerical methods. Herein, the residual stresses were obtained by the cut-compliance method (laser shock-peened compact (C(T)) specimens [1]) or the finite element method (FEM) (open hole specimens [2]). The residual SIFs for the laser shock-peened C(T) specimens were then calculated using the Green's function (GF) method [3]. The applied SIFs for the particular crack configuration were calculated under the desired maximum and minimum loading conditions as a function of the same normalized crack lengths that were used for the residual SIFs.

The SIF range (ΔK) was computed as the difference between the maximum and minimum resultant SIFs and also the residual stress intensity ratio (R_{rs}) was calculated. Thus, the crack growth rate (*da/dN*) at this R_{rs} and ΔK is calculated in the following manner. The material must have a given ΔK_{eff} against *da/dN* relation in table form. The table gives ΔK_{eff} as a function of rate using 5 to 9 points, depending upon the particular material. First, the normalized crack opening stresses (S_o/S_{max} or K_{op}/K_{max}) are found from Newman's equation [4] (using $S_{max}/\sigma_o = 0.3$). Thus, the crack-opening ratio was only a function of the stress ratio (R) and constraint factor (α). Using the crack opening ratio, the ΔK_{eff} value and corresponding rate (*da/dN*) were determined at a given crack length. Using this crack growth rate, and with a prescribed small Δa, a corresponding ΔN was found. These incremental values were added to the previous values of a and N in calculating total life. The user guide, sample input and output files, and the FORTRAN code are also given herein.

B.2 USER GUIDE.

INPUT DATA FILE

1. READ(*,*) TITLE

Any 80-character title that describes the problem.

2. READ(*,*) TITLE1

Header: Type in "**W B Ai Kc**". Note: The header appears in the input file to help the user input appropriate data.

3. READ(*,*) W, B, AI, KC

W = width of specimen or component
B = thickness of specimen or component
AI = initial crack length
KC = fracture toughness (maximum elastic stress-intensity at failure)

4. READ(*,*) MAT

Any 80-character title that describes the material.

5. READ(*,*) MTAB

MTAB = number of ΔK_{eff}-rate data points (normally 5 to 9)

7. READ(*,*) TITLE1

Header: Type in "**DKeff Rate**". Note: The header appears in the input file to help the user input appropriate data.

8. READ(*,*) DKETAB(I), CGRTAB(I)

DKETAB(I) = effective stress-intensity-factor range, ΔK_{eff}
CGRTAB(I) = crack-growth rate

9. READ(*,*) TITLE1

Header: Type in "**Constraint-loss regime:**". Note: The header appears in the input file to help the user input appropriate data.

10. READ(*,*) RATE1, ALP1, RATE2, ALP2

RATE1 = rate at start of constraint-loss regime
ALP1 = constraint factor at start of constraint-loss regime
RATE2 = rate at end of constraint-loss regime
ALP2 = constraint factor at end of constraint-loss regime

11. READ(*,*) NTAB

NTAB = number of crack length against residual stress-intensity factor data points

12. READ(*,*) TITLE1

Header: Type in "**a/W Kmax+Krs Kmin+Krs**". Note: The header appears in the input file to help the user input appropriate data.

13. READ(*,*) AW(J), KMAX(J), KMIN(J)

AW(J) = normalized crack length to width (a/W) ratio
KMAX(J) = maximum stress-intensity factor (Kmax + Krs)
KMIN(J) = minimum stress-intensity factor (Kmin + Krs)

B.3 EXAMPLE DATA FILE.

The example data file is a single crack growing from an open hole in a 7075-T6 aluminum alloy specimen that had been cold-worked (3%) in the hole and then reamed. The residual stresses were calculated from an elastic-plastic finite-element method (herein) simulating a 3% cold-worked hole, reamed and notched. The applied and residual SIFs were calculated from a two-dimensional GF (K2DL [5]) code.

B.3.1 INPUT FILE.

```
CRACK-GROWTH LIFE  Single Crack at Cold-Worked Hole
    W      B      Ai      Kc
 0.0222 0.0038  0.00025  60.0
 7075-T6 NASA RP-1309
    8
  DKeff      Rate
   0.9      1.00E-11
   1.25     1.00E-09
   3.4      1.00E-08
   5.2      1.00E-07
  11.9      1.00E-06
  20.0      1.00E-05
  50.0      7.00E-04
  88.0      0.01
Constraint-loss regime:
  0.70E-06  1.8  0.70E-05  1.2
 199
  a/W     Kmax+Krs   Kmin+Krs
0.011261  10.386912  1.038691
0.015034  5.021954  -5.415305
0.018806  1.317620  -9.977938
0.022579  0.285797  -11.705620
0.026351  0.531962  -12.034704
0.030124  0.941105  -12.108089
0.033896  1.425098  -12.033590
0.037669  1.960011  -11.849599
0.041441  2.550013  -11.562899
0.045216  3.141694  -11.235531
0.048986  3.758000  -10.850800
0.052761  4.395508  -10.418049
0.056532  5.048495  -9.946851
```

```
 (data intentionally removed)

0.720495  54.554270 6.350423
0.724279  55.816968 6.478331
0.728063  57.174093 6.615636
0.731802  58.619967 6.761799
0.735586  60.203999 6.921750
0.739369  61.927127 7.095503
0.743153  63.811203 7.285440
0.746892  65.856605 7.491241
0.750676  68.145670 7.721317
0.754459  70.697270 7.977827
0.758243  73.565381 8.265988
```

B.3.2 OUTPUT FILE.

```
CRACK-GROWTH LIFE  Single Crack at Cold-Worked Hole

  Width(W)= 0.222E-01  Thickness(B)= 0.380E-02  Crack length(Ai)= 0.2500E-03
     Fracture toughness (Kc)=  0.6000E+02

 7075-T6 NASA RP-1309
     DKeff         Rate
    0.9000E+00    0.1000E-10
    0.1250E+01    0.1000E-08
    0.3400E+01    0.1000E-07
    0.5200E+01    0.1000E-06
    0.1190E+02    0.1000E-05
    0.2000E+02    0.1000E-04
    0.5000E+02    0.7000E-03
    0.8800E+02    0.1000E-01

 CONSTRAINT-LOSS REGIME:
 RATE AT START OF TRANSITION = 0.7000E-06  WITH  ALP1 = 1.80
 RATE AT  END  OF TRANSITION = 0.7000E-05  WITH  ALP2 = 1.20

    a/W       Kmax+Krs      Kmin+Krs
   0.01126    0.1039E+02    0.1039E+01
   0.01503    0.5022E+01   -0.5415E+01
   0.01881    0.1318E+01   -0.9978E+01
   0.02258    0.2858E+00   -0.1171E+02
   0.02635    0.5320E+00   -0.1203E+02
   0.03012    0.9411E+00   -0.1211E+02
   0.03390    0.1425E+01   -0.1203E+02
   0.03767    0.1960E+01   -0.1185E+02
   0.04144    0.2550E+01   -0.1156E+02
   0.04522    0.3142E+01   -0.1124E+02
   0.04899    0.3758E+01   -0.1085E+02
   0.05276    0.4396E+01   -0.1042E+02
   0.05653    0.5048E+01   -0.9947E+01
   0.06031    0.5710E+01   -0.9448E+01
   0.06408    0.6388E+01   -0.8916E+01
   0.06785    0.7083E+01   -0.8355E+01
```

0.07162	0.7784E+01	-0.7774E+01

(data intentionally removed)

0.71671	0.5338E+02	0.6231E+01
0.72049	0.5455E+02	0.6350E+01
0.72428	0.5582E+02	0.6478E+01
0.72806	0.5717E+02	0.6616E+01
0.73180	0.5862E+02	0.6762E+01
0.73559	0.6020E+02	0.6922E+01
0.73937	0.6193E+02	0.7096E+01
0.74315	0.6381E+02	0.7285E+01
0.74689	0.6586E+02	0.7491E+01
0.75068	0.6815E+02	0.7721E+01
0.75446	0.7070E+02	0.7978E+01
0.75824	0.7357E+02	0.8266E+01

Crack length	N,Cycles	Kmax+Krs	Kmin+Krs	Kop
0.2500E-03	0			
0.2550E-03	25	0.1039E+02	0.1038E+01	0.3821E+01
0.2600E-03	51	0.1007E+02	0.6530E+00	0.3629E+01
0.2650E-03	79	0.9746E+01	0.2677E+00	0.3457E+01
0.2700E-03	109	0.9426E+01	-0.1175E+00	0.3305E+01
0.2750E-03	142	0.9106E+01	-0.5028E+00	0.3159E+01
0.2800E-03	178	0.8785E+01	-0.8881E+00	0.3013E+01
0.2850E-03	217	0.8465E+01	-0.1273E+01	0.2868E+01
0.2900E-03	260	0.8145E+01	-0.1659E+01	0.2722E+01
0.2950E-03	307	0.7824E+01	-0.2044E+01	0.2576E+01
0.3000E-03	363	0.7504E+01	-0.2429E+01	0.2430E+01
0.3050E-03	431	0.7184E+01	-0.2814E+01	0.2284E+01
0.3100E-03	513	0.6864E+01	-0.3200E+01	0.2138E+01
0.3150E-03	614	0.6543E+01	-0.3585E+01	0.1993E+01

(data intentionally removed)

0.1626E-01	349318	0.5879E+02	0.6779E+01	0.2715E+02
0.1626E-01	349318	0.5888E+02	0.6788E+01	0.2719E+02
0.1627E-01	349318	0.5898E+02	0.6798E+01	0.2724E+02
0.1627E-01	349318	0.5907E+02	0.6807E+01	0.2728E+02
0.1628E-01	349318	0.5917E+02	0.6817E+01	0.2732E+02
0.1628E-01	349318	0.5926E+02	0.6827E+01	0.2737E+02
0.1629E-01	349318	0.5936E+02	0.6836E+01	0.2741E+02
0.1629E-01	349318	0.5945E+02	0.6846E+01	0.2745E+02
0.1630E-01	349318	0.5954E+02	0.6855E+01	0.2749E+02
0.1630E-01	349318	0.5964E+02	0.6865E+01	0.2754E+02
0.1631E-01	349318	0.5973E+02	0.6874E+01	0.2758E+02
0.1631E-01	349318	0.5983E+02	0.6884E+01	0.2762E+02
0.1632E-01	349318	0.5992E+02	0.6893E+01	0.2767E+02

FAILED

B.4 FORTRAN CODE.

```
C     PROGRAM KRS.for
C  This program uses linear superposition to grow a crack in a
C  residual stress field using (Kmax + Krs) and (Kmin + Krs)
C  input data for any general through-the-thickness crack
C  configuation. The FASTRAN crack-closure model is used to
C  develop the DKeff-rate for the material. The crack-opening
C  stress-intensity factor (Kop) is calculated from Kop/Kmax =
C  So/Smax = f(R, Smax/Sflow, alpha) where Smax/Sflow = 0.3
C  (Sflow is flow stress on material) and the constraint-loss
C  regime is used for calculating the variation in constraint
C  (alpha).
C-----------------------------------------------------------------
C
      IMPLICIT REAL*8 (A-H,O-Z)
      COMMON/BIGC/B,W,P,DKETAB(50),CGRTAB(50),C1(50),C2(50),
     1 AW(499),XKMAX(499),XKMIN(499),AKMAX(499),BKMAX(499),XKC,
     2 AKMIN(499),BKMIN(499),AWMIN,AWMAX,MTAB,NTAB,
     3 ALRAT,RATE1,ALP1,RATE2,ALP2
      CHARACTER*4 TITLE(20),TITLE1(20),MAT(20)
      CHARACTER*20 INFILE,OUTFILE
C
      PRINT *,'ENTER INPUT FILENAME ?'
      READ(5,11) INFILE
      PRINT *,'ENTER OUTPUT FILENAME (like out1.txt) ?'
      READ(5,11) OUTFILE
   11 FORMAT(A20)
      OPEN(3,FILE=INFILE,STATUS='UNKNOWN')
      OPEN(4,FILE=OUTFILE,STATUS='UNKNOWN')
C
      READ(3,15) TITLE
      WRITE(4,15) TITLE
   15 FORMAT(20A4)
      READ(3,15) TITLE1
      READ(3,*) W,B,AI,XKC
      WRITE(4,74) W,B,AI
   74 FORMAT(/,2X,'Width(W)= ',E10.3,3X,'Thickness(B)= ',E10.3,
     1 3X,'Crack length(Ai)= ',E11.4)
      WRITE(4,75) XKC
   75 FORMAT(5X,'Fracture toughness (Kc)= ',E11.4,/)
      READ(3,15) MAT
      WRITE(4,15) MAT
      READ(3,*) MTAB
      READ(3,15) TITLE1
      WRITE(4,76)
   76 FORMAT(5X,'DKeff',9X,'Rate')
```

```
      DO 77 I=1,MTAB
      READ(3,*) DKETAB(I),CGRTAB(I)
      WRITE(4,78) DKETAB(I),CGRTAB(I)
   78 FORMAT(3X,E11.4,3X,E11.4)
      DKETAB(I)=DLOG(DKETAB(I))
      CGRTAB(I)=DLOG(CGRTAB(I))
      IF(I.GT.1) THEN
      II=I-1
      IF(DKETAB(I).LE.DKETAB(II)) IERR = 2
      IF(CGRTAB(I).LE.CGRTAB(II)) IERR = 2
      IF(IERR.EQ.2) GOTO 999
      ENDIF
      IF(I.GT.1) THEN
      I2=I
      I1=I-1
      C2(I1)=(CGRTAB(I2)-CGRTAB(I1))/(DKETAB(I2)-DKETAB(I1))
      C1(I1)=DEXP(CGRTAB(I1)-C2(I1)*DKETAB(I1))
      ENDIF
   77 CONTINUE
C
      READ(3,15) TITLE1
      READ(3,*) RATE1,ALP1,RATE2,ALP2
      WRITE(4,68) RATE1,ALP1,RATE2,ALP2
   68 FORMAT(/,1X,'CONSTRAINT-LOSS REGIME:',/,1X,
     1 'RATE AT START OF TRANSITION =',E11.4,
     2 '  WITH  ALP1 = ',F4.2,/,
     3 1X,'RATE AT  END  OF TRANSITION =',E11.4,
     4 '  WITH  ALP2 = ',F4.2,/)
      RATE1=DLOG(RATE1)
      RATE2=DLOG(RATE2)
      ALRAT=1./(RATE1-RATE2)
      ALP=ALP1
      IF(ALP1.LE.ALP2) IERR=3
      IF(IERR.EQ.3) GOTO 999
C
      READ(3,*) NTAB
      READ(3,15) TITLE1
     WRITE(4,84)
   84 FORMAT(4X,'a/W',7X,'Kmax+Krs',6X,'Kmin+Krs')
      DO 87 J=1,NTAB
      READ(3,*) AW(J),XKMAX(J),XKMIN(J)
      AWMIN=AW(1)
      AWMAX=AW(NTAB)
      WRITE(4,86) AW(J),XKMAX(J),XKMIN(J)
   86 FORMAT(3X,F7.5,3X,E11.4,3X,E11.4)
      IF(J.GT.1) THEN
        J2=J
```

```
        J1=J-1
        BKMAX(J1)=(XKMAX(J2)-XKMAX(J1))/(AW(J2)-AW(J1))
        AKMAX(J1)=XKMAX(J1)-BKMAX(J1)*AW(J1)
        BKMIN(J1)=(XKMIN(J2)-XKMIN(J1))/(AW(J2)-AW(J1))
        AKMIN(J1)=XKMIN(J1)-BKMIN(J1)*AW(J1)
c
c      write(4,776) J1,AKMAX(J1),BKMAX(J1)
c  776 format(1x,I3,5x,E10.3,5x,E10.3)
c
      ENDIF
   87 CONTINUE
C
      WRITE(4,99)
   99 FORMAT(/,2X,'Crack length',7X,'N,Cycles',4X,'Kmax+Krs',
     1 6X,'Kmin+Krs',6X,'Kop')
      NCYC=0
      WRITE(4,111) AI,NCYC
      DELA=0.000005
      A=AI-DELA
  100 A=A+DELA
      Z=A/W
      CALL KMAX(Z,VKMAX)
      IF(VKMAX.GE.XKC) GOTO 995
      CALL KMIN(Z,VKMIN)
      CALL SOEQN(VKMAX,VKMIN,ALP,VKOP)
      DKEFF=VKMAX-VKOP
      CALL RATE(CGR,DKEFF,VKMAX)
      CALL VALP(CGR,ALP)
      NDEL=DELA/CGR
      NCYC=NCYC+NDEL
      Ag=A+DELA
      WRITE(4,111) Ag,NCYC,VKMAX,VKMIN,VKOP
  111 FORMAT(3X,E11.4,5X,I9,3(3X,E11.4))
      GOTO 100
  995 WRITE(4,222)
  222 FORMAT(/5X,'FAILED')
  999 STOP
      END
C
      SUBROUTINE KMAX(Z,VKMAX)
C COMPUTES KMAX from table
      IMPLICIT REAL*8 (A-H,O-Z)
      COMMON/BIGC/B,W,P,DKETAB(50),CGRTAB(50),C1(50),C2(50),
     1 AW(499),XKMAX(499),XKMIN(499),AKMAX(499),BKMAX(499),XKC,
     2 AKMIN(499),BKMIN(499),AWMIN,AWMAX,MTAB,NTAB,
     3 ALRAT,RATE1,ALP1,RATE2,ALP2
c
```

```
      IF(Z.LT.AWMIN.OR.Z.GT.AWMAX) WRITE(4,800)
  800 FORMAT(10X,'AWMIN or AWMAX')
      IF(Z.LT.AWMIN.OR.Z.GT.AWMAX) STOP
      DO 910 I=2,NTAB
c
c      write(4,777) I,Z,AW(I)
c  777 format(5x,I3,5x,E10.3,5x,E10.3)
c      write(4,777) I,AKMAX(I),BKMAX(I)
c
      IF(Z.LE.AW(I)) GOTO 920
  910 CONTINUE
      I=NTAB
  920 I1=I-1
      VKMAX=AKMAX(I1)+BKMAX(I1)*Z
C
c      WRITE(4,930) Z,VKMAX
c  930 FORMAT(5X,'Z= ',E11.4,4X,'KMAX= ',E11.4)
c
      RETURN
      END
C
      SUBROUTINE KMIN(Z,VKMIN)
C COMPUTES KMIN from table
      IMPLICIT REAL*8 (A-H,O-Z)
      COMMON/BIGC/B,W,P,DKETAB(50),CGRTAB(50),C1(50),C2(50),
     1 AW(499),XKMAX(499),XKMIN(499),AKMAX(499),BKMAX(499),XKC,
     2 AKMIN(499),BKMIN(499),AWMIN,AWMAX,MTAB,NTAB,
     3 ALRAT,RATE1,ALP1,RATE2,ALP2
c
      IF(Z.LT.AWMIN.OR.Z.GT.AWMAX) WRITE(4,800)
  800 FORMAT(10X,'AWMIN or AWMAX')
      IF(Z.LT.AWMIN.OR.Z.GT.AWMAX) STOP
      DO 910 I=2,NTAB
      IF(Z.LE.AW(I)) GOTO 920
  910 CONTINUE
      I=NTAB
  920 I1=I-1
      VKMIN=AKMIN(I1)+BKMIN(I1)*Z
C
c      WRITE(4,930) Z,VKMIN
c  930 FORMAT(5X,'Z= ',E11.4,4X,'KMIN= ',E11.4)
c
      RETURN
      END
C
      SUBROUTINE SOEQN(VKMAX,VKMIN,ALP,VKOP)
C COMPUTES CRACK-OPENING STRESS INTENSITY FACTOR
```

```
      IMPLICIT REAL*8 (A-H,O-Z)
C
      PI2=1.5708
c     Smax/Sflow = Z = 0.3
      Z=0.3
      A0=(0.825-0.34*ALP+0.05*ALP**2)*(DCOS(PI2*Z))**(1./ALP)
      A1=(0.415-0.071*ALP)*Z
      A3=2.*A0+A1-1
      A2=1.-A0-A1-A3
      R=VKMIN/VKMAX
      IF(R.GE.0.0) SX=A0+A1*R+A2*R**2+A3*R**3
      IF(R.LT.0.0) SX=A0+A1*R
      VKOP=SX*VKMAX
      IF(VKOP.LT.VKMIN) VKOP=VKMIN
C
c      WRITE(4,930) ALP,VKOP,VKMAX
c      930   FORMAT(5X,'ALP=   ',E11.4,4X,'KO=   ',E11.4,4X,'KMAX=
',E11.4)
C
      RETURN
      END
C
      SUBROUTINE RATE(CGR,DKEFF,VKMAX)
C COMPUTES CRACK-GROWTH RATE FROM TABLE LOOKUP
      IMPLICIT REAL*8 (A-H,O-Z)
      COMMON/BIGC/B,W,P,DKETAB(50),CGRTAB(50),C1(50),C2(50),
     1 AW(499),XKMAX(499),XKMIN(499),AKMAX(499),BKMAX(499),XKC,
     2 AKMIN(499),BKMIN(499),AWMIN,AWMAX,MTAB,NTAB,
     3 ALRAT,RATE1,ALP1,RATE2,ALP2
C
      CGR=0.0
      DO 10 I=2,MTAB
      IF(DKEFF.LE.DEXP(DKETAB(I))) GOTO 20
   10 CONTINUE
      I=MTAB
   20 I1=I-1
      CGR=C1(I1)*DKEFF**C2(I1)
      CGR=CGR/(1.-(VKMAX/XKC)**2)
C
c      WRITE(4,930) DKEFF,CGR
c  930 FORMAT(5X,'DKEFF= ',E11.4,4X,'CGR= ',E11.4)
C
   50 RETURN
      END
C
      SUBROUTINE VALP(CGR,ALP)
C COMPUTES ALP FROM CRACK GROWTH RATE
```

```
      IMPLICIT REAL*8 (A-H,O-Z)
      COMMON/BIGC/B,W,P,DKETAB(50),CGRTAB(50),C1(50),C2(50),
     1 AW(499),XKMAX(499),XKMIN(499),AKMAX(499),BKMAX(499),XKC,
     2 AKMIN(499),BKMIN(499),AWMIN,AWMAX,MTAB,NTAB,
     3 ALRAT,RATE1,ALP1,RATE2,ALP2
C
      CGRX=CGR
      IF(CGRX.EQ.0.0) CGRX=DEXP(RATE1)
      ACGR=DLOG(CGRX)
      ALP=ALP1
      IF(ACGR.LE.RATE1) GOTO 10
      ALP=ALP2+(ALP1-ALP2)*((ACGR-RATE2)*ALRAT)
      IF(ALP.LT.ALP2) ALP=ALP2
   10 CONTINUE
c
c      write(4,777) CGR,ALP
c  777 format(5x,'CGR= ',E11.4,4x,'ALP= ',F5.2)
c
      RETURN
      END
C
```

B.5 REFERENCES.

B-1. Hill, M.H., VanDalen, J.E., Stuart, D.H. and Minotti, J.R., Jr., "Analytical Tools for Residual Stress Enhancement of Rotorcraft Damage Tolerance—Volume 3: Residual Stress Measurements, Crack Growth Testing and LEFM Analyses," FAA Report DOT/FAA/TC-13/36, V3.

B-2. Ismonov, S., Daniewicz, S.R., Newman, J.C., Jr., Hill, M.R., and Urban, M.R., "Three Dimensional Finite Element Analysis of a Split-Sleeve Cold Expansion Process," *Journal of Engineering Materials and Technology*, Vol. 131, 2009, pp.71-78.

B-3. Newman, J.C., Jr., Yamada, Y., and James, M.A., "Stress-Intensity Factor Equations for Compact Specimen Subjected to Concentrated Forces," *Engineering Fracture Mechanics*, Vol. 77, 2010, pp. 1025-1029.

B-4. Newman, J.C., Jr., "A Crack Opening Stress Equation for Fatigue Crack Growth," *International Journal of Fracture*, Vol. 24, 1984, pp. R131-R135.

B-5. Newman, J.C., Jr., Johnson, W.S., and Zhao, W., "Assessment of Residual Stresses and Hole Quality on the Fatigue Behavior of Aircraft Structural Joints," FAA Report DOT/FAA/AR-07/56, V1, March 2009.